学位論文

X-ray Study of Nuclear Activity in Nearby Galaxies
(X 線観測による近傍銀河の中心核活動性の研究)

1997 年
寺島 雄一

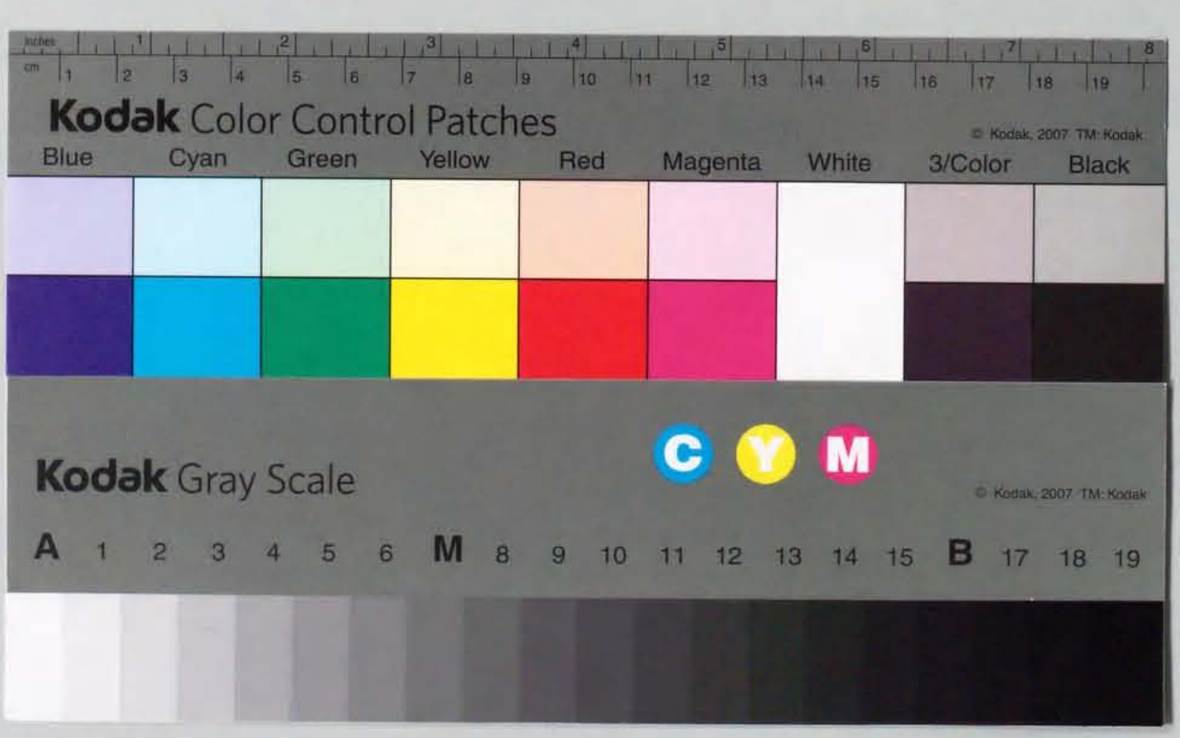

X-ray Study of Nuclear Activity in Nearby Galaxies

Yuichi Terashima

Dissertation submitted to the Graduate School of Science,
Nagoya University in partial fulfillment of the requirements
for the degree of Doctor of Science (Physics)

28 November, 1997

Abstract

Active galactic nuclei (AGNs) emit huge energy in all wavelengths from radio to γ-ray and the most plausible energy source of emission is the gravitational energy of the accreting matter onto a super massive blackhole at the center of galaxies. AGNs are present in about 1% of galaxies. Recent optical spectroscopic surveys revealed that $\sim$1/3 of bright galaxies show weak activity characterized by optical emission lines from low ionization species called low ionization nuclear emission-line regions (LINERs). The origin of LINERs are still under debate among several mechanisms including low luminosity AGNs, hot stars, cooling flows, and so on.

In order to search for AGNs using the broad band X-ray spectra and images, we observed 12 LINERs with the *ASCA* satellite. Almost all objects are detected for the first time in the 2–10 keV band, and the X-ray luminosities are $4 \times 10^{39} - 5 \times 10^{41}$ ergs s^{-1} in the 2–10 keV band. These luminosities are more than 1–3 orders of magnitude smaller than usual Seyfert galaxies. Their X-ray spectra are generally represented by a combination of a power-law with a photon index around 1.8 and a thermal plasma with $kT \sim 0.5 - 1$ keV. Most of LINERs with broad Hα in the optical spectrum indicate point like hard X-ray source and their X-ray luminosities are well correlated with Hα luminosities. These facts strongly support that these LINERs harbor low luminosity AGNs and infer that AGNs are present at the nucleus of many apprently normal galaxies. On the other hand, majority of LINERs without broad Hα in our sample are X-ray dim compared to X-ray - Hα luminosity correlation for low luminosity Seyfert galaxies and LINERs with broad Hα. Hard X-ray weakness of these objects means that their optical emission lines are ionized by other mechanism rather than low luminosity AGNs and/or that AGN is heavily obscured even at energies above 2 keV. X-rays from these objects can be attributed to the starburst activity and/or discrete sources in the host galaxy.

The detailed study of AGN characteristics at the lowest luminosity end provides strong constraints on energy release and emission mechanisms in AGNs. For this purpose, we also observed 8 low luminosity Seyfert galaxies. Obtained X-ray luminosity ranges from 6×10^{39} ergs s^{-1} to 6×10^{41} ergs s^{-1}. We compared X-ray properties of this class of AGNs, LINERs with low luminosity AGN, and luminous AGNs. The continuum shape of the X-ray spectrum of low luminosity AGNs is very similar to luminous Seyfert galaxies; the photon index distributes around 1.8 and the absorption column density ranges from 10^{20} cm^{-2} to 10^{24} cm^{-2}. On the other hand, iron K emission lines in low luminosity AGNs show variety in the center energy and strength. These results infer that physical states of the accretion disk around the low luminosity AGNs are different from those of luminous AGNs.

Contents

List of Figures

List of Tables

Chapter 1

Introduction

Active Galactic Nuclei (AGNs) are one of the most energetic phenomena. AGNs emit huge energy in all wavelengths from radio to γ-ray and it is thought that the emitted energy is liberated by the accretion of matter onto a super massive black hole at the center of galaxies (Rees 1984). Such a nucleus is present in about 1% of galaxies. There are many luminous AGNs (quasars) at a redshift around $\sim$ 2, and number of quasars rapidly decline with time (i.e. decrease of a redshift). Then many 'remnant' of quasars should be present in the local Universe.

Recent optical spectroscopic surveys revealed that $\sim$1/3 of bright galaxies show weak activity characterized by optical emission lines from low ionization species called low ionization nuclear emission-line regions (LINERs). The origin of LINERs are still under debate and one possible origin is photoionization by a 'dwarf' (= low luminosity) AGN. If most of LINERs are genuine AGNs, there are much more AGNs in the local Universe than previously thought. Weak activity in nearby galaxies are a candidate of the dead quasars. On the other hand, there are observational indications of the presence of super massive black hole at the center of galaxies (Kormendy & Richstone 1995). These super massive black holes in nearby galaxies are also a candidate of the dead quasars (Rees 1990).

AGN is bright in X-rays and have been intensively studied since early days of X-ray astrophysics. X-ray observations are one of the most powerful tools to investigate the AGN phenomena, since X-rays are emitted from just vicinity of the central black hole. Additionally, the hard X-ray observations have an advantage that hard X-rays can see the nucleus through the thick obscuring matter of equivalent hydrogen column density of more than 10^{23} cm^{-2}. However few X-ray observations of 'dwarf' AGNs have been performed because of limited sensitivity and energy band of previous instruments. The

ASCA satellite achieved unprecedented high sensitivity in the wide energy band 0.5–10 keV and enables us systematic study of weak activity in apparently 'normal' galaxies. Imaging capability in the hard X-ray band is also essential to search for a dwarf AGN as a hard point source at the galactic center, particularly the case for the AGN is heavily obscured.

In this thesis, we search for an AGN in LINERs using the broad band X-ray spectra and images obtained with *ASCA* and examine the ionization mechanisms in LINERs. We find X-rays considered to be dominated by emission from a low luminosity AGN from many LINERs selected based on results from optical emission line surveys.

The optical emission line surveys also revealed that $\sim 10\%$ of nearby galaxies contain dwarf Seyfert nuclei. We also present the *ASCA* results of these Seyfert galaxies. Using these low luminosity Seyfert galaxies and LINERs with a low luminosity AGN, we investigate X-ray properties of these low luminosity AGNs. The mechanism of energy release and radiation in AGNs has not yet understood. The detailed study of AGNs in an extreme condition, i.e. very low luminosity, provides a strong constraints on such mechanisms. We compare our results with theoretical prediction on radiation.

In chapter 2, we present a review of current understanding of AGNs and weak activity in nearby galaxies. The *ASCA* satellite and on board instruments are described in chapter 3. In Chapter 4, summary of the observed galaxies and previous observations for them are given. Chapter 5 describes the results on individual objects. In Chapter 6, we discuss the origin of the detected X-rays and X-ray properties of low luminosity AGNs. Conclusions are given in Chapter 7.

Chapter 2

Reviews

2.1 Active Galaxies

2.1.1 Active Galactic Nuclei (AGN)

Active Galactic Nuclei (AGN) emit in all wavelengths from radio to γ-ray at enormous luminosity. It is thought that the emitted energy is liberated by the accretion of matter onto a super massive blackhole at the center of galaxies (Rees 1984).

AGNs are classified into some subclasses based on their optical spectra, radio loudness, luminosities, and so on. Based on radio loudness, two subclasses radio quiet AGNs and radio loud AGNs are defined. Radio quiet AGNs are classified into Seyfert galaxies and radio quiet quasars, while radio loud AGNs into radio galaxies and radio loud quasars with increasing luminosity. There is other subclass: LINERs (low ionization nuclear emission line regions; Heckman 1980). LINERs, which show strong low ionization optical emission lines, will be reviewed in the following sections.

Seyfert galaxies are divided into two categories: Seyfert 1 (type 1 Seyfert) and Seyfert 2 (type 2 Seyfert) based on widths of optical permitted lines. Seyfert 1s show both broad (FWHM > 1000 km s^{-1}) and narrow (FWHM$\sim$500 km s^{-1}) permitted lines, while Seyfert 2s show only narrow lines. Seyfert 1s show non-thermal optical continuum. On the other hand non-thermal continuum is very weak or absent in Seyfert 2s. The intermediate types (Seyfert 1.5 / 1.8 / 1.9) are also defined. Balmer lines in Seyfert 1 galaxies are dominated by broad component, while Seyfert 1.5 galaxies indicate both broad and narrow Hα line. Seyfert 1.8 galaxies have weak broad Hα and Hβ, and Seyfert 1.9 galaxies have broad Hα and undetectable broad Hβ. The same classifications are also applicable to quasars and radio galaxies: type 1 / type 2 quasars and broad line radio galaxies / narrow line radio galaxies.

Optical emission lines are primarily due to photoionization by the emission from the central source. Strength of emission lines reflects the physical state of the line emitting gas and shape of the ionizing continuum.

Some authors developed the excitation diagrams to classify Seyfert galaxies, LINERs and HII nuclei (Baldwin, Philips, & Terlevich 1981, Veilleux & Osterbrock 1987). Seyfert galaxies show both high ionization and low ionization emission lines. LINERs have strong emission lines from low ionization species ([OI]λ6300, [NII]$\lambda\lambda$6548, 6583, [SII]$\lambda\lambda$6716, 6731) and weak high ionization lines. HII nuclei is ionized by OB stars and show strong [OIII]λ5007 emission and Balmer lines, but weak low ionization lines. These characteristics are clearly separated on the excitation diagrams, for example, [OIII]/Hβ — [OI]/Hα plane (Veilleux & Osterbrock 1987). Strength of the highly and low ionized emission lines are explained in terms of ionizing continuum. AGNs contain many high energy photons which can penetrate deeply in the line emitting gas and make a large partially ionized region.

2.1.2 The Unified Model of AGN

There are various pieces of evidence that Seyfert 1s and Seyfert 2s are intrinsically same. In the unified model of AGN, the observed differences of various AGNs are attributed to the difference of the orientation of the obscuring torus to the line of sight and the obscuration by the 'torus' (Antonucci 1993, Lawrence 1987).

Antonucci & Miller (1985) detected polarized broad emission lines by spectropolarimetry from the prototypical Seyfert 2 NGC 1068 and revealed that the broad line region is present also in Seyfert 2s. Miller & Goodrich (1990) observed several Seyfert 2s and detected polarized broad lines. These polarized broad lines are interpreted as scattered flux by electrons located above an 'obscuring torus'. The [OIII]λ5007 line image shows biconical structure (ionizing cone) which suggests emission from the central source is collimated by a torus (e.g. Tudhunter & Tsvetanov 1989). The detection of hard X-ray emission obscured by column densities of $N_{\rm H}$=$10^{22} - 10^{24}$ cm^{-2} with the *Ginga* satellite provides further evidence for Seyfert 2s contain hidden Seyfert 1 nuclei (Awaki et al. 1990, Awaki et al. 1991).

On the other hand, there are increasing evidence against this simple orientation dependent unification scheme. For example, Seyfert 2s indicate more molecular gas, far infrared emission, dust, and circumnuclear starburst than Seyfert 1s and these properties are not caused by orientation effect (Heckman et al. 1989, Dahari & De Robertis 1988).

2.1.3 X-ray observations of active galactic nuclei

Seyfert 1: AGNs are known to be bright X-ray sources from early days of X-ray astronomy. *HEAO-1* measured the X-ray spectra of large sample of AGNs and revealed that the X-ray spectra of AGNs are well modeled by a power-law with a photon index of ~ 1.7 in the 2–20 keV band (Mushotzky et al. 1980, Mushotzky 1982, Rothschild et al. 1993, Mushotzky 1984). Observations by *EXOSAT* and *Ginga* confirmed these results (Turner & Pounds 1989, Awaki et al. 1991, Nandra & Pounds 1993). *Ginga* observations of Seyfert 1s revealed the presence of fluorescent iron K lines at 6.4 keV. *Ginga* spectra of Seyfert 1s also show spectral flattening above ~10 keV (Pounds et al. 1990). These spectral features are interpreted to be caused by reprocessing due to cold matter subtended large solid angle viewed from the nucleus (Lightman & White 1988; Guibert & Rees 1988; George & Fabian 1991; Matt, Perola, & Piro 1991). At higher energies, Compton down-scattering and the reduction of the scattering cross section deplete the number of photons reflected, resulting in a broad band spectral bump peaking at $\sim 20 - 30$ keV. If this 'Compton reflection' is taken into account, the intrinsic spectral slope for a large *Ginga* sample of Seyfert 1 s is $\Gamma = 1.95 \pm 0.05$ rather than $\Gamma = 1.7$ (Nandra & Pounds 1993). Recent *ASCA* observations of Seyfert 1 s revealed that the iron line is broad (FWHM$\sim 10000 - 100000$ km s^{-1}) and asymmetric in profile; skewed to lower energies (e.g. Tanaka et al. 1995, Nandra et al. 1997b). This iron line is interpreted to be emitted from inner most part of the accretion disk (Tanaka et al. 1995, Fabian et al. 1995; see also Fabian et al. 1989 for the disk-line model).

quasars: Broad band X-ray spectra of quasars with higher luminosity than Seyfert galaxies are obtained from the *Ginga* (Lawson & Turner 1997, Williams et al. 1992) and *EXOSAT* (Comastri et al. 1992, Lawson et al. 1992) observations. The spectra of radio-quiet quasars are generally consistent with Seyfert 1s. Iron K emission is detected from a few quasars (e.g. E1821+643, Kii et al. 1991, Yamashita et al. 1997; PG1116, Nandra et al. 1996). The line center energy of these objects are higher than Seyfert galaxies (6.4 keV) and consistent with He-like or H-like iron. Nandra et al. (1997c) summed the *ASCA* spectra of high luminosity AGNs and showed that the center energy of the iron line is higher and red tail is weak compared to Seyfert 1 galaxies. *ASCA* spectra of radio quiet quasars at $z \sim 1$ show no significant reflection component (Nandra et al. 1995). These properties of iron line and absence of reflection would be due to ionization of the accretion disk (Nandra et al. 1997c).

Seyfert 2: *Ginga* observations of Seyfert 2 galaxies revealed the presence of heavily obscured AGN and provides additional support of the unified model (Awaki et al. 1990,

Awaki et al. 1991). The absorption column densities are distributed from $10^{22} - 10^{24}$ cm^{-2}. In many cases strong iron K emission is observed. Iron K emission is produced by transmission through the obscuring matter and/or scattering by cold / warm material (e.g. Turner et al. 1997b). In the low energy part (<several keV) of the Seyfert spectra, a soft X-ray emission is seen, and is accompanied with emission lines in some cases (Turner et al. 1997a, Ueno 1995, Iwasawa 1994). These soft emission is due to scattered emission by warm gas located above the opening part of the putative obscuring torus and / or starburst activity.

time variability: X-ray emission from AGN shows variability of the shortest time scale in any wavelength band. Since variability of a time scale shorter than the light crossing time of the emitting region cannot be observed, time scales gives an upper limit of the source size: $R < c\Delta t$. Assuming $R = 5R_s$, this can be translated to a limit on the mass: $M < 2 \times 10^7 \frac{\Delta t}{1000 \text{ sec}} M_\odot$.

2.1.4 Starburst galaxies

In Starburst galaxies, intensive star formation is undergoing in the central region of the galaxy. Starburst galaxies are strong far infrared emitter probably due to the dust heated by the radiation from massive stars. Collective super nova explosions of short life massive stars and stellar winds from massive stars heat the interstellar gas and lead to outflow along the direction of the minor axis of the galaxy. Such outflows are called galactic superwinds (Heckman, Lehnert, & Armus 1993, Heckman et al. 1990, Tomisaka & Ikeuchi 1988). Optical emission line profiles and line imaging indicates the presence of outflowing gas (e.g. Heckman et al. 1990, Armus et al. 1996). Note that optical emission line ratios of the off nucleus are similar to LINERs and probably due to shock excitation. Soft X-ray images obtained with *Einstein* IPC also indicate the presence of hot gas extended to the minor axis direction of the host galaxy (Fabbiano 1988; Watson, Stanger, & Griffiths 1984; Fabbiano, Heckman, & Keel 1990). These extended X-ray emission is a prominent in soft X-rays and temperature of the X-ray emitting gas is typically 1 keV or less. *ASCA* spectra of starburst galaxies clearly show various emission lines due to hot gas of temperature around 0.5–1 keV (Ptak et al. 1996, Moran & Lehnert 1997, Tsuru et al. 1997). *ASCA* measurements of the abundance of metals of hot gas result in apparent deficit of iron compared alpha-elements O, Ne, Mg, Si, and S. The soft X-ray emission is roughly proportional to far infrared luminosity; $L_X/L_{FIR} \sim 10^{-4}$ (David, Jones, & Forman 1992, Heckman et al. 1990).

Ginga and *ASCA* observations show starburst galaxies also emit hard X-rays. *Ginga* spectra of starburst galaxies are well fitted with a thermal bremsstrahlung model with temperature of several keV (Ohashi et al. 1990, Tsuru 1992). *ASCA* observations provide similar results with *Ginga* or harder spectra in some cases (photon index ~ 1; Awaki et al. 1996). Origin of the hard component is heterogeneous; including single or superposition of discrete sources such as X-ray binaries (Collura et al. 1994, Awaki et al. 1996, Okada et al. 1997), hot gas heated by supernova explosions, inverse Compton scattering of far infrared photons by energetic electrons (Moran & Lehnert 1997).

2.2 Low level activity in nearby galaxies

2.2.1 Results from optical spectroscopic surveys

Optical spectroscopic surveys in 80's revealed that many nearby galaxies show activity which is recognized by nuclear spectra with emission lines (Heckman 1980; Stauffer 1982; Keel 1983a, b; Filippenko & Sargent 1985, Véron-Cetty & Véron 1986; Phillips et al. 1986). These surveys indicate 'active galaxies' are more numerous than previously thought.

The optical spectra of these galaxies are characterized by strong low-ionization emission lines such as [OI]λ6300, [OII]λ3727, [NII]$\lambda\lambda$6548, 6583, and [SII]$\lambda\lambda$6716, 6731. Heckman (1980) defined a class LINERs (Low Ionization Nuclear Emission-line Regions) by two oxygen line intensity ratios: [OII]$\lambda\lambda$3726, 3729 / [OIII]λ5007 $\geq$ 1 and [OI]λ6300 / [OIII]λ5007 $\geq$ 1/3. Some authors adopt different definition of LINERs (for example [NII]λ6583 / Hα >0.6). We adopt the definition by Ho et al. (1997a) (Table 2.1). Heckman(1980) shows about 1/3 of bright ($B_T \leq 12$) galaxies have LINER. Thus LINERs are quite common. (Seyfert galaxies are about 1% of all bright galaxies (Weedman 1977)).

Among several optical spectroscopic surveys of bright galaxies conducted so far, the Palomer survey (Filippenko & Sargent 1985; Ho Filippenko & Sargent 1995, 1997a, 1997b, 1997c; Ho et al. 1997d, Ho 1996) which is recently completed contains largest sample and high quality optical spectra are compiled after precise starlight subtraction using their sample galaxies without emission lines. In the Palomer Survey, long slit (2"×4") optical spectra of moderate resolution (4 A for 4230–5110 A and 2.5 A for 6210–686) of bright (magnitude0 A limit B_T=12.5 mag) northern ($\delta > 0°$) galaxies were obtained and intensities of emission lines were measured (Ho et al. 1995, 1997a). Based on these measurements, Ho et al. (1997a) classified sample galaxies into five classes; absorption line galaxies, HII nuclei, Seyfert nuclei, LINERs, and transition between LINERs and

Table 2.1: Definition of LINER, Seyfert, and HII nucleus based on optical emission line ratios taken from Ho et al. 1997a

Class	[OIII]λ5007/Hβ	[OI]λ6300/Hα	[NII]λ6583/Hα	[SII]$\lambda\lambda$6716,6731/Hα
HII nuclei	Any	< 0.08	< 0.6	< 0.4
Seyfert nuclei	≥ 3	≥ 0.08	≥ 0.6	≥ 0.4
LINERs	< 3	≥ 0.17	≥ 0.6	≥ 0.4
Transition nuclei	< 3	$\geq 0.08, < 0.17$	≥ 0.6	≥ 0.4

HII nuclei (Table 2.1). Their results show that 40%, 13%, 19%, 14% of nearby bright galaxies are classified as HII, Seyfert, LINER, and transition, respectively. Thus 'active' galaxies are fairly common in bright galaxies. A median Hα luminosity of these AGNs (we tentatively regard Seyfert + LINER + transition as AGNs; see next section) is only 2×10^{39} ergs s^{-1}, which is more than two orders of magnitudes lower than previously known AGNs. Furthermore Ho et al. (1997d) detected broad Hα from 10% of their sample galaxies. Detection of a broad Hα infer that they are genuine AGNs and a super massive blackhole is present at the center of these galaxies.

2.3 Low Ionization Nuclear Emission-line Regions — (LINERs)

2.3.1 Excitation mechanisms of LINERs

Optical spectroscopic surveys revealed that LINERs are quite common and about 1/3 of bright galaxies contains a LINER nucleus. The origin of LINER optical emission lines are still under debate and there are some proposed excitation mechanisms (see Filippenko 1996, Filippenko 1989 for review) including shock excitation, photoionization by low luminosity AGN, photoionization by very hot stars, and cooling flows.

Originally LINERs are considered to be from shock heated gas (Koski & Osterbrock 1976, Fosbury et al. 1978, Heckman 1980). Observed spectra of LINERs resemble those of supernova remnants. Furthermore LINER like optical spectra are often observed from the galactic superwinds of starburst galaxies (e.g. Heckman, Armus & Miley 1990). The emission line gas of the superwinds are extended to kpc scale in some cases and at least some LINERs, specifically extended ones, are probably excited by starburst driven winds.

LINER emission lines are also well reproduced by photoionization by low luminosity AGNs with a ionization parameter

$$U = \frac{\int_{\nu_0}^{\infty} \frac{L_\nu}{h\nu} d\nu}{4\pi r^2 nc}$$

of $10^{-3} - 10^{-4}$, which is 1–2 orders of magnitude smaller than usual Seyfert galaxies ($U \sim 10^{-2}$) (Ferland & Netzer 1983, Ho, Filippenko, & Sargent 1993). High energy photons make a partially ionized region and strong emission lines due to low ionized species are produced. In some LINERs, broad Hα similar to Seyfert 1 galaxies and X-ray emission are detected and infer the presence of low luminosity AGNs.

If very hot stars are abundant, there may be enough high energy photons to make lower ionized emission lines. Photoionization by very hot stars were calculated by some authors (Filippenko & Terlevich 1992, Shields 1992) and reproduce LINER emission lines of specifically weak [OI] LINERs.

Extended LINER is seen in the central region of the elliptical galaxies and may be originated from small cooling flows (Fabian 1986, Heckman 1989).

2.3.2 Recent progress of observations of LINERs

In order to distinguish excitation mechanisms in LINERs and search for direct evidence of the presence of an AGN, many observational efforts have been made. We summarize the recent observational progress of LINERs.

HST UV images

UV imaging observations are performed to search for a UV nucleus with *HST* Faint Object Camera (FOC) (Maoz 1996, Maoz et al. 1995) and Wide Field Planetary Camera 2 (WFPC2) (Barth et al. 1996a, 1998) at a wavelength of 2300 A. An UV nucleus is detected from only 20–25% of LINERs and rest of LINERs are turned out to be UV dark. Proposed reasons for UV darkness are (1)AGN is obscured, (2)AGN is in the 'off' state, and (3)LINER emission lines in optical spectra are excited by other mechanisms rather than AGNs. Using Maoz et al. (1995) and their own sample, Barth et al. (1998) conclude that dust obscuration is the dominant factor determining whether or not a UV source is detected.

HST UV spectra

UV spectroscopy provides important diagnostics of the excitation mechanism of LINERs from which UV nucleus is detected. If an AGN dominates a UV spectrum, a featureless continuum is expected, while hot stars show UV absorption lines such as CIVλ1459, SiIVλ1397, and HeIIλ1640. UV emission lines also provides information on the excitation

mechanism. The shock models predict strong UV emission lines and little UV continuum emission compared to photoionization (Dopita et al. 1997, Dopita et al. 1996).

UV emission lines consistent with the shock model are observed only from off nucleus of M87 by *HST* FOS observations (Dopita et al. 1997, Dopita et al. 1996). On the other hand, *HST* FOS UV spectra of M81 and NGC 4579 show a featureless continuum most likely of non stellar origin and broad emission lines (FWHM≈2000-4000 km s^{-1}) similar to Seyfert 1 galaxies (Ho et al. 1996, Barth et al. 1996b).

Maoz et al. (1998) compiled UV spectra of seven LINERs. UV emission from at least three LINERs shows absorption lines and dominated by massive stars. UV emission from other four LINERs is not sufficient to explain observed optical emission line fluxes. Maoz et al. (1998) concluded that the UV compact source is a nuclear starburst rather than AGN, at least in some cases. Maoz et al. (1998) compare their results and our *ASCA* results (this thesis) and suggests that the AGN component is most prominent at higher energies.

Thus UV spectra are useful to distinguish excitation mechanisms of UV emission lines in some cases. However obviously observations at higher energies are necessary since hot stars are often dominate UV emission and most of LINERs are UV dark, which means we cannot obtain any UV spectrum.

X-ray observations prior to ROSAT and ASCA

X-rays are emitted from region in vicinity of the central blackhole and provides us a direct evidence of the presence of AGN in LINERs if LINERs are genuine AGNs. However X-ray observations prior to *ROSAT* and *ASCA* is limited in sensitivity and X-ray emission is detected from very limited number of LINERs. The pre-*ASCA* observational results of LINERs and low luminosity Seyfert galaxies are summarized in Mushotzky (1993).

Halpern & Steiner (1982) compiled *Einstein* IPC observations of 15 LINERs and low luminosity Seyfert galaxies and found preliminary evidence for photoionizing X-ray emission. However they cannot exclude the possibility that the X-ray flux from the low luminosity objects is not nuclear.

ROSAT X-ray observations

Using the *ROSAT* satellite, X-ray properties of LINERs are investigated. *ROSAT* HRI images of several LINERs show X-ray nucleus (Koratkar et al. 1994; Fabbiano & Juda 1997). X-ray spectra obtained with *ROSAT* PSPC are consistent with Seyfert galaxies, although emission line like features probably due to a hot gas in the host galaxy are sometimes seen (Koratkar et al. 1994, Fabbiano 1996). For the brightest objects, L_X/LHa values are similar to Seyfert 1s and X-ray emission seems to be dominated by a low luminosity AGN (Koratkar et al. 1994). However *ROSAT* sensitivity is limited to

energies less than 2 keV and it is difficult to detect X-ray emission from a weak obscured AGN. Furthermore, spectral resolution of *ROSAT* PSPC is poor and hard to distinguish soft thermal emission accompanied by low energy emission lines from continuum emission due to possible AGN.

ASCA observations

The *ASCA* satellite achieved high sensitivity and imaging capability up to 10 keV. X-ray spectra above 2 keV is essential to search for AGNs especially in the case an AGN is obscured. Even in the case that AGN is not significantly obscured, soft band spectra of galaxies are often complicated due to thermal emission and difficult to study the pure AGN spectra. X-ray emission from thermal plasmas are often observed from both elliptical galaxies (e.g. Forman, Jones, & Tucker 1985) and spiral galaxies (Makishima 1994, Read et al. 1997 and references therein). The spectral resolution of SIS and GIS on-board *ASCA* is unprecedentedly highly and can resolve many emission lines from thermal plasmas in the host galaxy. Emission lines would be also expected from photoionized plasmas around the continuum source on the AGN (e.g. Turner et al. 1997a).

X-ray images above 2 keV is also quite important to study an activity at the center of galaxy, since emission from an AGN is a point source while discrete sources distributed over a galaxy is expected to be extended in case of nearby galaxies. One of the clear example is the low luminosity Seyfert 1.9 galaxy NGC 4258 (Makishima et al. 1994). The X-ray image above 3 keV is point-like while image below 3 keV is extended. The X-ray spectrum also revealed the presence of highly obscured (N_H=1.5 × 10^{23} cm^{-2}) hard X-ray source, which is obviously identified with the Seyfert nucleus. Some other *ASCA* observations of LINERs are published as Ishisaki et al. (1996; Seyfert 1.5/LINER M81), Iyomoto et al. (1996; Seyfert 1/LINER NGC 1097), and Serlemitsos et al. (1996).

Chapter 3

Instrumentation

3.1 The ASCA satellite

ASCA is the fourth Japanese X-ray astronomy satellite subsequent to *Hakucho*, *Tenma*, and *Ginga* (Tanaka, Inoue, & Holt 1994). It was launched by the M-3S-II rocket from Kagoshima Space Center (KSC) on 1993 Feb. 20, and placed into a near-circular orbit with a perigee of 520 km, an apogee of 625 km, and an inclination of 31° and the orbital period is 96 minutes.

ASCA carries four identical X-ray telescopes (XRT) and two SIS (Solid-State Imaging spectrometers) and two GIS (Gas Imaging spectrometers) are placed at the focal plane.

3.2 X-ray telescopes; XRT

The X-ray telescopes (XRT) onboard *ASCA* (Serlemitsos et al. 1995) are developed by NASA/GSFC, Nagoya University, and ISAS.

X-rays are totally reflected by metal at small angle less than the critical angle. Therefore grazing incidence optics are used. The Wolter type I configuration is usually used for X-ray telescopes. In this configuration, X-ray are reflected by paraboloid and hyperboloid mirror shells and focused. *ASCA* XRT is an approximation of the Wolter I using conical aluminum foil mirrors. Each mirror shell consists of thin aluminum foil with a thickness of 127 μm and large effective area up to 10 keV is achieved by nesting 120 foils. The design parameters of the XRT are shown in Table 3.1.

The effective area depends on the X-ray energy and the off axis angle. The total effective area of 4 XRTs is 1300 cm^2 at 1 keV and 600 cm^2 at 6 keV at on axis (Fig 3.3). The effective area decreases with increasing off axis angle (vignetting effect) (Fig 3.4).

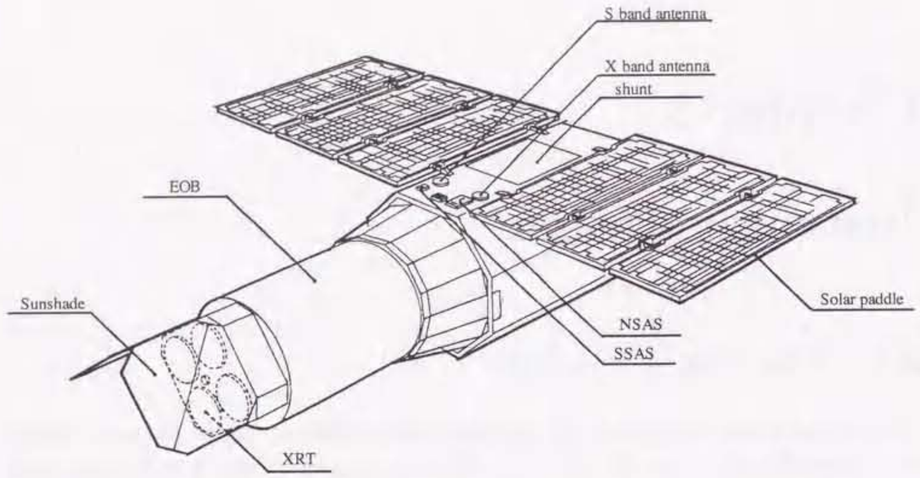

Figure 3.1: Schematic view of the ASCA satellite

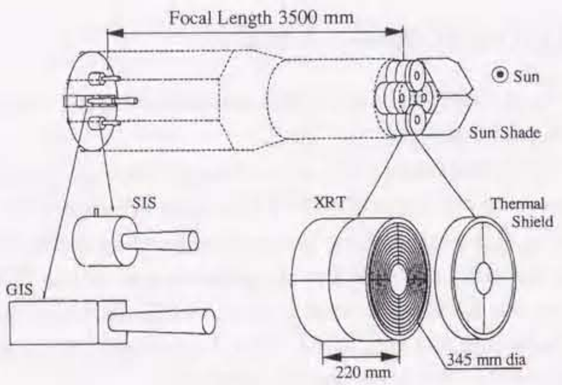

Figure 3.2: Onboard instruments of the ASCA satellite

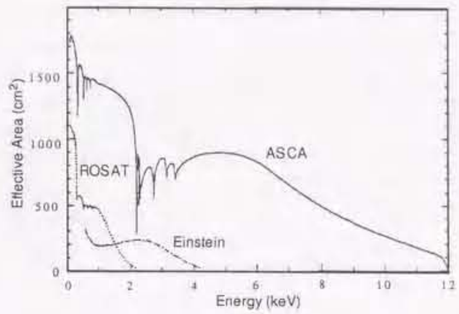

Figure 3.3: Effective area of ASCA

Then the XRT field of view is typically 18'–24' in FWHM diameter.

The spatial resolution of the XRT is about 3' in half power diameter (HPD). The point spread function (PSF) has a sharply peaked core and extended outskirt. The shape of the PSF is energy dependent: higher energy photons is scattered to outer radius and then the PSF is more extended. The example of the image of the point source and radial profile of surface brightness (3C273) are shown in Fig 3.5 and Fig 3.6. The shape of the PSF also depends on position on the detector. At larger off axis angle, the PSF elongates towards the azimuthal direction and squeezed into the radial direction.

We utilize the ray-tracing program to simulate the PSF (Tsusaka et al. 1995). Fig 3.6 shows the comparison of the simulated PSF and the actual SIS data of the point source 3C273 in the 0.5–2 keV and 2–10 keV band. Background image produced from the black sky fields released by NASA Guest observer facility. The ray-traced PSF reproduce the observed PSF quite well around the core. The extended component of the PSF is reproduced within a radius of 5–6'. Systematic residuals are visible outer than 6' radius.

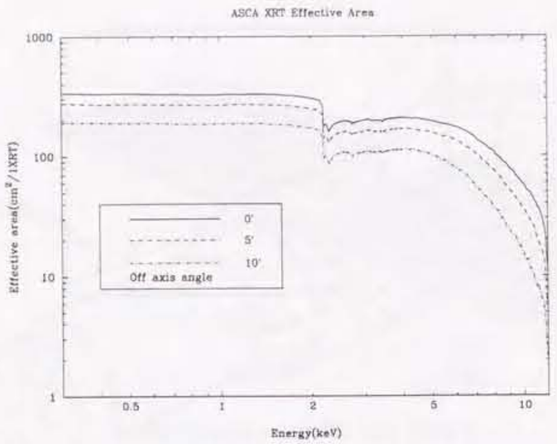

Figure 3.4: Off axis angle dependence of the Effective area of the ASCA XRT

Table 3.1: Design parameters and performance of the XRT

Mirror substrate	Aluminum foil (127 μm)
Mirror surface	Acrylic lacquer (10 μm) + Au (500 A)
Mirror length	100 mm
Number of foils	120 foils
Inner/ outer diameter	120 mm / 345 mm
Focal length	3500 mm
Incident angle	0.24° – 0.7°
Total weight (four telescopes)	~40 kg
Geometrical area	558 cm^2
Field of view (FWHM)	24' at 1 keV
	16' at 7 keV
Energy range	$\leq$10 keV
Effective area	1300 cm^2 at 1 keV
(four telescopes)	600 cm^2 at 6 keV
Half power diameter	~3 arcmin

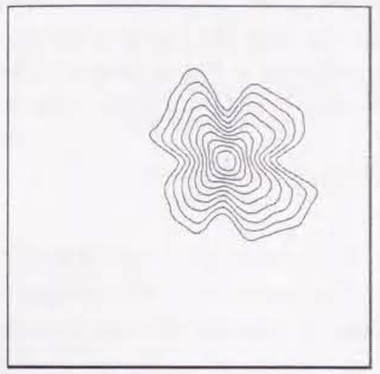

Figure 3.5: ASCA SIS image of the quasar 3C273 in the 0.5–10 keV band. Image size is 11'×11' square.

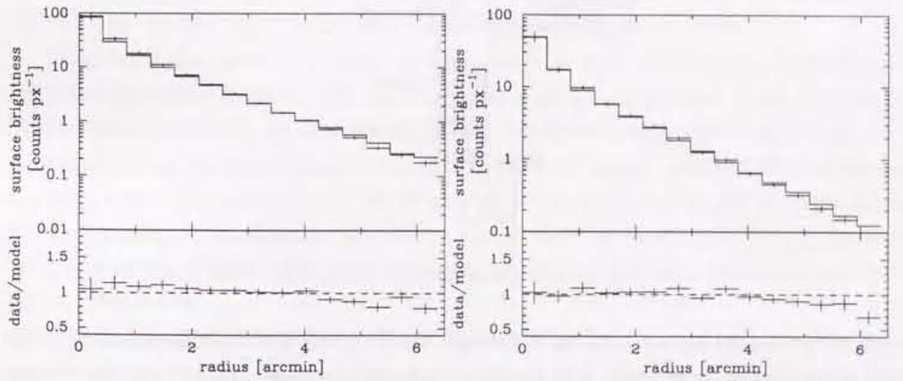

Figure 3.6: Radial profile of surface brightness in the 0.5–2 keV (left) and 2–10 keV (right) band. Crosses are observed data of 3C273 and histogram represent the point spread function simulated by the ray-tracing assuming a photon index of 1.6. Background is subtracted from the 3C273 data using the blank sky data.

3.3 Gas Imaging Spectrometer; GIS

The Gas Imaging Spectrometer (GIS) is an imaging gas scintillation proportional counter developed mainly by University of Tokyo, ISAS, and Tokyo Metropolitan University (Ohashi et al. 1996, Makishima et al. 1996). GIS has large effective area (50 mm in diameter), high time resolution, and high detection efficiency at higher energies >5 keV. Fig 3.7 shows a cross section of the GIS. Design parameters and performance of the GIS is summarized in Table 3.2.

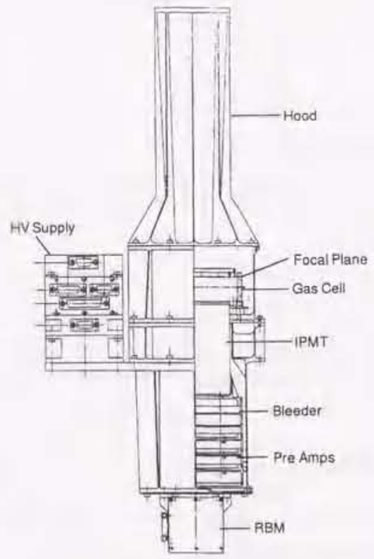

Figure 3.7: Cross section of the GIS

X-rays reflected by the XRT enter through the Be window and photo-absorbed in the drift region in the Xe gas cell. The generated primary electrons drifts to the scintillation region by the electric field ($\sim$ 1 kV cm^{-1}) and are accelerated in the strong strong electric field ($\sim$ 4 kV cm^{-1}). The electrons excite Xe and produce UV photons of λ $\sim$1700 A. These UV photons are detected by imaging photomultiplier tube through the quartz window. Then pulse hight and position is read out. In these processes, electron avalanche is not taken place and better energy resolution ($\Delta E/E$ $\sim$8% at 5.9 keV) than conventional proportional counter is obtained.

Table 3.2: Design parameters and performance of the GIS

Energy band	0.7–15 keV
Energy resolution	8% at 5.9 keV
Field of view	50 mm diameter
Positional resolution	0.5 mm (FWHM)
Time resolution	$\sim$ 61μm (Minimum in PH mode)
	1.95 msec (Minimum in MPC mode)

In orbit, the background rejection is carried out via a rise-time (RT) discrimination and a spread (SP) discrimination. The SP discrimination was enabled on May 28 1993. Therefore, we should take care the date of observation. It can reduce the non X-ray events appeared the edge of the detectors and is important to be set for the studies of extended or diffuse sources. The onboard RT acceptance window is set to be rather loose, which can be tightened further on ground in the course of data analysis. By using this tight RT window, the non X-ray background can be reduced to be $\sim$ 10 % while the X-ray is lost only 1 % (Ohashi et al. 1996). Applying SP discrimination after RT discrimination,$\sim$ 85 % of non X-ray background can be rejected and its count rate within a radius of 17$'$ is $(5-9)\times10^{-14}$ c s^{-1} cm^{-2} keV^{-1} in 1–10 keV (Makishima et al. 1996)

There are 3 observation modes of the GIS; the pulse height(PH) mode, the multichannel pulse count(MPC) mode, the position calibration(PCAL) mode. In all observations in this thesis, the GIS is operated in PH mode. PH mode is fully CPU-based data mode. After calculating the event position and applying the SP and so on, the CPU assigns each accepted event 32 telemetry bits. The 32 bits are a combination of sensor ID, pulse height, X and Y positions, rise time, spread of light signal, and the event arrival timing measured by the hard-wired logic. The bit assignment is adjustable; the nominal assignment is 1-10-8-8-5-0-0 bits.

Each sensor has the ^{55}Fe isotope ($\sim$ 0.3 c/s/GIS) attached to the edge of the entrance window to monitor the stability of the gain. The gain exhibits a temperature dependence of about 1 % per degree and a position dependence up to 20 %. These have been calibrated in orbit down to 1 % (Makishima et al. 1996). We, usually, correct the GIS by using temp2gain to compensate the gain change due to the detector temperature. The gain is corrected for the peak of Mn-Ka to be 500 channel. We correct the GIS gain by using temp2gain to compensate the gain change due to the detector temperature and the longterm gain degradation (Idesawa et al. 1997).

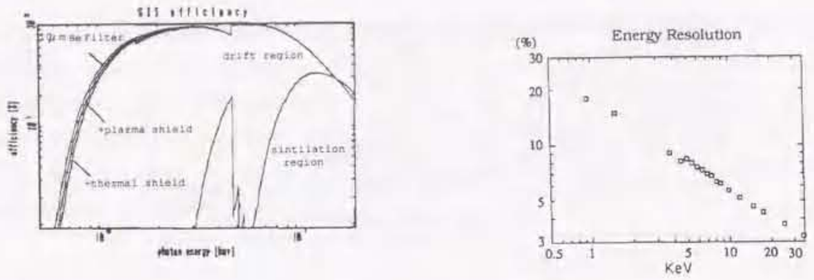

Figure 3.8: Detection efficiency (left) and energy resolution (right) of GIS

3.4 Solid state Imaging Spectrometer; SIS

The Solid state Imaging Spectrometer (SIS) is the first X-ray detector in orbit employing a Charge Coupled Device (CCD) in the photon counting mode. SIS was developed by MIT, Pennsylvania State University, ISAS, and Osaka University. SIS has superior energy resolution (2% at 6 keV) and positional resolution (pixel size of 27 μm). Fig 3.9 shows a cross section of the SIS. Design parameters and performance of the SIS is summarized in Table 3.3.

Each SIS is made of four CCD chips of 11 mm square each developed at MIT Lincoln laboratory, to achieve a 22 mm $\times$ 22 mm square area for X-ray detection. Each chip has 420$\times$422 pixels of 27 μm square each, and a depletion layer of about 40 μm thick which ensure an improved efficiency for harder X-rays than conventional CCDs.

Fig 3.10 illustrates the quantum efficiency and energy resolution of the SIS as a function of incident photon energy. The SIS sensitivity covers approximately 0.4–10 keV. The CCD chips and preamplifiers are cooled down to reduce thermal noise down to $N \sim 5$ electrons level. Thus the SIS achieves an energy resolution of about 150 eV FWHM over the whole energy range.

In order to perform proper photon-counting spectroscopy, the CCD frame must be scanned and read out fast enough so that event pile up (i.e. one pixel receiving more than one X-rays) is virtually negligible. Since the read out cycle is usually limited by the telemetry capacity, the SIS performs an extensive on-board CPU processing to compress the information. Instead of sending data from all the pixels to ground, the SIS basically picks up only those pixels in which the charge exceeds a certain threshold, and sends

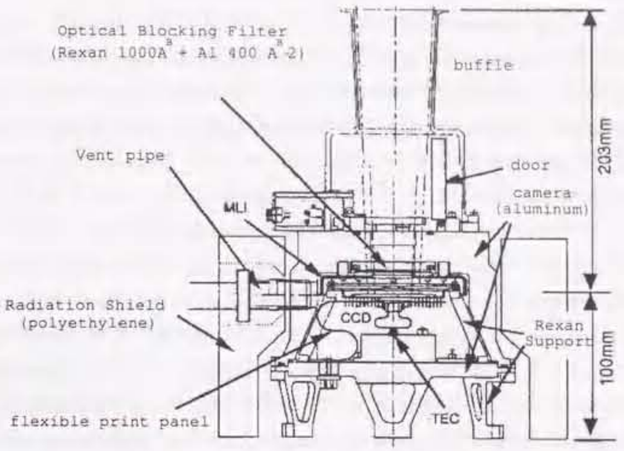

Figure 3.9: Cross section of the SIS

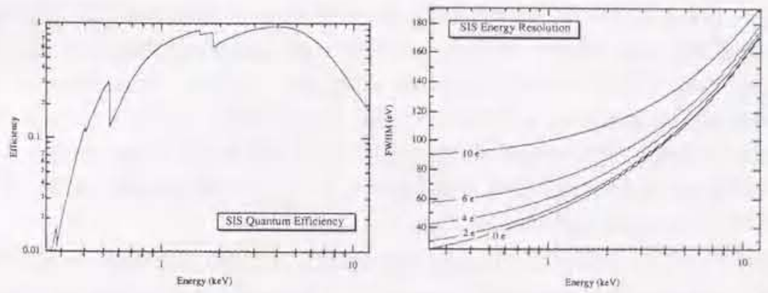

Figure 3.10: left: Detection efficiency of the SIS. K-edges of O (0.53 keV), Al (1.56 keV), and Si (1.84 keV) are seen. right: Energy resolution of the SIS as a function of incident photon energy. Energy resolution with different read-out noise N are plotted. The read-out noise levels are given as the equivalent number of electrons.

out their addresses and pulse heights. Moreover to handle targets with different X-ray intensities and angular sizes under different telemetry rates, the SIS uses four different clocking modes; 1-CCD, 2-CCD, and 4-CCD modes. In the n-CCD mode (n = 1,2,4), data from n chips for each detector are read out. In the 1-CCD mode, e.g., the usable field of view becomes limited to a quarter of the detector, but the event pile up becomes least severe so that we can use slower telemetry rates and observe brighter sources than in other clocking modes. The electrons produced in the depletion layer by an X-ray photon may be split into several adjacent pixels. The pattern of charge splitting over 3 by 3 pixels is called 'event grade'. (When the charge is spread over more than 3 by 3 pixels, the event is rejected by the on-board CPU as a background event.) In order to cope with the splitting of normal X-ray events, the SIS incorporates several data selection modes. For example in so called 'faint mode', information on a certain pixel with event detection is always accompanied by similar information on the eight surrounding pixels. We can then examine the event ground on ground, and restore the total pulse height if necessary. In so called 'bright mode', the on-board CPU automatically recognizes the charge splitting pattern, and sends the total pulse height only for events with specified even grades. The faint mode requires a larger telemetry capacity, but provides more information than the bright mode. Actually we can convert the faint mode data into the bright mode data on ground, but the reverse is impossible.

There are several additional particular phenomena in the SIS. One is called "hot pixels".

Lattice defect in the silicon substrate causes a lower resistance in the insulation of electrode of particular pixels. It leads to a spurious background spectrum similar to a real X-ray event. Such defected pixels are called as hot pixels. Discarding of the hot pixel event can be easily done because number of readout is abnormally frequent from hot pixels compared with normal X-ray events. After the launch of the satellite, number of hot pixels are increasing. This is thought to be due to an increase of lattice defect induced by the charged particles in orbit.

Another problem is the light leakage, particularly in chip2 and chip 3 of SIS 0 (S0C2 and S0C3, respectively), presumably caused by a damage in the optical blocking filter. This makes the observations with S0C2 and S0C3 almost impossible when the day earth is within $\sim 25°$ from the target. It also affects the dark current of the whole CCDs in the day time, and causes a subtle change in the energy to pulse-height relation.

"Echo" is the phenomenon where some specific fraction of a pixel's pulse height(PH) leaks to the PH of the next readout pixel. Because PH and grade of an event is calculated using the PH of event's in 3 × 3 pixels, echo affects both the grade and energy of each

photon event in a non-linear fashion. The echo values are different between the two sensors and ranging 1–2 % (Otani & Dotani 1994).

"Dark Frame Error"(DFE) is the difference between the real zero level of pixels and that estimated by the onboard software. Onboard software calculate "zero level" for each 16 × 16 pixels subsection by averaging the PH of pixels whose PH lies between −40 ADU and 40 ADU(1 ADU $\sim$ 3.5eV). DFE mainly arise from asymmetric distribution of PH around zero, and is influenced by the charges generated by X-ray photons, charged particles, and optical light leakage on the CCD chips(Otani & Dotani 1994).

There also exists a serious long-term degrading of the SIS performance due to the accumulated radiation damage (Yamashita et al. 1997; Yamashita 1995; Dotani et al. 1995). The radiation damage causes degradation of Charge transfer inefficiency (CTI) and increases dark current. CTI is defined as the fraction of lost charge per one transfer and the degradation of CTI is $\sim 1-2\times10^{-5}$ transfer^{-1} yr^{-1} . Increase of dark current of each pixel causes the scatter of dark levels among pixels and then the distribution of dark level becomes wider and asymmetric. This is called residual dark distribution (RDD). The degradation of the energy resolution due to CTI non uniformity and RDD is taken into account in the response matrices.

Furthermore the SIS background varies in a complicated way, depending on the SIS operation condition (clocking mode, data mode, split threshold, etc.), as well as the particle environment (Gendreau 1994, Ueda et al. 1996).

Table 3.3: Design parameters and performance of the SIS

Irradiation method	Front irradiation
Charge transfer method	Frame Transfer
Clock	3-phase drive
Number of pixels in image region	420 pixels × 422 lines per chip
Pixel size	27 μm (Imaging region)
	18 μm × 24 μm (Frame store region)
Area	11 × 11 mm square per chip
Field of view	11 × 11 arcmin square per chip
Thickness of Depletion layer	$\sim 40\mu$m
Drive temperature	$\sim -62°$
Energy band	0.4–12 keV
Quantum efficiency	~80% at 6 keV
Energy resolution	2% at 5.9 keV (FWHM)

Chapter 4

Observations

4.1 Observed galaxies

We compiled *ASCA* data of LINERs and low luminosity Seyfert galaxies from public archival data at the end of September 1997 as well as our own observations. Classification to LINERs or Seyferts is based on the results from Palomar survey which is recently completed (Filippenko & Sargent 1985, Ho et al. 1995, Ho et al. 1997a). Their measurements of optical emission lines are of highest quality and contains the largest number of galaxies achieved so far. We also analyzed a few galaxies which is not included in the list by Ho et al. (1995). Although NGC 4941 is located in the southern hemisphere, some authors measured their optical emission lines and information of classification/line flux is available. The analyzed galaxies are tabulated in Table 4.1. Among galaxies classified as Seyferts, we analyzed low luminosity ones with Hα luminosity log $L_{\mathrm{H}\alpha}$ <40.5 ergs s^{-1}. Since Hα luminosity of the low luminosity Seyfert 1 galaxy NGC 4051, which has been extensively studied in various wavelengths, is logHα =40.32 ergs s^{-1}, Seyfert galaxies in our sample is much less luminous than Seyfert galaxies previously studied. Hα luminosities are summarized in Appendix A.

Our sample is not a complete one and biased to more active galaxies. Most of galaxies have broad Hα. In some cases there exists radio jets, optical jets, a compact radio core, an X-ray nucleus, and so on. Therefore the sample galaxies have more probability to host active nucleus compared to uniformly sampled LINERs.

In Table 4.1, positions, morphological types, classifications of optical emission lines and the presence of broad Hα are shown . Distances are taken from Tully (1988) and we assume the Hubble constant H_0=75 km s^{-1} Mpc^{-1} throughout this thesis.

4.2 Data reduction

ASCA observations are summarized in Table 4.2. We applied the nominal data selection criteria: times were excluded when the elevation angle from the earth rim was less than 5 degrees, the geomagnetic cut off rigidity was less than 6 GeV c^{-1}, and the telescope was in the South Atlantic Anomaly. Additionally the condition that the elevation angle from the day-Earth rim was greater than 25 degrees was also applied to the SIS data.

We converted the Faint mode data to the Bright mode for the objects observed in Faint and Bright mode, and added together to improve photon statistics, but for NGC 4579. Since the SIS sensors were operated in Faint mode during most of the observation time for NGC 4579, we used only Faint mode data.

The obtained effective exposure time and count rates after date screening are summarized in Table 4.3.

4.3 Spectral analysis

We used XSPEC version 9.00 in the XANADU software package for spectral fitting. An X-ray spectrum is extracted from a circular region of radius 4' for SIS and 6' for GIS, unless otherwise mentioned. In some cases, there are some sources near the main target and smaller region is used. A background spectrum is made using off source region in the same field. We used the response matrices of version 4.0 for the GIS detectors and made by sisrmg in ftools version 3.6 for the SIS detectors. The ARF response is made by a combination of jbldarf-2.10 and arffilter. Although obtained X-ray image is extended in some cases, we assumed point source to make an ARF response; spatial extension is small for all the cases, and this assumption provides good approximation.

The X-ray spectrum is binned so that each bin contains at least 20 counts and chi-square minimization technique is used. All errors are quoted at 90% confidence level for one parameter of interest ($\Delta\chi^2$=2.7; Lampton et al. 1976), unless otherwise quoted. The spectral fittings are done simultaneously for SIS and GIS data. The calibration uncertainty of normalizations between four detectors are typically several percent and we assumed the same normalization for SIS and GIS otherwise noted.

4.4 Previous observations of individual objects

NGC 404 is a nearby face-on S0 galaxy at a distance of 1.8 Mpc. The optical emission lines are classified to LINER and no broad Hα is detected (Ho et al. 1997a, b). There

are strong Hydrogen Balmer absorption lines in the optical spectrum (Ho et al. 1995). A UV image is taken with *HST* FOC and the probably unresolved bright core, surrounding several point sources, and some diffuse emission are detected. If number of ionizing photons is calculated assuming $f_\nu \propto \nu^{-1}$, the UV luminosity of the nucleus is sufficient to the luminosity of the Hydrogen recombination lines through photoionization (Maoz et al. 1995). On the other hand, UV spectra obtained with *HST* FOS show blueshifted CIV absoption and narrow absorption lines which indicate the UV emission is originated from a star cluster (Maoz et al. 1998). No X-ray results are reported so far.

NGC 1052 is a E4 galaxy at a distance of 17.8 Mpc and has a LINER nucleus. The LINER in this galaxy has been known since 1970's and shock models are extensively calculated to explain optical emission lines (Koski & Osterbrock 1976, Warner 1977, Fosbury et al. 1978). A broad Hα is present in the optical spectrum. NGC 1052 is also a H_2O megamaser source (Braatz, Wilson, & Henkel 1994). A *ROSAT* PSPC spectrum is significantly harder than typical elliptical galaxies and it is suggested that emission from the AGN contributes to the soft X-ray emission (Davis & White 1996.

NGC 2273 is a low luminosity Seyfert 2 galaxy (Huchra, Wyatt, & Davis 1982) with an Hα luminosity of log $L_{\rm H\alpha}$=40.41 ergs s^{-1} (Ho et al. 1993a).

NGC 3079 is a nearly edge-on Sc galaxy with starburst activity. The nucleus of NGC3079 indicates strong [OII]λ3727 (Heckman, Balick, & Crane 1980) and [OI]λ6300 (Ho et al. 1997a) relative to [OIII]λ5007, which is classified as a LINER or Seyfert 2 (Ho et al. 1997a). A compact nuclear radio source with a flat spectrum and a radio lobe are present (Hummel, van der Hulst, & Dickey 1984, Duric & Seaquist 1988). A strong starburst activity is present and the optical emission lines indicate that the gas is outflowing along the minor axis of the galaxy probably due to the starburst, although some contribution from an AGN cannot be excluded (Heckman, Armus, & Miley 1990, Filippenko & Sargent 1992, Veilleux et al. 1994). Although the presence of broad broad Hα is suspected by Stauffer (1982) and Keel (1983), Ho et al. (1997b) argue that it is premature to come to any firm conclusions because of difficulty of the modeling of the line profile due to complex velocity field of the line emitting gas.

X-ray obsarvations with *Einstein* IPC and *ROSAT* PSPC detected diffuse emission extends to the minor axis of the galaxy with a soft spectrum ($kT \sim 0.5$ keV). The X-ray luminosity of the diffuse emission is log $L_{\rm X} = 40.46$ ergs s^{-1} in the 0.1–2.0 keV band. An X-ray source is also detected at the nucleus. The X-ray spectrum of the nuclear source is soft ($kT \sim$1.1 keV) and probably not dominated by X-rays from the AGN (Read et al. 1997).

NGC 3998 is a S0 galaxy with a LINER nucleus. Broad Hα and Hβ are present in the optical spectra(Ho et al. 1997b). Broad MgΛ2800 is also detected in the UV spectrum (Reichert et al. 1992). *HST* FOC observations show the presence of unresolved nuclear source (Fabbiano, Fassnacht, & Trinchieri 1994).

X-ray emission is detected by *Einstein* and *Ginga* observations. *Einstein* IPC image is consistent with point line and its luminosity is 3×10^{41} ergs s^{-1} (Fabbiano, Kim, & Trinchieri 1992). Ginga observation (Awaki et al. 1992) detected X-ray emission with a luminosity of 1.0×10^{42} ergs s^{-1} (at 25 Mpc) and its spectrum is represented by a power-law with a photon index of 2.0. There is no indication of an iron K emission line. No significant time variability within one day is detected.

NGC 4203 is a Sa galaxy at a distance of 9.7 Mpc. Optical emission lines of the nucleus are clssified as LINER and broad Hα is detected (Ho et al. 1997a, b). VLA observations at 6 cm revealed a central radio source (Fabbiano, Gioia, & Trinchieri 1989). A UV image taken by *HST* WFPC2 through F218W filter shows the presence of faint unresolved central source (Barth et al. 1996, 1998). The UV flux is sufficient to explain optical emission line fluxes under assumption of spectral slope $f_\nu \propto \nu^{-1}$.

X-ray observations were done by the *Einstein* and *ROSAT* satelite. A net exposure time of the *Einstein* observation is too short ($\sim$ 1.6 ksec) and detaled imaging and spectral information is not available. A point source with a luminosity of 4.8×10^{40} ergs s^{-1} (at a distance of 22.5 Mpc) is detected at the nucleus by *ROSAT* PSPC observations (Bregman, Hogg, & Roberts 1995). The *ROSAT* PSPC spectrum of the nuclear source is represented by a power-law of $\Gamma = 2.24$ and log$N_{\rm H}$=20.40 cm^{-2}, which is consistent with *ROSAT* PSPC results of Seyfert 1 galaxies and some low luminosity AGNs ($\Gamma \sim 2.6$, Koratkar et al. 1995). No diffuse emission cannot be seen in the PSPC image because of a bright nuclear source, although diffuse may be expected in the buldge of early type spiral galaxies.

NGC 4438 is an early type spiral galaxies (Sa/0 and Sa) in the Virgo cluster of galaxies and interacting with NGC 4435. The LINER optical emission lines of NGC 4438 are come from an extended region (Filippenkko & Sargent 1985). A very weak broad Hα is present (Ho et al. 1997b). An UV image taken with *HST* FOC shows only a weak amorphous patch of UV emission of about 5" in size and no UV nucleus is present (Maoz et al. 1996, Maoz 1996).

NGC 4450 is an Sab galaxy at a distance of 16.8 Mpc. The optical spectra of the nucleus is classified as a LINER (Ho et al. 1997a, Stauffer 1982). A fairly weak broad Hα is probably present (Ho et al. 1997b). An *Einstein* IPC obsercation detected X-ray emission with a luminosity of 1×10^{41} ergs s^{-1} at 27 Mpc (Fabbiano et al. 1992). The spectum obtained with IPC is very soft compared to other spiral galaxies (Kim, Fabbiano, & Trinchieri 1992) and *ROSAT* PSPC observation confirmed a soft spectrum. The *ROSAT* PSPC spectrum is represented by either a 2-kT thermal ($kT_1 > 1.3$ keV, $0.13 < kT_2 < 0.16$ keV) or a power-law model with $\alpha \sim 2 - 2.5$ (Fabbiano 1996).

NGC 4565 is a nearly edge on spiral galaxy with the prominent dust lane at a distance of 9.7 Mpc. The optical spectrum of the nucleus is classified as a Seyfert 2 based on emission line ratios. A weak broad Hα is seen in the spectrum after the fitting of the narrow lines by Ho et al. (1997b). The soft X-ray observations are done with Einstein (Fabbiano et al. 1992) and ROSAT PSPC (Vogler, Pietsch, & Kahabka 1996). The *ROSAT* PSPC image shows several point sources within galaxies and extended emission from a hot gas. The prominent sources are the nuclear source and the off center source by $\sim$ 0.8'from the nucleus and these sources emit about 85% of the total X-ray emission. The X-ray luminosities of each source is $\sim 3 \times 10^{39}$ ergs s^{-1}, while the luminosity of the diffuse emission is $\sim 4 \times 10^{39}$ ergs s^{-1} in the 0.1–2.4 keV band (Vogler et al. 1996).

NGC 4569 is a Sab galaxies in the Virgo cluster of galaxies. The optical spectrum of the nucleus is classified as a transition object between an HII nucleus and a LINER and shows strong Balmer absorption which indicates A stars dominate the optical light (Ho et al. 1997a). No broad Hα is present (Ho et al. 1997b). The bright source at the nucleus and some diffuse emission are detected in the *HST* FOC image at $\sim$ 2300 A (Maoz et al. 1995). If number of ionizing photons is calculated assuming $f_\nu \propto \nu^{-1}$, the UV luminosity of the nucleus is sufficient to the luminosity of the Hydrogen recombination lines through photoionization. An *HST* WFPC2 image through F218W filter shows the nucleus is extended (Barth et al. 1996a). The UV emission line CIV show P Cygni profile, which are the signatures of winds from massive stars, and absorption lines due to the photosphere of hot stars. These spectral properties indicate that the UV emission is dominated by a cluster of massive stars (Maoz et al. 1998).

NGC 4579 (M58) is a Sab galaxy in the Virgo cluster of galaxies and classified as a LINER or Seyfert 1.9 galaxy based on the optical emission lines (Ho et al. 1997a, Keel 1983, Stauffer 1982) and the broad Hα component with FWHM $\sim$ 2300 km s^{-1} is detected (Ho et al. 1997b). There exists a flat-spectrum radio core (Hummel et al. 1987). An *Einstein* HRI observation showed the presence of an unresolved X-ray nucleus and the X-ray flux was measured to be $F_{\rm X} = 7.9 \times 10^{-12}$ ergs s^{-1} cm^{-1} in the 0.2–4.0 keV band with the *Einstein* IPC (Fabbiano, Kim, & Trinchieri 1992, Halpern & Steiner 1983) which corresponds to the X-ray luminosity of 2.7×10^{41} ergs s^{-1}. These facts indicate the presence of a low luminosity AGN in this galaxy. A recent ultraviolet imaging observation by *HST* Faint Object Camera (FOC) detected a point source at the nucleus (Maoz et al. 1995). Its UV spectra were taken by *HST* Faint Object Spectrograph (FOS) and a featureless

UV continuum is detected as well as various emission lines. Comparison of the FOC and FOS data also indicate a factor of 3.3 decrease of UV flux in 19 months. The narrow UV emission lines are incompatible with shock excitation model and a photoionization model is preferred (Barth et al. 1996). Several broad UV emission lines are also detected. These UV results provide further support for the presence of a low luminosity AGN in NGC 4579. On the other hand, Maoz et al. (1998) estimated the ionizing photon number by extrapolating the UV luminosity at 1300 A towards higher energies and argued that observed UV continuum is not sufficient to explain Hα luminosity. They also suggest that emission from AGNs is most prominent at higher energies than UV. Measurements of an X-ray flux and continuum slope provide information on the ionization source in this LINER.

NGC4594 (M104) is a Sa galaxy well known as the Smbrero galaxy and its nicleus shows LINER emission lines (Ho et al. 1997a, Keel 1983, Stauffer 1982). Broad Hα is detected in the optical spectrum obtained by a recent *HST* FOS observation (Kormendy et al. 1997). A compact nuclear UV source has been found in *HST* FOC images at $\sim$ 3400 A (Crane et al. 1993). The UV spectrum shows weak and narrow emission lines on top of a UV continuum. Nicholson et al. (1997) favor an AGN as an origin of UV emission. The presence of a super massive blackhole with mass $M \sim 10^9 M_\odot$ at the center is suspected from the motioin of the gas around the nucelus (Kormendy et al. 1996, Kormendy & Richstone 1995 and references therein). There exists a variable compact radio nucleus (Bajaja et al. 1988) An *Einstein* IPC image shows extended X-ray halo similar to elliptical galaxies (Forman, Jones, & Tucker 1985). A point source at the nucleus is detected in an high resolution X-ray image with *ROSAT* HRI as well as clumpy emission associated with the isk of NGC 4594, and diffuse emission from the bulge (Fabbiano & Juda 1997). The X-ray lluminosity of the nuclear component is $\sim 3.5 \times 10^{40}$ ergs s^{-1} at 18 Mpc in the 0.1–2.4 keV band which is about half of the total X-ray luminosity. A *ROSAT* PSPC spectrum of the nucleus is fitted with power-law with photon index of $\sim$ 1.8. Time vatiability is also suggested from an HRI light curve.

NGC 4736 is a nearby (4.3 Mpc) Sab galaxy with strong Balmer absorption lines in the optical spectra of the nucleus (Filippenko & Sargent 1985, Ho et al. 1995). The nucleus shows strong [NII]λ6583 and classified to a LINER. Taniguchi et al. (1996) performed the stellar population synthesis and found that NGC 4736 is dominated by A-type stars with ages of 10^9 yr and that a luminous starburst occured 1×10^9 years ago. Their results indicate optical emission line ratios are located at the region between HII and LINER on the excitation diagrams. In *HST* FOC image at 2200 A, two compact sources os approximately equal brightness separated by 2".5 are detected (Maoz et al. 1995). A

starforming ring is present at a radius of 50" ($\sim$ 0.7 kpc). *ROSAT* PSPC detected nuclear X-ray source of linuminositof 3.4×10^{39} ergs s^{-1} (0.1–2 keV) and diffuse emission. No variability is seen on time scale of minuites to hours (Cui et al. 1997).

NGC 4941 is a nearby (6.8 Mpc) galaxies with a Seyfert 2 nuclei which is dicoverd in the optical spectroscpic survey by Keel (1993). *BeppoSAX* detected a strong iron K emission of equivalent width of $\sim$ 1 keV at 6.4 keV (Salvati et al. 1997). The X-ray continuum is fitted with either a pure reflection model or partial covering model.

NGC 5005 is a bright starburst galaxies. Optical emission lines of the nucleus is classified to LINER and broad Hα is suggested (Ho et al. 1997a, b). No UV nucleus is detected in an *HST* WFPC2 image at λ=2190A (Barth et al. 1996) and an *HST* FOC image at $\sim$ 2300 A (Maoz 1996), either, but extended emission is detected (Barth et al. 1998). An X-ray image obtained with *ROSAT* PSPC shows a extended nucleus and diffuse emission. The spectrum of nuclear source is represented by $kT \sim 1$ keV thermal emission with a X-ray luminosity of $\log L_X = 40.47$ ergs s^{-1} in the 0.1–2 keV band at a distance of 21.3 Mpc. The ' plume-like' extended emission is probably due to a galacic wind.

NGC 5033 The optical emission lines are classified as Seyfert 1.5 or LINER and the prominent and variable broad Hα has been observed in the optical spectrum (Shuder 1980, Stauffer 1982, Filippenko & Sargent 1985, Koratkar et al. 1995, Ho et al. 1997b). NGC5033 is detected in X-rays by *Einstein* IPC (Halpern & Steiner 1982) and *ROSAT* HRI observations (Koratkar et al. 1995). The ROSAT HRI image of the X-ray nucleus is point-like and the X-ray luminosity is log L_X=41.41 ergs s^{-1}(0.2-2.2 keV) (Koratkar et al. 1995).

NGC 5194 (M51) is a nearby spiral galaxy known as the 'whirlpool galaxy' and has been intensively studied at various wavelengths. On the basis of optical emission line studies the M51 nucleus has been classified as a Seyfert 2 or a LINER (low ionization nuclear emission-line region) (Stauffer 1982; Filippenko & Sargent 1985; Ho, Filippenko, & Sargent 1997). The presence of broad Hα is suspected by Ho et al. 1997b.

The *Einstein* HRI detected X-ray emission from M51 with a luminosity $L_X = 3.0 \times 10^{40}$ ergs s^{-1} in the 0.2–4.0 keV band at 9.6 Mpc (Sandage & Tammann 1975). However the HRI image of the nucleus is clearly extended and provides only an upper limit ($L_{0.2-4.0\ \mathrm{keV}} < 1.5 \times 10^{39}$ ergs s^{-1}) for the luminosity of a point source at the nucleus (Palumbo et al. 1985). A *ROSAT* HRI observation confirmed that the X-ray source at the nucleus is extended (Ehle, Pietsch, & Beck 1995). The *ROSAT* PSPC spectrum of the M51 nucleus is fitted with a $kT \sim$0.4 keV thermal plasma model (Marston et al. 1995; Read, Ponman, & Strickland 1997). Such a soft X-ray spectrum also supports the idea that

the AGN does not dominate the nuclear soft X-ray emission. The *ROSAT* PSPC and HRI also detected eight point sources with X-ray luminosities around 10^{39} ergs s^{-1} in M51 superposed on diffuse X-ray emission. A *Ginga* observation detected hard X-ray emission with a photon index $\Gamma = 1.4$ and a X-ray luminosity in the 2–20 keV bandpass of $(1.2 \pm 0.6) \times 10^{41}$ ergs s^{-1} from a ~ 1 deg^2 field containing M51 (Makishima et al. 1990). The *Ginga* spectrum can also be fit with a kT=7 keV thermal bremsstrahlung plus a power-law ($\Gamma = 1.6$) absorbed with $N_H \sim 4 \times 10^{23}$ cm^{-2}. Makishima et al. (1990) proposed a scenario to explain both the *Einstein* and *Ginga* data in which the active nucleus is obscured and only the harder portion of the spectrum is dominated by X-rays from an active nucleus. The visual and UV band images taken by *Hubble Space Telescope* show X-shaped dust lanes (Maran & Kinney 1993; Maoz et al. 1996). A dense molecular disk with $N_H > 3.0 \times 10^{23}$ cm^{-2} around the nucleus is also revealed by HCN ($J = 1 \rightarrow 0$) and CO ($J = 1 \rightarrow 0$) observations (Kohno et al. 1996). Some of this material may account for the X-ray absorbing material.

NGC 5195 is the companion galaxy of the 'Whirlpool galaxy' M51 (NGC 5194) and interacting with it. The optical spectrum of the nucleus shows deep Balmer absorption lines (Filippenko & Sargent 1985, Ho et al. 1995, Yamada private communication). The optical emission lines are classified to a LINER ot transition between LINER and HII nucleus (Ho et al. 1997a). No broad Hα (Ho et al. 1997b) and no UV nucleus is observed (Maoz 1996, Barth et al. 1996b). X-ray observations were performed with *Einstein* HRI and *ROSAT* PSPC and HRI (Palumbo et al. 1985, Marston et al. 1995, Ehle et al. 1995, Read et al. 1997). No clear point nucleus is seen in the X-ray images although extended X-ray emission is detected.

NGC 7217 The optical emission lines are classified to a LINER and no broad Hα is detected (Ho et al. 1997a, b). UV nucleus is not deteced in *HST* WFPC2 image at 2190 A (Barth et al. 1996).

Table 4.1: Observed galaxies

name		Type	distance[a]	redshift[b]	class[c]	references[d]
NGC404		S0.3	2.4	–0.00016	L2	
NGC1052		E3/S0	17.8	0.00490	L1.9	
NGC1667		S(r)c I-II	61.2	0.01517	S2	
NGC2273		SB(rs)0/a	28.4	0.00614	S2	
NGC3079		S(s)c II-III	20.4	0.00375	S2	
NGC3998		$S0_1(3)$	21.6	0.00347	L1.9	
NGC4203		$S0_2(1)$	9.7	0.00362	L1.9	
NGC4438		Sb(tides)	16.8	0.00024	L1.9	
NGC4450		Sab pec	16.8	0.00652	L1.9	
NGC4565		Sb	9.7	0.00409	S1.9	
NGC4569	M90	S(s)ab I-II	16.8	–0.00078	T2	
NGC4579	M58	S(s)ab II	16.8	0.00507	S1.9/L1.9	
NGC4594	M104	Sab	20.0	0.00364	L2 [e]	
NGC4736	M94	RS(s)ab	4.3	0.00103	L2/T	1
NGC4941		(R)SAB(r)ab	6.4	0.00370	S2	2
NGC5005		S(s)b II	21.3	0.00316	L1.9	
NGC5033		S(s)b I	18.7	0.00292	S1.5	
NGC5194	M51	S(s)bc I-II	7.7	0.00154	S2	
NGC5195		$SB0_1$ pec	9.3	0.00155	L2:	
NGC7217		S(r)b II-III	16.0	0.00316	L2	

a: taken from Tully (1988); b: taken from NASA Extragalactic Database; c: S = Seyfert nucleus, L = LINER, T = transition between LINER and HII nucleus, 1.5/1.9/2 = types, ":" denotes ambiguous classification.; d: 1: Taniguchi et al. 1996, 2: Keel 1983, others: Ho, Filippenko & Sargent 1997a; e: The presence of broad Hα is reported by Kormendy et al. (1996).

Table 4.2: *ASCA* observation log

name	date	begin	end	period	SIS mode
	yymmdd	hhmm	hhmm		
NGC404	970721	1034	2310	AO5	1CCD faint
NGC1052	960811	0216	0846	AO4	1CCD faint
NGC1667	940306	0840	0825	AO1	2CCD faint
NGC2273	961020	1223	1040	AO4	1CCD faint 0.48 keV LVL ON
NGC3079	930509	0255	0318	PV	1CCD faint/bright
NGC3998	940510	1945	1140	AO2	2CCD/1CCD faint
NGC4203	931217	0235	0220	AO1	2CCD faint
NGC4438	951224	2134	1010	AO4	2CCD/1CCD faint
	960105	1754	0620	AO4	1CCD faint/bright
NGC4450	950620	0504	0951	AO3	1CCD faint
NGC4565	940528	1904	2020	AO2	2CCD faint
NGC4569	970624	1035	0230	AO5	1CCD faint
	970706	0011	1230	AO5	1CCD faint
NGC4579	950625	0530	0951	AO3	2CCD faint/bright
NGC4594	940120	0139	1721	AO1	2CCD faint
NGC4736	950525	1726	1940	AO3	1CCD faint 0.41keV LVL ON
NGC4941	960719	1313	0820	AO4	1CCD faint
	970108	0555	1840	AO4	1CCD faint
NGC5005	951213	0737	0800	AO4	1CCD faint
NGC5194	930511	0321	0135	PV	4CCD faint/bright
NGC5195	930511	0321	0135	PV	4CCD faint/bright
NGC5033	951214	0801	0800	AO3	1CCD faint
NGC7217	951119	2135	0101	AO4	2CCD faint/bright

Table 4.3: Count rates and exposure time

name	SIS count rate [counts s^{-1}]	(0.5–10 keV) exposure [ksec]	GIS count rate [counts s^{-1}]	(0.7–10 keV) exposure [ksec]
NGC404	—	12.3	—	13.4
NGC1052	0.046	36.5	0.041	37.7
NGC1667	0.006	39.9	0.001	43.8
NGC2273	0.004	36.1	0.013	38.4
NGC3079	0.022	37.2	0.008	41.1
NGC3998	0.29	24.3	0.18	39.7
NGC4203	0.035	35.1	0.024	38.1
NGC4438	0.014	43.0	0.005	45.2
NGC4450	0.026	37.4	0.015	36.7
NGC4565	0.056	37.4	0.036	38.8
NGC4569	0.017	40.9	0.007	41.4
NGC4579	0.15	32.0	0.090	30.9
NGC4594	0.075	18.7	0.060	19.7
NGC4736	0.073	28.4	0.042	31.2
NGC4941	0.009	36.5	0.009	35.3
NGC5005	0.024	35.9	0.012	38.3
NGC5033	0.16	36.1	0.11	38.6
NGC5194	0.044	34.6	0.020	38.5
NGC5195	0.012	34.6	0.006	38.5
NGC7217	0.008	81.0	0.004	80.9

Chapter 5

Results

5.1 Spectral fitting

5.1.1 power-law model

AGNs show X-ray spectrum represented by a power-law model modified by absorption due to cold matter. We first fit the spectrum with a absorbed power-law model:

$$N(E)dE = AE^{-\Gamma}\exp(-\sigma(E)N_{\rm H}),$$

where A is a normalization factor, and the absorption cross section by Morrison & MacCammon (1983) is adopted for $\sigma(E)$.

The fitting results with this model is shown in Table table:PLfit. This simple model provide acceptable fits only for three objects; NGC 3998, NGC 4203, and NGC 5033. NGC 3998 and NGC 5033 exhibit a emission line like feature around 6.4 keV. This feature is well modeled by adding a Gaussian component (see §5.1.4).

In some cases, X-ray continuum in the hard band suffers from large absorption ($N_{\rm H}>10^{22}$ cm^{-2}) and less absorbed component is also present in the soft energy band. NGC 1052, NGC 2273, NGC 4565 [1] , and NGC 4941 belong to this category. We examined partial covering model as is seen in Seyfert 2 galaxies. (Many Seyfert 2 galaxies show two component X-ray continua; heavily absorbed power-law and less absorbed component. The less absorbed continuum is interpreted to be scattered radiation from the nucleus or leaked emission from 'leaky absorber' and/or a starburst component.) The model function

$$F(E)dE = \exp(-\sigma(E)N_{\rm H1})A[E^{-\Gamma}\{f\exp(-\sigma(E)N_{\rm H2}+(1-f)\}],$$

[1]The X-ray spectrum of NGC 4565 fitted here is sum of emission from the nuclear source and off center source. The off center source is about two times brighter than the nucleus. See §5.5.4 for details.

is fitted for these objects. As NGC 1052, NGC 2273, and NGC 4941 show line emission around 6.4 keV, we added a Gaussian and obtained good fit. The results of partial covering model is shown in Table 5.3.

As shown in the following subsections, other galaxies in our sample show a soft component accompanied by several emission lines. Fig 5.1 shows an example of a power-law model fit to the SIS spectrum of M51 (NGC 5194). Emission line-like residuals are seen around 0.65 keV, 0.9 keV, 1.0 keV, 1.3-1.4 keV, and 1.8 keV, which are identified as H-like O-K, He-like and H-like Ne-K, He-like and H-like Mg-K, He-like Si-K emission lines. These emission lines suggest the presence of a thermal plasma of $kT = 0.5 - 1$ keV. Therefore we tried to add a thermal plasma model to the power-law continuum model.

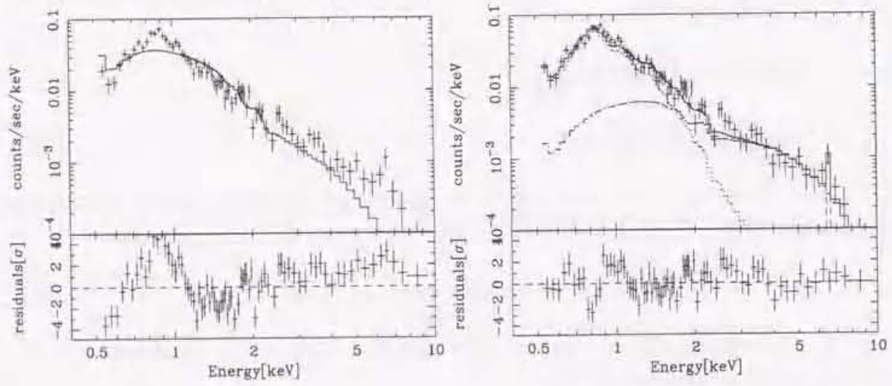

Figure 5.1: left: *ASCA* SIS spectrum of M51 fitted with a single power-law model. right: *ASCA* SIS spectrum of M51 fitted with a Raymond-Smith thermal plasma + single power-law model.

5.1.2 Raymond-Smith + Power-law model

We introduced the Raymond-Smith thermal plasma model (Raymond & Smith 1977) in addition to a power-law or partially covered power-law model examined above:

$$F(E)dE = \exp(-\sigma(E)N_{\rm H1})[RS(kT, A, EM) + AE^{-\Gamma}\exp(-\sigma(E)N_{\rm H2}],$$

or

$$F(E)dE = \exp(-\sigma(E)N_{\rm H1})[RS(kT, A, EM) + AE^{-\Gamma}\{f\exp(-\sigma(E)N_{\rm H2} + (1-f)\}],$$

where kT, A, EM are the electron density, abundance, and emission measure of the plasma, respectively. The definition of solar abundance by Anders & Grevesse (1989) is used throughout.

This model significantly improves the fit compared to a power-law or partially covered power-law model for all the galaxies, but for objects well fitted with the simple model, and acceptable fit is obtained for most of the galaxies. The best fit parameters are summarized in Table 5.4. NGC 1052 and NGC 4579 shows a emission line at ~ 6.7 keV and a Gaussian is added to the model (see §5.1.4).

5.1.3 variable abundance Raymond-Smith + power-law model

Some objects clearly exhibit O-K, Ne-K, Mg-K emission lines but weak iron-L line complex in their spectra. Fig 5.1 shows an example of such class of objects M51 (NGC 5194) fitted with a Raymond-Smith plasma + power-law model, where the relative abundance of various metals is assumed to be solar ratio. Such apparently smaller iron abundance compared to abundance of α elements is observed in several starburst galaxies. Since many galaxies in our sample exhibit starburst activity, such appearance of emission lines may be attributed to hot gas produced by starburst.

We tried variable abundance Raymond-Smith model + power-law model, where abundance of iron and α elements are varied separately. The fitting results are tabulated in Table 5.5. The fit is improved for NGC 3079, NGC 4450, NGC 4594, NGC5194 (M51).

5.1.4 Iron K emission

Seyfert galaxies generally show fluorescence iron K emission. In order to evaluate the intensity of iron emission, we add a Gaussian to the best fit continuum model of each galaxies. If significant iron K emission is not detected, we add a narrow Gaussian at 6.4 keV or 6.7 keV and calculate upper limits of equivalent widths. Improvement of chi-square and obtained equivalent widths are shown in Table 5.7. Statistically significant iron emission is detected from NGC 1052, NGC 2273, NGC 4579, NGC 4941, NGC 5033, NGC 5194 (M51). From NGC 3998 and NGC 4736, we detected a marginal iron emission. For these objects, the center energy of the iron line is shown in Table 5.6.

Table 5.1: Results of power-law fit

name	$N_{\rm H}$ $[10^{22}$ cm$^{-2}]$	Γ	χ^2/dof	notes
NGC1052	0.0	0.20	240.8/111	
NGC1667	$0(<0.16)$	$2.3^{+0.8}_{-0.4}$	13.5/18	
NGC2273	0.0	0.94	32.5/15	1,3
NGC3079	0	2.38	137.6/93	
NGC3998	0.088 ± 0.012	1.89 ± 0.03	332.0/280	1
NGC4203	$0.024(<0.056)$	1.77 ± 0.08	46.2/71	
NGC4438	0	2.68	58.0/42	
NGC4450	$0(<0.043)$	$1.89^{+0.14}_{-0.08}$	72.1/70	
NGC4565	0.22	1.81	163.7/112	
NGC4569	0	2.18	123.0/45	
NGC4579	0.046	1.78	250.5/206	2
NGC4594	0.056	1.61	138.7/88	
NGC4736	0	1.98	225.3/107	
NGC4941	0	0.52	134.9/55	
NGC5005	0	2.05	144.7/60	
NGC5033	0.087 ± 0.017	1.72 ± 0.04	173.3/188	1
NGC5194	0	2.82	482.3/146	
NGC5195	0	2.68	81/23	
NGC7217	0.0	1.78	92.8/59	

1: including an iron emission line at 6.4 keV. 2: including an iron emission line at 6.7 keV. 3: only SIS spectrum is fitted.

Table 5.2: Results of power-law fit in the 2–10 keV band

name	$N_{\rm H}$ $[10^{22}$ cm$^{-2}]$	Γ	χ^2/dof	notes
NGC1052	13 ± 5	$1.63^{+0.39}_{-0.45}$	59.4/50	1,3
NGC3079	$0(<2.9)$	$1.7^{+1.1}_{-0.4}$	39.4/35	
NGC3998	$0(<0.26)$	$1.82^{+0.09}_{-0.05}$	152.5/149	1
NGC4438	$1.1(<8.0)$	$2.5^{+2.4}_{-0.9}$	9.9/9	
NGC4203	$0.69(<1.8)$	$1.84^{+0.33}_{-0.28}$	15.9/26	
NGC4450	$0(<0.83)$	$1.68^{+0.38}_{-0.30}$	23.7/27	
NGC4565	$1.6^{+1.0}_{-0.9}$	2.52 ± 0.36	70.1/53	
NGC4569	$2.4(<5.9)$	$2.8^{+1.4}_{-1.0}$	19.3/13	
NGC4579	$0(<0.48)$	$1.76^{+0.19}_{-0.08}$	115.2/110	2
NGC4594	$1.1^{+1.0}_{-0.9}$	$2.10^{+0.45}_{-0.34}$	40.2/40	
NGC4736	$0(<0.58)$	$1.57^{+0.23}_{-0.13}$	53.4/47	
NGC5005	$0(<1.0)$	$1.22^{+0.43}_{-0.34}$	32.0/24	
NGC5033	$0.06(<0.58)$	$1.66^{+0.19}_{-0.08}$	119.1/102	1
NGC5194	$0(<0.49)$	$1.67^{+0.27}_{-0.24}$	62.0/54	1
NGC5195	$0(<3.0)$	$2.2^{+1.0}_{-0.7}$	4.6/3	
NGC7217	$1.2(<4.5)$	$2.5^{+1.2}_{-0.8}$	38.4/27	

1: including an iron emission line at 6.4 keV. 2: including an iron emission line at 6.7 keV. 3: results of fitting in the 3.5–10 keV band. (The soft component makes significantly contribution up to ~ 3 keV).

Table 5.3: Results of partial covered power-law fit

name	$N_{\rm H}1$ $[10^{22}$ cm$^{-2}]$	$N_{\rm H}2$ $[10^{22}$ cm$^{-2}]$	C.F.	Γ	χ^2/dof	notes
NGC1052	$0(<0.034)$	9.5 ± 1.6	$0.77^{+0.05}_{-0.07}$	$1.11^{+0.14}_{-0.41}$	128.6/107	1
NGC2273	$0(<)$	46^{+11}_{-13}	$0.94^{+0.02}_{-0.03}$	$1.4^{+0.5}_{-0.4}$	70.9/56	1
NGC4565	0.30 ± 0.07	2.6 ± 0.8	$0.65^{+0.11}_{-0.14}$	2.60 ± 0.32	140.6/110	
NGC4941	$0.18(<0.56)$	100^{+50}_{-30}	$0.962^{+0.023}_{-0.050}$	$1.50^{+0.58}_{-0.48}$	43.5/51	1

1: including an iron emission line at 6.4 keV. 2: including an iron emission line at 6.7 keV.

Table 5.4: Results of power-law + Raymond-Smith model fit

name	$N_{\rm H}$ [10^{22} cm^{-2}]	kT [keV]	abundance [solar]	$N_{\rm H}$ [10^{22} cm^{-2}]	Γ	χ^2/dof	
NGC1052	0.030(f)	$1.0^{+2.2}_{-0.3}$	0.04(< 0.10)	$20.0^{+7.0}_{-8.3}$	$1.67^{+0.57}_{-0.40}$	104.4/104	
				$2.5^{+2.7}_{-1.4}$	(CF $0.77^{+0.08}_{-0.10}$)		
NGC1667	0.055(f)	$0.81^{+0.20}_{-0.55}$	0.1(f)	$1.4^{+3.6}_{-1.4}$	1.8(f)	10.3/17	
	0.055(f)	$0.75^{+0.27}_{-0.46}$	0.5(f)	0(< 0.44)	1.8(f)	10.3/17	
NGC3079	0.01(f)	$0.34^{+0.09}_{-0.07}$	0.1(f)	0(< 0.1)	1.88 ± 0.18	106.5/91	
	0.01(f)	$0.32^{+0.10}_{-0.08}$	0.5(f)	0(< 0.07)	1.94 ± 0.16	107.8/91	
NGC4438	0.02(f)	$0.79^{+0.07}_{-0.15}$	0.1(f)	1.4(< 5.3)	$2.0^{+1.5}_{-1.0}$	35.0/40	
	0.02(f)	$0.76^{+0.08}_{-0.13}$	0.5(f)	0(< 0.18)	$2.0^{+0.4}_{-0.3}$	34.9/40	
NGC4450	0.018(f)	$0.65^{+0.23}_{-0.30}$	0.1(f)	0(< 0.087)	$1.74^{+0.19}_{-0.16}$	63.9/68	
	0.018(f)	$0.64^{+0.09}_{-0.32}$	0.5(f)	0(< 0.067)	$1.80^{+0.16}_{-0.13}$	64.1/68	
NGC4565	0.038(f)	$1.35^{+1.65}_{-0.42}$	0.27(> 0.03)	$2.2^{+1.1}_{-0.9}$	$2.48^{+0.36}_{-0.31}$	136.0/107	3
				$0.27^{+0.39}_{-0.11}$	(CF $0.69^{+0.10}_{-0.56}$)		
NGC4569	0.02(f)	$0.69^{+0.07}_{-0.09}$	$0.12^{+0.42}_{-0.064}$	$2.4^{+1.5}_{-1.2}$	$2.7^{+0.9}_{-0.6}$	54.6/41	
NGC4579	0.031(f)	$0.90^{+0.11}_{-0.05}$	0.5(f)	0.04 ± 0.03	1.72 ± 0.05	192.4/201	2
NGC4594	0.035(f)	$0.64^{+0.18}_{-0.15}$	$0.05^{+0.07}_{-0.02}$	$0.73^{+0.36}_{-0.33}$	1.89 ± 0.17	104.9/85	
NGC4736	0.011(f)	$0.62^{+0.06}_{-0.07}$	$0.05^{+0.11}_{-0.02}$	0(< 0.88)	$1.44^{+0.14}_{-0.16}$	100.6/104	
NGC5005	0.011(f)	$0.76^{+0.07}_{-0.08}$	$0.06^{+0.09}_{-0.02}$	0.10(< 0.86)	0.97 ± 0.37	71.3/57	
NGC5194	0.013(f)	0.63 ± 0.04	$0.033^{+0.011}_{-0.009}$	$2.4^{+1.4}_{-1.0}$	$1.57^{+0.58}_{-0.42}$	164.2/141	1
NGC5195	0.013(f)	$0.60^{+0.08}_{-0.13}$	$0.03^{+0.03}_{-0.02}$	$2.3^{+2.5}_{-1.7}$	$2.2^{+1.2}_{-0.8}$	17.4/20	
NGC7217	0.09(f)	$0.76^{+0.10}_{-0.12}$	0.1(f)	$1.5^{+1.6}_{-0.9}$	$2.4^{+0.8}_{-0.6}$	71.4/57	
NGC7217	0.09(f)	$0.74^{+0.09}_{-0.13}$	0.5(f)	$0.85^{+0.85}_{-0.60}$	$2.2^{+0.6}_{-0.4}$	71.3/57	

1: including an iron emission line at 6.4 keV., 2: including an iron emission line at 6.7 keV. 3: fitting results of the nucleus + the off center source.

Table 5.5: Results of power-law + variable abundance Raymond-Smith model fit

name	$N_{\rm H}$ [10^{22}cm^{-2}]	kT [keV]	abundance (O,Ne,Mg,Si)	abundance (Fe)	$N_{\rm H}$ [10^{22}cm^{-2}]	Γ	χ^2/dof	no
NGC3079	0.010(f)	$0.62^{+0.08}_{-0.15}$	0.5(f)	$0.048^{+0.026}_{-0.019}$	$1.8^{+1.7}_{-1.3}$	2.0 ± 0.7	91.5/90	
NGC4450	0.018(f)	$0.66^{+0.19}_{-0.30}$	0.5(f)	0.09(> 0.03)	< 0.38	$1.64^{+0.30}_{-0.39}$	62.9/68	
NGC4565	0.038(f)	$0.80^{+1.08}_{-0.38}$	0.5(f)	0.04(< 0.09)	$3.1^{+0.7}_{-0.8}$	$2.70^{+0.34}_{-0.43}$	132.6/107	3
					$0.53^{+0.18}_{-0.22}$	(CF $0.69^{+0.09}_{-0.07}$)		
NGC4579	0.031(f)	$0.89^{+0.12}_{-0.08}$	0.5(f)	0.4(> 0.12)	0.04 ± 0.03	1.72 ± 0.05	192.6/201	2
NGC4594	0.035(f)	$0.62^{+0.08}_{-0.11}$	0.5(f)	$0.11^{+0.08}_{-0.03}$	0.73 ± 0.29	1.89 ± 0.16	99.9/85	
NGC4736	0.011(f)	$0.61^{+0.06}_{-0.09}$	0.5(f)	$0.23^{+}_{-0.10}$	<0.09	$1.57^{+0.15}_{-0.12}$	100.8/104	2
NGC5005	0.011(f)	$0.76^{+0.08}_{-0.10}$	$0.11^{+0.53}_{-0.11}$	$0.078^{+0.13}_{-0.038}$	0.09(< 0.73)	$1.00^{+0.36}_{-0.38}$	71.7/56	
NGC5194	0.013(f)	$0.61^{+0.04}_{-0.05}$	$0.14^{+0.05}_{-0.06}$	$0.041^{+0.013}_{-0.011}$	$2.6^{+1.3}_{-0.7}$	$1.69^{+0.35}_{-0.48}$	152.1/140	

1: including an iron emission line at 6.4 keV, 2: including an iron emission line at 6.7 keV, 3: partial covered power-law model

Table 5.6: Summary of iron emission line parameters

name	center energy [keV]	line width [keV]
NGC1052	6.32 ± 0.08	0(f)
NGC2273	$6.37^{+0.05}_{-0.06}$	0(f)
NGC3998	$6.40^{+0.11}_{-0.20}$	0(f)
NGC4579	$6.70^{+0.13}_{-0.12}$	$0.17^{+0.11}_{-0.12}$
NGC4941	$6.31^{+0.07}_{-0.08}$	0(f)
NGC5033	$6.38^{+0.08}_{-0.06}$	0(f) (< 0.26)
NGC5194	$6.40^{+0.08}_{-0.12}$	0(< 0.27)

Table 5.7: Equivalent width of iron K emission

name	Fe-K 6.4keV EW [eV]	Fe-K 6.7keV EW [eV]	$\Delta\chi^2$ (6.4 keV)	$\Delta\chi^2$ (6.7 keV)	notes
NGC1052	180^{+80}_{-90}	< 120	12.1	0.2	5
NGC1667	—	—			
NGC3079	780< 1700	1100< 2400	1.9	1.7	
NGC3998	90^{+70}_{-70}	< 90	4.1	0	1
NGC4203	< 300	< 260	0.0	0.0	1
NGC4438	< 1300	< 3900	0.0	1.0	2
NGC4450	550(< 1200)	610(< 1400)	2.5	1.7	2
NGC4565	240(< 620)	< 350	1.7	0.1	
NGC4569	< 1800	< 4800	0.0	0.0	2
NGC4579	< 280	490^{+180}_{-190}		20.0	2
NGC4594	< 150	< 260	0	0	
NGC4736	170 ± 170	340^{+380}_{-320}	0.5	2.9	
NGC4941	760^{+410}_{-280}		15.7		4
NGC5005	380(< 1000)	< 480	0.8	0.0	2
NGC5033	290 ± 100	< 230	22.5	0.9	1
NGC5194	910^{+410}_{-380}		15.7		3
NGC5195	< 3700	< 5000	0.0	0.0	2
NGC7217	< 460	< 1100	0.0	0.0	2

1. PL model, 2. PL + RS model, 3. PL + variable RS model, 4. partial covering PL model, 5. partial covering PL + RS model

The $\Delta\chi^2$ value for the 6.4 keV line in NGC5033 — two additional parameters (line center energy and line intensity).
The $\Delta\chi^2$ value for the 6.7 keV line in NGC4579 — three additional parameters (line center energy, line width and line intensity).
others — one additional parameter (line intensity).

Table 5.8: Summary of X-ray flux in unit of 10^{-12} ergs cm^{-2} s^{-1}

name	total	power-law		Raymond-Smith	
	(observed)	(observed)	(intrinsic)	(observed)	(intrinsic)
	2–10 keV	2–10 keV	2–10 keV	0.5–4 keV	0.5–4 keV
NGC1052	4.78	4.72	9.94	0.316	0.344
NGC1667	$0.09^{+0.04}_{-0.05}$	0.09	0.09	—	—
NGC2273	1.1	1.1	6.3	—	—
NGC3079	0.46	0.43	0.51	0.45	0.47
NGC3998	8.06	8.06	8.13	—	—
NGC4203	2.1	2.1	2.1	—	—
NGC4438	$0.28^{+0.04}_{-0.05}$	0.24	0.28	0.40	0.43 (ab=0.1)
	$0.27^{+0.05}_{-0.05}$	0.26	0.26	0.19	0.20 (ab=0.5)
NGC4450	0.66	0.66	0.66	0.085	0.090(ab=0.1)
	0.65	0.65	0.65	0.056	0.059(ab=0.5)
NGC4565	1.6	1.6	2.2	0.30	0.33 (vRS fit)
NGC4569	$0.31^{+0.12}_{-0.11}$			$0.33^{+0.14}_{-0.13}$	
NGC4579	4.3	4.3	4.3	0.63	0.66 (ab=0.1)
			4.3	0.32	0.35 (ab=0.5)
NGC4594	2.8	2.7	2.9	0.69	0.78
NGC4736	2.0	2.0	2.0	0.64	0.67
NGC4941	1.3	1.3	9.7	—	—
NGC5005	0.73	0.70	0.71	0.35	0.37
NGC5194	1.1	1.0	1.0	1.1	1.1
NGC5195	0.31	0.29	0.36	0.44	0.46
NGC5033	5.5	5.5	5.6	—	—
NGC7217	0.21	0.20	0.24	0.10	0.14 (ab=0.1)
	$0.22^{+0.02}_{-0.03}$	0.21	0.23	0.072	0.095 (ab=0.5)

"ab" in the parenthesis denotes the assumed abundance of the Raymond-Smith component. Errors are quoted if statistical error dominates.

Table 5.9: Summary of X-ray luminosity in unit of 10^{40}ergs s^{-1}

name	total	power-law		Raymond-Smith	
	(observed)	(observed)	(intrinsic)	(observed)	(intrinsic)
	2–10 keV	2–10 keV	2–10 keV	0.5–4 keV	0.5–4 keV
NGC1052	18.2	17.9	37.8	1.20	1.31
NGC1667	4.0	4.0	4.0	—	—
NGC2273	11.0	11.0	60.8	—	—
NGC3079	2.3	2.2	2.5	2.2	2.3
NGC3998	45.1	45.1	45.5	—	—
NGC4203	2.34	2.34	2.34	—	—
NGC4438	0.95	0.81	0.95	1.4	1.5 (ab=0.1)
	0.91	0.88	0.88	0.64	0.68 (ab=0.5)
NGC4450	2.2	2.2	2.2	0.29	0.30 (ab=0.1)
	2.2	2.2	2.2	0.19	0.20 (ab=0.5)
NGC4565	1.81	1.81	2.48	0.34	0.37
NGC4565(nucleus)	0.59	0.59	—	—	—
NGC4569	1.1			1.1	
NGC4579	15	15	15	2.1	2.2 (ab=0.1)
				1.1	1.2 (ab=0.5)
NGC4594	13	13	14	3.3	3.7
NGC4736	0.45	0.44	0.44	0.14	0.15
NGC4941	0.64	0.64	4.8	—	—
NGC5005	4.0	3.8	3.9	1.9	2.0
NGC5033	23.2	23.2	23.4	—	—
NGC5194	0.75	0.73	0.73	0.75	0.80
NGC5195	0.32	0.30	0.37	0.46	0.48
NGC7217	0.66	0.63	0.74	0.32	0.42 (ab=0.1)
	0.67	0.66	0.72	0.22	0.29 (ab=0.5)

5.2 Images

X-ray image is made and examined whether X-ray emission is point-like or not. We made X-ray images in some energy range using SIS data and compare them it with the point spread function of XRT+SIS. Since SIS has superior spatial resolution than GIS, we use SIS images for this purpose.

Except for some cases, we made an azimuthally averaged profile of surface brightness and compared with the point spread function + the background. The point spread function at the source position is simulated using the ray-tracing code. The background is assumed to be constant. Although the background level depends on the position on the detector, we checked that constant assumption is accurate enough for our purpose by using the surface brightness profiles of the blank skies.

In some observations, there is an X-ray source near (<4') the target source (for example, NGC 4203, NGC4565, and NGC5194/95). In these cases we utilize the projected profiles to an appropriate direction to evaluate spatial extension in stead of radial profiles. These results are discussed in subsections on individual objects.

Obtained reduced chi-square values are summarized in Table 5.10. Only NGC 5005 is extended even at 4–10 keV band. The X-ray images of other objects are consistent with point-like in the hard energy band.

Table 5.10: Reduced chi-square values for the PSF + background fit to the radial profiles of surface brightness obtained with SIS0 + SIS1. The degree of freedom is 11.

name	0.5–2 keV	2–10 keV	4–10 keV
NGC 1052	1.30	0.88	
NGC 3079	2.93	2.11	0.820
NGC 3998	0.518	0.546	
NGC 4450	1.97	1.23	
NGC 4569	1.93	1.12	
NGC 4594	1.99	0.755	
NGC 4736	0.924	1.47	0.880
NGC 5005	1.42	1.61	1.42
NGC 5033	0.69	0.40	

5.3 Variability

X-ray light curves are made using the same extraction region as making spectra, and examined time variability. The X-ray flux of most of the observed objects are small, we binned the light curves with 5760 sec bin, which is an one orbit period of the *ASCA* satellite.

The light curves are made in several energy band. As the hard component is a dominant component above 2 keV in most of the objects, we made a 2–10 keV light curve for all of the four detectors, otherwise noted. Then we combined these light curves together, and fitted with a constant. We also examined a light curve in all energy range: 0.5–10 keV for SIS and 0.7–10 keV for GIS. Although the soft thermal component are often present, the hard component may be also significantly contribute to the soft energy band. In this case we can expect better S/N light curves compared to 2–10 keV light curves.

5.4 Low luminosity Seyfert 1 Galaxies

5.4.1 Introduction

Recent optical spectroscopic surveys have shown that there are many active galactic nuclei (AGNs) in nearby galaxies and about 1/3 of bright galaxies are classified as Seyfert galaxies or LINERs (Low Ionization Nuclear Emission-line Regions; Heckman 1980) (Ho, Filippenko, & Sargent 1997a). The luminosity of these objects are rather low compared to previously known AGN with a median value of the Hα luminosity being only 2×10^{39} ergs s^{-1} in the sample of Ho et al (1997a). Such objects (LLAGNs) are important for investigating the physics of AGN under an extreme condition, i.e. very low luminosity. X-ray observations probe the innermost regions in AGNs and specifically the iron K line provides information on the ionization state, density, motion of matter very close to the central energy source.

ASCA observations of Seyfert 1 galaxies revealed that as a class these objects have a broad iron K line with a profile skewed to lower energies, which thought to be caused by the reprocessing of the continuum by a relativistic accretion disk (e.g., Tanaka et al. 1995, Nandra et al. 1997a). The center energy of the iron line from Seyfert 1 galaxies is consistent with 6.4 keV, which is expected from fluorescence by neutral or lower ionization states of (<FeXVI) iron in a disk with a inclination of < 30 degrees. In some Seyfert 2 galaxies (e.g. IRAS 18325–5926) a higher peak energy of iron emission is seen, which is compatible with a highly inclined disk ($i = 40 - 50°$) origin (Iwasawa et al. 1996). Highly

ionized iron emission lines are detected from several radio-quiet quasars e.g. E1821+643 (Kii et al. 1992, Yamashita et al. 1997) and PG 1116+215 (Nandra et al. 1996). Nandra et al. (1997b) studied the luminosity dependence of the iron line profile in a large sample of AGN and found that the center energy increases and the red-tail becomes weaker with increasing luminosity. They attributed such behavior to an increasing ionization of the accretion disk with increasing luminosity. Thus X-ray measurements of iron emission lines are powerful diagnostic tools of matter in the vicinity of the nucleus.

There are only a few observations of iron emission lines from low luminosity AGNs ($L_{\rm X}$ (2–10 keV) $\sim 10^{40} - 10^{41}$ ergs s^{-1}). M81 (NGC 3031) with X-ray luminosity of $L_{\rm X}$ (2–10 keV) $\sim 2 \times 10^{40}$ ergs s^{-1} shows a broad iron line centered at ~ 6.7 keV with an equivalent width of ~ 200 eV. This line center energy is significantly higher than Seyfert 1 galaxies and similar to luminous quasars. On the other hand, only an upper limit on the equivalent width 300 eV is obtained for NGC 1097 ($L_{\rm X}$ (2–10 keV) $= 1 \times 10^{41}$ ergs s^{-1}, Iyomoto et al. 1996). Although strong iron emission lines are also detected from M51 (NGC 5194, Terashima et al. 1998a), NGC 1365 and NGC 1386 (Iyomoto et al. 1997), the iron lines in these objects are interpreted as being caused by reprocessed emission from an obscuring tori and/or extended ionized scatterer outside of our line of sight, because these nuclei are heavily obscured. Thus, at present, the number of low luminosity AGNs with small intrinsic absorption from which iron lines are detected is rather limited.

In this section, we report the detection of iron K emission lines from low luminosity Seyfert 1 galaxies NGC 4579 and NGC 5033 and discuss X-ray properties of the low luminosity AGN and origin of the iron emission line.

5.4.2 NGC 4579

Results

X-ray image

NGC 4579 is detected at the position of the optical nucleus within position determination uncertainties and the X-ray image looks point-like. We compared X-ray images in the 0.5–2 keV and 2–10 keV band with the point spread function (PSF) of *ASCA* XRT + SIS to evaluate the spatial extension. We fit the azimuthally averaged surface brightness profiles with those of a model PSF + constant background, where we left two parameters free; the normalization of PSF and the background level. We obtained good fits with reduced chi-square $\chi^2_\nu = 0.64$ and 0.70 (11 dof) for the soft and hard energy bands, respectively. Thus the images in these energy bands are consistent with a point source. In order to set an upper limit of the spatial extent, we fit the radial brightness profiles with

those of a two-dimensional Gaussian convolved through the PSF. In this fitting, the free parameters are a Gaussian sigma, normalization of the Gaussian, and background level. The upper limits of the Gaussian width are 0.25 arcmin for both soft and hard band (0.25 arcmin corresponds to 1.2 kpc at 16.8 Mpc).

The fitted background level is ~ 2.5 times higher than that of blank sky observations released by NASA Guest Observer Facility in the 0.5–2 keV band, while 2–10 keV background is consistent with the blank sky fields. NGC 4579 is located at $\sim 1.8°$ away from M87 in the Virgo cluster of galaxies and soft diffuse emission due to the intracluster gas is present in this region (Böhringer et al. 1994). Thus the high background level in the soft band is most likely due to Virgo cluster emission. In the soft band image, no significant structure is seen.

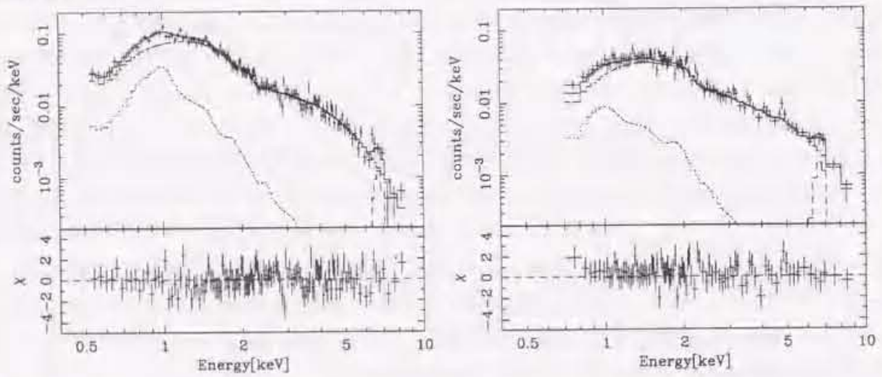

Figure 5.2: X-ray spectra of NGC 4579; left: SIS, right: GIS.The best fit model consist of a Raymond-Smith thermal plasma, power-law, and Gaussian is shown as histograms.

X-ray spectrum

X-ray spectra obtained with the SIS and GIS are shown in Fig. 1. The X-ray spectra cannot be fitted with simple power-law or thermal bremsstrahlung model and residuals were clearly seen around 1 keV and 6.5 keV, which can be identified respectively with iron L line complex and an iron K emission line. An acceptable fit is obtained with the sum of a power-law, a Raymond-Smith (R-S) thermal plasma model (Raymond & Smith 1977) and a Gaussian at 6.7 keV. In the fitting, the absorption column density is assumed to be the Galactic value (3.1×10^{20} cm^{-2}; Murphy et al. 1996) for the R-S component and left free for the power-law component. The best fit parameters of the X-ray continuum are summarized in Table 1 and the best fit model are also shown in Fig. 1 as a histogram. The photon index of the power-law component is 1.72 ± 0.05 (hereafter

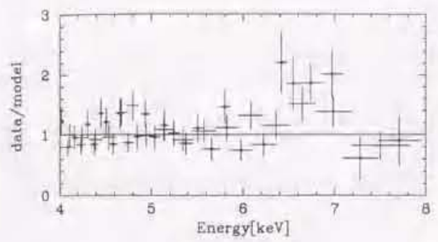

Figure 5.3: Data/model ratio for the best fit continuum model around an iron K emission line in NGC 4579. The crosses with and without filled circle represent SIS and GIS data, respectively.

quoted errors are 90% confidence for one interesting parameter), and the X-ray luminosity of this component is 1.5×10^{41} ergs s^{-1} in the 2–10 keV band. Although a small excess absorption $N_{\rm H} = 4 \pm 3 \times 10^{20}$ cm^{-2} is necessary to fit the data in addition to the Galactic absorption, $N_{\rm H}$ is still consistent with the Galactic value if the calibration uncertainties of SIS at low energies are taken into account. Since the power-law component dominates the X-ray flux even in the soft energy band, the abundance of the metals in the R-S component is poorly constrained. Therefore we fixed the abundance at 0.5 solar. Then the soft component is represented by the R-S model with $kT = 0.90^{+0.11}_{-0.05}$. and $L_{\rm X}$(RS) of 1.2×10^{40} ergs s^{-1} in the 0.5–4 keV band. The X-ray luminosity of the R-S component depends on the assumed abundance value, and 0.88×10^{40} and 1.7×10^{40} ergs s^{-1} are obtained for assumed abundances 1.0 and 0.1 solar, respectively. This decomposition of the spectrum is very similar to that of many other low luminosity objects observed by *ASCA* (Serlemitsos, Ptak and Yaqoob 1996). The hard band spectrum can be also be well represented by a Raymond-Smith thermal plasma with $kT = 7.9^{+1.3}_{-0.9}$ keV and abundance of $0.55^{+0.18}_{-0.16}$ in stead of a power-law plus Gaussian.

An iron K line is clearly detected in the X-ray spectra and an addition of a Gaussian line improved χ^2 by 20.0 for three additional parameters (line center energy, line width, and normalization). Therefore an iron line is statistically significant at more than 99.9 % confidence according to the F-test. The line center energy is $6.73^{+0.13}_{-0.12}$ keV (rest frame), which is higher than the 6.4 keV typically observed from Seyfert 1 galaxies. The equivalent width is 490^{+180}_{-190} eV. The iron line profile is shown in Figure 2 as the ratio of the data

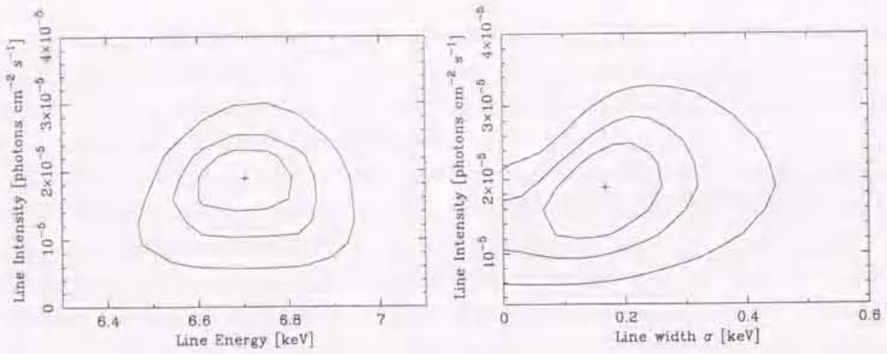

Figure 5.4: left: Confidence contours for the line energy and intensity. The line width is left to be vary. right: Confidence contours for the line width (Gaussian σ) and intensity. The contours correspond to 68%, 90%, and 99% confidence level for two interesting parameters ($\Delta\chi^2$ = 2.3, 4.6, and 9.2, respectively).

to the best fit continuum component of the above fitting. Figure 3 shows the confidence contours for the line energy and intensity. The best fit energy agrees with He-like iron and the 90% confidence range corresponds to the ionization state from FeXX to FeXXV (He-like). The line center energy of 6.4 keV, which is expected from cold or low ionized iron, is excluded at more than 99% confidence level. The confidence contours for the line width σ and intensity are shown in Figure 4. The emission line is marginally broad. Although the best fit width is σ = 170 eV, a narrow line cannot be excluded at 90% confidence level for 2 interesting parameters. If we fix the line width at σ=0, the line center energy of $6.82^{+0.10}_{-0.26}$ keV and equivalent width of 360^{+175}_{-135} eV are obtained.

A combination of multiple narrow lines instead of a single broad Gaussian also provides a good fit (χ^2_ν=0.958 for 201 dof), where the line center energies are fixed at 6.4 keV, 6.7 keV, and 7.0 keV, which represent cold, He-like, and H-like iron, respectively. The obtained equivalent widths are 110^{+130}_{-110}, 240^{+170}_{-160}, and 160^{+190}_{-160} eV, respectively (Table 2). The 6.7 keV line is the dominant component also in this model.

Many Seyfert 1 galaxies show broad iron lines with a significant red tail and they are interpreted as originating from inner part of a relativistic accretion disk (e.g. Tanaka et al. 1995). We examined the disk-line model by Fabian et al. (1989) instead of the Gaussian model. Since statistics are limited, only two parameters, the inclination angle of the disk and normalization, were left free. The inclination angle is defined such that i = 0 corresponds to a face-on disk. The line emissivity is assumed to be proportional

Table 5.11: Results of spectral fitting to the SIS and GIS spectra of NGC4579

model	$N_{\rm H}$(galactic) [10^{20} cm^{-2}]	kT [keV]	abundance [solar]	$N_{\rm H}$ [10^{20} cm^{-2}]	Γ or kT [keV]	abundance —	χ^2/dof
(1)	3.1(f)	$0.90^{+0.11}_{-0.05}$	0.50(f)	4.1 ± 2.7	1.72 ± 0.05		192.4/201
(2)	3.1(f)	$0.88^{+0.11}_{-0.05}$	0.50(f)	0(f)	$7.9^{+1.3}_{-0.9}$	$0.55^{+0.18}_{-0.16}$	198.2/204

The fitting models are (1)Raymond-Smith + Power-law and (2)Raymond-Smith + Raymond-Smith. (f) in the table denotes frozen parameter. The quoted errors in parenthesis are at the 90% confidence level for one interesting parameter.

Table 5.12: Gaussian fits to the iron K line

model	E_L [keV]	σ [keV]	EW [eV]	χ^2/dof
narrow Gaussian	$6.82^{+0.10}_{-0.26}$	0(f)	360^{+175}_{-135}	195.5/202
broad Gaussian	$6.73^{+0.13}_{-0.12}$	$0.17^{+0.11}_{-0.12}$	490^{+180}_{-190}	192.4/201
three narrow Gaussians	6.4(f)	0(f)	110^{+130}_{-110}	192.6/201
	6.7(f)	0(f)	240^{+170}_{-160}	
	7.0(f)	0(f)	160^{+190}_{-160}	

to r^{-q} and q is fixed at 2.5, which is the typical value for Seyfert 1 galaxies (Nandra et al. 1997a). The line center energy is fixed at 6.4 keV or 6.7 keV. The inner radius of the line emitting region is fixed at $6r_g$, where $r_g = GM/c^2$ is the gravitational radius. The outer radius is fixed at χ^2 local minima in the fitting $16.6r_g$ and $10.5r_g$ for 6.4 keV and 6.7 keV case, respectively. The disk-line model fits provided worse reduced chi-square values $\Delta\chi^2 \sim 8$ than the Gaussian modeling. The best fit parameters are summarize in Table 3. Although the fit is acceptable, systematic positive residuals are seen around 6.7 keV. This is probably due to absence of significant red asymmetry in the observed profile. The obtained equivalent width $\sim$ 900 eV is extremely large compared to the value expected from a X-ray irradiated disk (e.g. George & Fabian 1991) and observed in Seyfert 1 galaxies (Nandra et al. 1997a).

Table 5.13: Disk-line model fits to the iron K line

E_L [keV]	R_{in} [R_g]	R_{out} [R_g]	i degree	EW [eV]	χ^2/dof
6.4(f)	6(f)	16.6(f)	42 ± 4	880^{+570}_{-360}	200.7/202
6.7(f)	6(f)	10.5(f)	36 ± 3	920^{+530}_{-320}	201.5/202

Discussion

X-ray emission from a low luminosity AGN

We obtained X-ray images and spectra in the 0.5–10 keV band and a point-like X-ray source with a photon index of $\Gamma = 1.72 \pm 0.05$ is detected. An iron line is also detected at 6.7 keV. In the soft energy band, a broad line like feature identified with iron-L line complex indicates the presence of thin-thermal plasmas of temperature $kT \sim 0.9$ keV.

The X-ray luminosity (1.5×10^{41} ergs s^{-1} in 2–10 keV) is 1–3 orders of magnitude smaller than typical Seyfert galaxies and falls in the classes of LINERs and "low luminosity" Seyfert galaxies (Serlemitsos et al. 1996, Iyomoto et al. 1996, Ishisaki et al. 1996). In normal spiral galaxies, the X-ray emission is dominated by discrete sources specifically low mass X-ray binaries (LMXBs) (e.g. Fabbiano 1989, Makishima et al. 1989). The X-ray luminosity from LMXBs are roughly proportional to B-band luminosity L_B and their X-ray spectra can be approximated by a thermal bremsstrahlung of a temperature of several keV. The *ASCA* X-ray spectra of NGC 4579 well fitted by $kT \sim 8$ keV thermal plasma model. However the strong iron line at 6.7 keV is not compatible with the X-ray spectra of LMXBs, since equivalent width of iron emission lines from LMXBs are small (several tens of eV, Hirano et al. 1989). Additionally, the L_X/L_B value 1.3×10^{-3} is more than an order of magnitude higher than normal spiral galaxies (e.g. L_X/L_B=3.5×10^{-5} for M31; Makishima et al. 1989). Therefore we conclude that AGN emission dominates the *ASCA* spectra and that contribution from LMXBs to X-ray emission of NGC 4579 is negligible.

If the primary ionizing mechanism of LINER optical emission lines in this galaxy is photoionization by a low luminosity AGN, $L_X/L_{H\alpha}$ might be expected to be similar to Seyfert 1 galaxies, for which there is a good positive correlation between L_X and $L_{H\alpha}$ (e.g. Ward et al. 1988, Koratkar et al. 1995, Serlemitsos et al. 1996). Using the Hα luminosity of broad plus narrow component $L_{H\alpha} = 5.9 \times 10^{39}$ ergs s^{-1} (Ho et al. 1997b)

and the observed X-ray luminosity in the 2–10 keV band, we obtain $L_X/L_{H\alpha} \approx 26$ for NGC 4579. This value is in excellent agreement with those of Seyfert 1 galaxies (Ward et al. 1988) and strongly supports a low luminosity AGN as the ionizing source of the LINER in NGC 4579.

Less luminous Seyfert 1 galaxies tend to show rapid and large amplitude variability (Mushotzky, Done and Pounds 1993 and references therein). However NGC 4579 shows no significant short term variability. Lack of variability on short time scales seems to be a common property of low luminosity AGNs (Mushotzky 1993, Petre et al 1993),for example the low luminosity AGN in NGC 1097 (Iyomoto et al. 1996) and NGC 3998 (Awaki et al. 1992) also show no significant variability on time scales less than a day.

The X-ray spectral slope $\Gamma = 1.72 \pm 0.05$ is identical to the average value found for Seyfert 1 galaxies (Mushotzky, Done and Pounds 1993) but the luminosity is lower than that of any Seyfert 1 galaxy but NGC 4051. Based on the FW0I (full width at 0 intensity) of a broad emission line and an estimate of the size of the broad line region, mass of the central black hole is $M_\bullet \sim 4 \times 10^6 M_\odot$. Then the Eddington ratio L/L_{Edd} is $\sim 10^{-3}$ for the observed luminosity of $\sim 5 \times 10^{41}$ ergs s^{-1} (Barth et al. 1996 a). Therefore X-ray spectral slope does not seem to be drastically changed even as a very low Eddington ratio. This is also true for M81, for which L/L_{Edd} is estimated to be $\sim (2-10) \times 10^{-4}$ (Ho, Filippenko, & Sargent 1996) and the photon index is 1.85 ± 0.04 (Ishisaki et al. 1996).

Soft thermal emission of $kT \sim 0.5 - 1$ keV is often observed from low luminosity AGNs (Ptak 1997). In some cases, such emission is associated with starburst activity (e.g. Iyomoto et al. 1996, Terashima et al. 1998a). The far infrared luminosity of NGC 4579 is 1.5×10^{43} ergs s^{-1} and some star formation activity may be present and may explain the thermal emission. The X-ray to far infrared luminosity ratio $L_X/L_{FIR} = 6 \times 10^{-4} - 1.1 \times 10^{-3}$ is consistent with starburst galaxies (e.g. David, Jones, & Forman 1992) within scatter.

iron-K line

A marginally broad ($\sigma \approx 0.17$ keV) iron emission line is clearly detected at $6.73^{+0.13}_{-0.12}$ keV and the equivalent width is 490^{+180}_{-190} eV for the broad Gaussian model fit. The line center energy is significantly higher than 6.4 keV, which is typically observed from Seyfert 1 galaxies, and consistent with He-like iron. Similar broad iron line centered at ~ 6.7 keV is detected from the low luminosity Seyfert galaxy M81 (Ishisaki et al. 1996, Serlemitsos et al. 1996). The line can also be represented by line blending of neutral, He-like, and H-like iron and dominated by He-like iron. The disk-line profile (Fabian et al. 1989) is

not inconsistent with the data for 6.4 keV or 6.7 keV intrinsic line energy. However the chi-square value is worse than a single broad Gaussian fit and systematic residuals remain in the disk-line fit, since a significant red tail is not clearly seen in the data. Another problem of the disk-line model is the very large equivalent width $\sim$ 900 eV, which is about 4 times larger than the results of the disk-line fit to Seyfert 1 galaxies (<EW>= 230 ± 60 eV, Nandra et al. 1997a). Therefore our data prefer a symmetric Gaussian-shape profile with intrinsic line center energy of 6.7 keV (He-like) and/or 7.0 keV (H-like) rather than 6.4 keV (<Fe XVI). Thus the ionization state of the iron line emitter may be different from that of higher luminosity Seyfert 1 galaxies in at least some low luminosity AGNs (NGC 4579 and M81)

Strong ionized iron emission lines are observed in heavily obscured Seyfert 2 galaxies (NGC 1068, Ueno et al. 1994, Iwasawa, Fabian, & Matt 1997; NGC 1365, Iyomoto et al. 1997; see also Turner et al. 1997a, b). In these objects continuum emission from the nucleus is completely blocked and only scattered radiation is observed. Ionized iron lines are interpreted to be originated from a photoionized scattering medium. If the continuum of NGC 4579 is scattered radiation, the observed X-ray luminosity is only a fraction of its intrinsic luminosity. Since the scattering fraction is typically less than 10 % for Seyfert 2 galaxies (Ueno 1995), the $L_{\rm X}/L_{\rm [OIII]}$ should be less than 10 % of those of Seyfert 1 galaxies as is the case for NGC 1068 (Mulchaey et al. 1992). However observed X-ray to [OIII]λ5007 luminosity ratio $L_{\rm X}/L_{\rm [OIII]}$ is very similar to Seyfert 1 galaxies. Therefore the observed X-ray continuum is not likely to be due to scattered component but a direct continuum from the active nucleus. Then the observed iron line should be emitted from the matter close to the nucleus in order to be ionized and/or broadened due to the Doppler effect.

If the iron line is emitted by the accretion disk, a line profile with significant red tail is expected (Fabian et al. 1989). On the other hand, the observed profile seems to be symmetric in shape although the statistics are limited. Broad lines with weaker red tail than Seyfert 1s are observed in AGNs with much higher luminosity; $L_{\rm X} > 10^{44}$ ergs s^{-1} (Nandra et al. 1997b). If the innermost part of the accretion disk is almost fully ionized, the red component is expected to be very weak or absent consistent with the interpretation that the observed iron K emission is from an ionized disk.

The obtained equivalent width ($\sim$ 500 eV for the Gaussian model) is rather large compared to that seen in most Seyfert 1 galaxies. If the disk is highly ionized, the fluorescence yield of iron increases and absorption by lighter elements decreases as light elements are almost completely ionized. In such a situation the equivalent width of an iron line can increase by a factor of two (Matt et al. 1993, Życki & Czerny 1994). Therefore

the large equivalent width is also naturally explained by an ionization effect.

The ionization state of photoionized matter is determined by an ionization parameter $\xi = L/nR^2$ (Kallman & McCray 1982), where L, n, and R is luminosity of ionizing photons, number density of photoionized matter, distance from light source to photoionized matter, respectively. The X-ray luminosity of NGC 4579 is only 1.5×10^{41} ergs s^{-1}, which is 1-3 orders of magnitude smaller than usual Seyfert 1 galaxies, and the X-ray luminosity of M81, from which an iron line centered at $\sim$ 6.7 keV is detected, is even lower ($\sim 2 \times 10^{40}$ ergs s^{-1}). In order to photoionize iron atoms to He-like, ξ should be at least $\sim$ 500, while $\xi < 100$ is required for less ionized species (< Fe XVI) which is probably appropriate for usual Seyfert 1 galaxies. Therefore nR^2 in the iron line emitting region should be more than 2.5 orders of magnitude smaller than that of luminous Seyfert 1 galaxies. An expected ionization parameter under an assumption of standard α disk is calculated by Matt et al. (1993). According to their results, the ionization parameter has a strong dependence on the mass accretion rate $\xi \propto \dot{m}^3$ (equations (5) and (6) in Matt et al. 1993), where $\dot{m}$ is denoted in units of the critical accretion rate $\dot{m} = L/L_{\rm Edd}$. In order to ionize iron to He-like, $\dot{m}$ should be at least 0.2 (Figs. 2 and 5 in Matt et al. 1993). However the order-of-magnitude estimate of the central black hole mass by Barth et al. (1996a) combined with the observed luminosity gives a significantly smaller value of $\dot{m}$ $\sim 1 \times 10^{-3}$. Then we cannot explain the very low luminosity and the ionized iron line at the same time in the standard disk model. This may suggest that the accretion processes in AGN is different in a very low luminosity situations with very small $\dot{m}$.

An advection dominated accretion flow (ADAF) model is proposed for AGNs specifically for objects radiating at very low Eddington ratio (e.g. $\dot{m} \sim 10^{-4}$ for NGC 4258, Lasota et al. 1996). In the model by Lasota et al. (1996), a standard disk is assumed outside of $r_{\rm in}$ and an ADAF inside of $r_{\rm in}$. In an ADAF, accreting matter is heated up to very high temperature ($T_i \sim 10^{12}$K, $T_e \sim 10^9$K). However our detection of an iron line indicates the presence of highly ionized (but not fully ionized) matter surrounding a large solid angle viewed from the light source. This means that $r_{\rm in}$ should be small and a geometrically thin disk is appropriate. Therefore iron line in NGC 4579 cannot be explained solely by an ADAF model and the real situation in NGC 4579 may correspond to a condition near the transition from the α disk to an ADAF.

Future sophisticated modeling of accretion in low luminosity AGNs and calculation of expected iron emission as well as precise measurements of an iron K line and mass determination by *HST* Space Telescope Imaging Spectrograph will be important to understand physical processes in extremely low luminosity AGNs.

5.4.3 NGC 5033

Results

X-ray images look like point like in both soft and hard energy band. Azimuthally averaged profiles of surface brightness is well fitted with the PSF of *ASCA* XRT + SIS in the 0.5–2 keV and 2–10 keV band. X-ray light curves in the 0.5–2 keV and 2–10 keV band are shown in Fig 5.5. Intensity variation of 30% in time scale of $\sim 10^4$ sec is clearly seen.

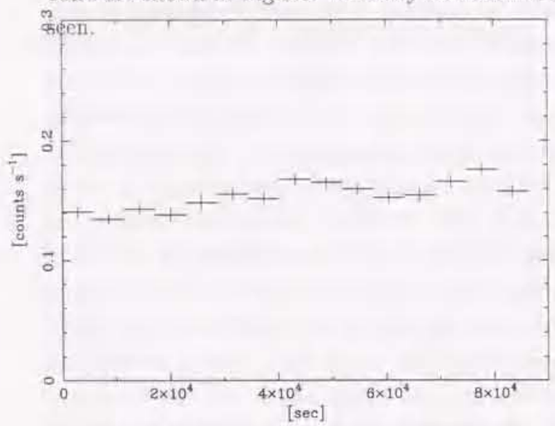

Figure 5.5: X-ray light curve of NGC 5033. SIS (0.5–10 keV) and GIS (0.7–10 keV) data are summed. Bin size = 5760 sec.

X-ray spectra of most of objects in our sample consist of at least two component, a soft thermal and hard component. On the other hand, Gaussianin NGC 5033, there is no indication of the presence of low energy emission lines from thermal plasmas, and X-ray continuum is well represented by a single component. An emission line like feature is seen around 6.4 keV. Therefore we fitted the overall spectra with a continuum plus Gaussian model.

A power-law plus Gaussian model well represent the observed spectra and the best fit parameters are summarized in Table 5.1. The observed spectra are shown in Fig 5.6 together with the best fit model. The best fit photon index is 1.72±0.04 and the absorption column density ($N_{\rm H}$ =8.7 ± 1.7 cm^{-2}) is slightly higher than the Galactic value 1.1 × 10^{20} cm^{-2}. The X-ray flux in the 2–10 keV band is 5.5 × 10^{-12} ergs s^{-1}cm^{-2} which corresponds to 2.3 × 10^{41} ergs s^{-1}.

An addition of a narrow Gaussian model improved chi-square value $\Delta\chi^2 = 22.5$ for two additional parameters (line center energy and intensity) compared to a simple power-law fit. According to F-test, this component is statistically significant at 99.999% confidence.

The best fit line center energy and equivalent width are $6.38^{+0.08}_{-0.06}$ keV and 290 ± 100 eV, respectively. If line width is allowed to be vary, chi-square value improves by only $\Delta\chi^2 = 0.1$ and the best fit line center, width, and equivalent width are $6.41^{+0.14}_{-0.09}$ keV, 100^{+160}_{-100} eV, 320^{+110}_{-140} eV, respectively. Thus the line width is consistent with a narrow line. The spectrum around iron K emission is shown in Fig 5.8 as ratios of the data to the best fit continuum model. Confidence contours for the line energy and intensity and for the line width and intensity are shown in Fig 5.7. In the iron line profile, there is a hint of a wing to higher energy side. We tried an additional narrow Gaussian at 6.7 keV. However chi-square improves only $\Delta\chi^2 = 0.9$ and equivalent width is obtained to be 40^{+190}_{-40} eV.

Many Seyfert 1 galaxies show an iron line profile skewed to red which is interpreted to be originated from inner most part of the accretion disk (disk line; Fabian et al. 1989). We examined the disk line model. Since photon statistics are limited, we fixed the line center energy at 6.4 keV and the inner radius of the line emitting region at $6r_g$, where $r_g = GM/c^2$ is the gravitational radius. The line emissivity is assumed to be proportional to r^{-q} and q is fixed at 2.5, which is typical value for Seyfert 1 galaxies (Nandra et al. 1997b).

In this model fitting, the outer radius of the line emitting region becomes greater than $1000r_g$ indicating that the iron line is emitted from an outer region in which relativistic effect is not significant and that line width is narrow. This is consistent with the Gaussian fit result which gives narrow line width. Additionally observed line profile show no significant red tail, although statistics may be too poor to recognize such a feature. We tentatively fixed the outer radius at $1000r_g$ and obtained slightly worse ($\Delta\chi^2$=+6) compared to the Gaussian model but acceptable fit was obtained. The fitting results are summarized in Table 5.14.

A thermal bremsstrahlung plus Gaussian model fit provided worse χ^2 ($\Delta\chi^2$=25.5) than power-law plus Gaussian fit and systematic negative and positive residuals are seen below 0.7 keV and above 7 keV, respectively. Furthermore the best fit center energy of the Gaussian component 6.38 keV indicate an emission line is fluorescence origin from neutral or low ionized (<FeXVI) iron and inconsistent with thermal origin. Therefore we conclude that thermal model is not appropriate for the NGC 5033 spectrum.

Discussion

X-ray variability of time scale of $\sim 10^4$ sec is detected in one day observation of NGC 5033. Less luminous Seyfert 1 galaxies tend to show large amplitude and rapid variability compared to luminous Seyfert 1 and quasars. However observed variability amplitude of NGC 5033 is only ∼30%. If other hard X-ray emitting components such as X-ray binaries

Table 5.14: Disk line model fits to the iron K line

E_L [keV]	R_{in} [R_g]	R_{out} [R_g]	i degree	EW [eV]	χ^2/dof
6.4(f)	6(f)	1000(f)	37^{+13}_{-11}	490^{+220}_{-210}	179.4/188

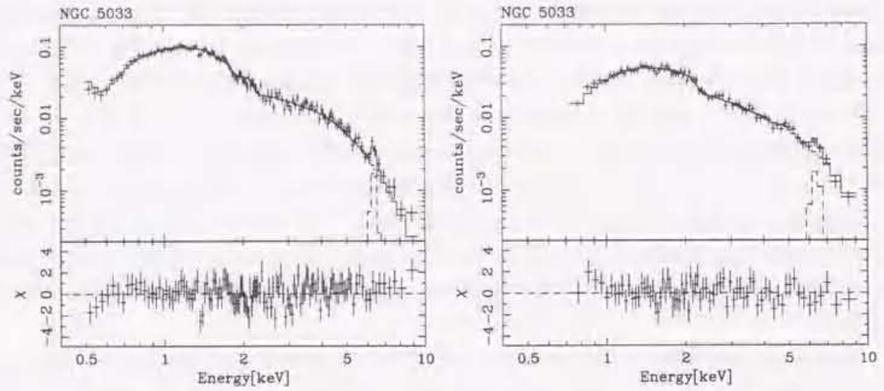

Figure 5.6: X-ray spectra of NGC 5033. left: SIS, right: GIS

and starburst activity contribute to the X-ray flux significantly, the AGN component is diluted and smaller amplitude of the variability than intrinsic amplitude is observed. However this possibility is unlikely, since $L_X/L_{H\alpha}$ is quite similar to AGNs and large L_X/L_B suggest that emission from X-ray binaries does not contribute to X-ray flux significantly. Therefore observed small amplitude seems to be real and the negative correlation between amplitude and luminosity is not seen at a luminosity around $\sim 10^{41}$ ergs s^{-1} any longer. The low luminosity Seyfert / LINER NGC 3031 (M81) ($L_X \sim 3 \times 10^{39}$ ergs s^{-1}) show also small amplitude variability (Ishisaki et al. 1996). Note that the low luminosity Seyfert NGC 4051 is a narrow line Seyfert 1 galaxies, which is a subclass of Seyfert galaxies and known to show rapid variability as a class.

The X-ray spectrum is well represented by combination of a power-law continuum and a Gaussian line. The continuum shape is very similar to Seyfert 1 galaxies with higher luminosities as is the case for NGC 4579. An iron emission line is detected at 6.4 keV which is consistent with fluoresce origin (Makishima 1986.) The 6.4 keV iron emission is generally observed from Seyfert 1 galaxies and the line width is often observed to be broad and skewed to lower energies (e.g. Nandra et al. 1997b). The iron emission from Seyfert

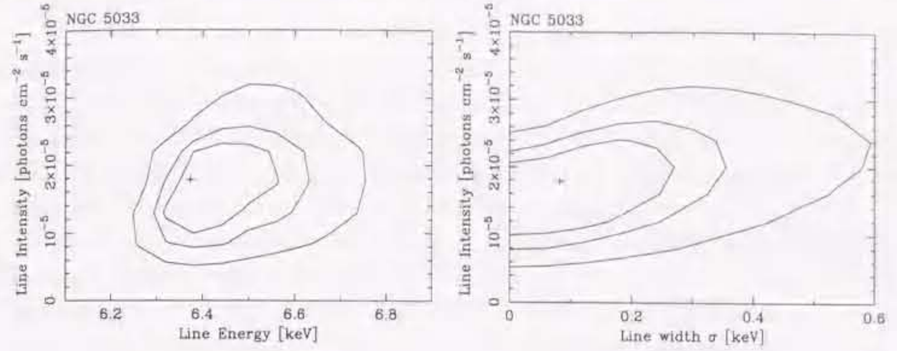

Figure 5.7: left: Confidence contours for the line energy and intensity. The line width is left to be vary. right: Confidence contours for the line width and intensity. The contours correspond to 68%, 90%, and 99% confidence level for two interesting parameters ($\Delta\chi^2$ = 2.3, 4.6, and 9.2, respectively).

1 galaxies are interpreted to be originated from the innermost part of the accretion disk (e.g. Tanaka et al. 1995).

The iron emission in NGC 5033 is consistent with narrow line width and no clear signature of broad red tail observed in Seyfert 1 galaxies is seen. Moreover the best fit equivalent width 290 $\pm$ 100 eV is larger than the equivalent width of the narrow core of the iron lines in Seyfert 1 galaxies 100–150 eV. These results would suggests that the narrow iron line contribution from putative molecular torus in the unified scheme. The iron line profiles of Seyfert 1 galaxies are well fitted with the 'disk-line' model by (Fabian et al. 1989) and no additional narrow component from the torus is not required except for small number of objects (Nandra et al. 1997b). Then the torus would be absent or subtends small solid angle viewed from the nucleus. On the other hand, the iron line in NGC 5033 is explained if the disk-line and narrow line from the torus contribute to the equivalent width of 100–150 eV each. The optical emission line spectrum is classified as intermediate type (Seyfert 1.5). This is also consistent with the orientation dependent unified model.

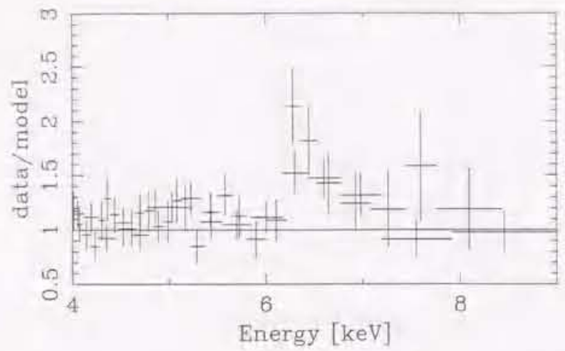

Figure 5.8: Data/model around iron K emission in NGC 5033.

5.5 Low luminosity Seyfert 2 Galaxies

5.5.1 Introduction

In Seyfert 2 galaxies, the central engine same as Seyfert 1s, i.e. accretion onto a super massive blackhole, is thought to be present. Actually X-ray observations with *Ginga* and *ASCA* detected a hard X-ray source suffered from large absorption (e.g. Awaki et al. 1990, Awaki et al. 1991).

The recent optical spectroscopic surveys of bright galaxies revealed many galaxies have ' dwarf' Seyfert nuclei (more than 10% of bright galaxies; Ho et al. 1997a, c). Low luminosity Seyfert 1 galaxies exhibit some difference compared to higher luminosity ones as discussed in the previous section; for example longer X-ray variability time scales and variety of iron K emission lines. X-ray observations of low luminosity Seyfert 2 galaxies have been done for very limited number of objects so far, because of apparent weakness due to heavy obscuration and limited sensitivity and/or energy band. Are they similar to higher luminosity Seyfert 2s? X-ray measurements of Seyfert 2 galaxies provide information on ionizing source, distribution of surrounding matter and we can compare them with higher luminosity Seyfert 2s.

One important aspect of observations of low luminosity Seyfert 2s is to clarify how many obscured AGNs there are and how much they contribute to the X-ray background. The X-ray spectrum of the Cosmic X-ray background is harder than type 1 AGNs, and X-ray sources with hard spectrum is required to explain the X-ray background by superposition of faint X-ray sources. Seyfert 2 galaxies are s candidate of such a class of

objects (Awaki 1991, Comastri et al. 1995). *ROSAT* X-ray surveys revealed the number of narrow emission line galaxies increase at low flux level (F_X(0.5-2 keV)$< 10^{-14}$ ergs $s^{-1}cm^{-2}$) and there X-ray spectra are hard (Almaini et al. 1996). Therefore they may be a candidate to explain the origin and the spectral paradox of the X-ray background. Observations of nearby relatively low luminosity Seyfert 2s are suitable to measure spectral shape precisely and to understand structure around central engine.

A few X-ray observation of weak Seyfert2 galaxies are available in the literature. *BeppoSAX* observed two weak Seyfert 2s NGC 4941 and NGC 3393 and detected strong iron K emission at 6.4 keV (Salvati et al. 1997). Although the X-ray continuum of NGC 4941 is very hard, the X-ray emission in the hard energy band is consistent with both a transmitted continuum through $N_H > 4 \times 10^{23}$ cm^{-2} and a reflection dominated spectrum because of poor photon statistics. On the other hand, *ASCA* detected strong iron K emission centered at 6.7 keV from NGC 1365 and NGC 1386 (Iyomoto et al. 1997). These difference of iron line energies would be due to difference of geometry of a putative obscuring torus.

In this section, we present *ASCA* observations of low luminosity Seyfert 2 galaxies NGC 1667, NGC 2273, NGC 3079, NGC 4941, NGC 5194 (M51), and NGC 4565.

5.5.2 NGC 4941 and NGC 2273

NGC 4941

The X-ray spectra of NGC 4941 obtained with SIS and GIS are shown in Fig 5.9. Excess emission above ~ 4 keV , which suggest the hard band spectrum is obscured by a column density of $N_H > 10^{23}$ cm^{-2}, and strong line emission is visible around 6.4 keV. A simple power-law model provides reduced chi-square of 2.45 for 55 dof. A good fit is obtained by a partial covering model plus Gaussian model. The best fit parameters are summarized in Table 5.3. The best fit model is also shown in Fig 5.9. The hard component is obscured by $N_H = 1.0^{+0.5}_{-0.3} \times 10^{24}$ cm^{-2} and accompanied by a strong emission line at $6.33^{+0.07}_{-0.08}$ keV (rest frame) with an equivalent width of 760^{+410}_{-280} eV. The line center energy is consistent with iron K emission from cold or lower ionized iron. These properties are quite similar to Seyfert 2 galaxies with higher luminosities.

The observed flux in the 2–10 keV band is 1.3×10^{-12} ergs $s^{-1}cm^{-2}$, which corresponds to the luminosity of 6.4×10^{39} ergs s^{-1} at 6.4 Mpc. This observed luminosity is the smallest among Seyfert 2 galaxies observed in the X-ray regime. The intrinsic luminosity corrected for the absorption is $4.8^{+4.7}_{-2.3} \times 10^{40}$ ergs s^{-1}.

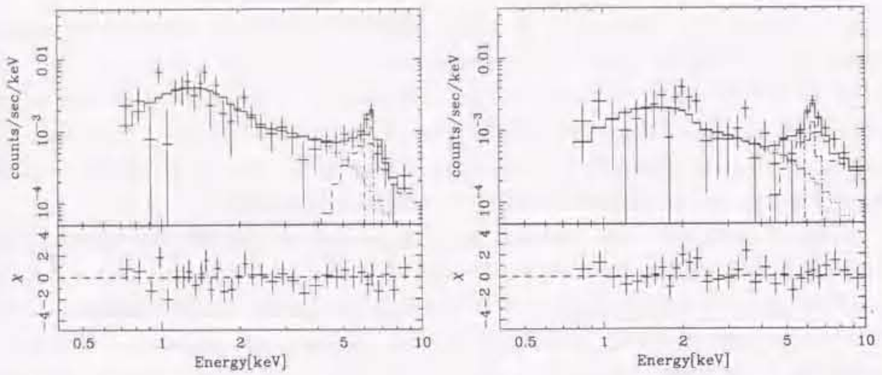

Figure 5.9: SIS (left) and GIS (left) spectra of NGC4941. The best fit partially covered power-law + Gaussian model is shown as histograms.

NGC 2273

X-ray image

Fig 5.11 shows SIS images of NGC 2273 field in the 0.5–2 keV and 2–10 keV band. NGC 2273 and one serendipitous source $\sim 2'$ south from the nucleus of NGC 2273 are detected. The serendipitous source is identified as the radio source 064542.0+605210. The X-ray images indicate NGC 2273 is bright in both soft and hard band images, while 064542.0+605210 is soft and very dim in the hard band image.

X-ray spectrum

Firstly, we extracted X-ray spectra of each sources within radii of 1.5' from NGC 2273 and 1' from the radio source using SIS data, as SIS has superior spatial resolution than GIS. Obtained X-ray spectra of these source are shown in Fig 5.12. The X-ray spectrum of the radio source is represented by a power-law model with a photon index of 1.9. On the other hand, the NGC 2273 spectrum shows hard continuum and a strong emission line around 6.4 keV. A single power-law fit gives unacceptable fit with reduced chi-square 2.2 for 16 dof. A good fit is obtained if we introduce partially covering to the power-law continuum. The best fit parameters are summarized in Table 5.15.

Observed flux of NGC 2273 is 1.14×10^{-12} ergs $s^{-1}cm^{-2}$ in the 2–10 keV band, this corresponds to observed luminosity of 1.1×10^{41} ergs s^{-1} and intrinsic luminosity of 6.1×10^{41} ergs s^{-1} at 28.4 Mpc.

Secondary, we tried to fit the SIS and GIS spectra simultaneously. In the GIS data spectra of NGC 2273 and the radio source cannot be extracted separately because of

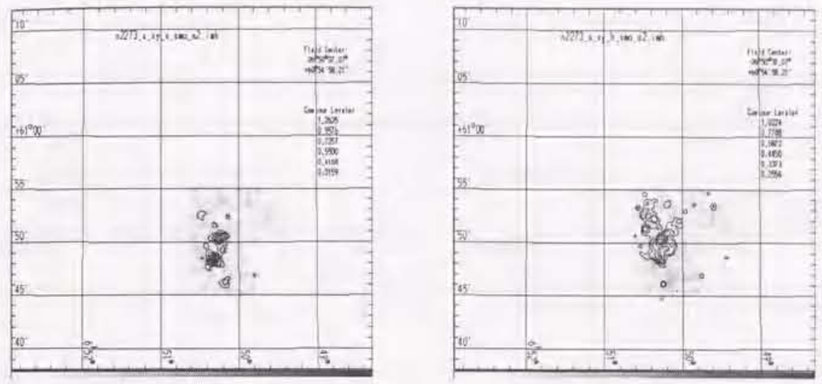

Figure 5.10: X-ray image of NGC 2273 obtained with SIS. left: 0.5–2 keV, right: 2–10 keV band.

Figure 5.11: SIS image of NGC 2273 field

coarser spatial resolution than SIS. Therefore we extracted a spectrum within 4' radius from the NGC 2273. This spectrum includes both NGC 2273 nucleus and the radio source. Then we fit three data sets (1)SIS spectrum of NGC 2273, (2)SIS spectrum of the radio source, and (3)GIS spectrum of NGC 2273 + radio source, with models; (partially covered power-law + Gaussian) for (1), absorbed power-law for (2), and (partially covered power-law + Gaussian) + absorbed power-law for (3). The spectral parameters are tied between SIS and GIS but normalizations are left free. The best fit results are summarized in Table 5.16.

The obtained fitting parameters are consistent with SIS results, but errors are small. The hard component is obscured by $N_{\rm H}$=$4.6^{+1.1}_{-1.3} \times 10^{23}$ cm^{-2}, and the continuum slope is $1.48^{+0.22}_{-0.20}$. The emission line is detected at $6.33^{+0.05}_{-0.06}$ keV (observed frame) or $6.37^{+0.05}_{-0.06}$ keV (rest frame) which is consistent with cold or lower ionized iron-K emission. The equivalent width is $1.4^{+0.5}_{-0.4}$ keV. These spectral properties are quite similar to Seyfert 2 galaxies with higher luminosities.

5.13

Table 5.15: Best fit parameters for SIS spectra of NGC 2273 and the radio source

name	model	$N_{\rm H}$ [10^{22} ergs s^{-1}]	Γ	E [keV]	σ [eV]	EW [keV]	χ^2/dof
NGC 2273	PL+Gauss	0	0.93	6.29	0(f)	6.30	32.5/15
	partial cover	$0(<0.22)$	$1.44^{+0.64}_{-0.44}$	$6.32^{+0.04}_{-0.12}$	0(f)	$1.23^{+0.14}_{-0.37}$	17.8/13
	+ Gauss	$80(>36)$	(CF $0.970^{+0.027}_{-0.07}$)				
radio source	PL	$0(<0.38)$	$1.94^{+0.91}_{-0.39}$	—	—	—	9.8/6

Table 5.16: Best fit parameters for simultaneous fitting for SIS and GIS spectra of NGC 2273 and the radio source

name	model	$N_{\rm H}$ [10^{22} ergs s^{-1}]	Γ	E [keV]	σ [eV]	EW [keV]	χ^2/dof
NGC 2273	partial cover	$0(<)$	$1.48^{+0.22}_{-0.20}$	$6.33^{+0.05}_{-0.06}$	0(f)	$1.4^{+0.5}_{-0.4}$	70.9/56
	+ Gauss	46^{+11}_{-13}	(CF $0.94^{+0.02}_{-0.03}$)				
radio source	PL	$0(<0.10)$	$2.04^{+0.39}_{-0.36}$	—	—	—	9.8/6

Table 5.17: Observed flux and luminosity in 2–10 keV (SIS)

name	observed flux [10^{-12} ergs s^{-1}cm^{-2}]	observed luminosity [10^{41} ergs s^{-1}]	intrinsic luminosity [10^{41} ergs s^{-1}]
NGC 2273	1.14	1.10	6.08
radio source	0.11		

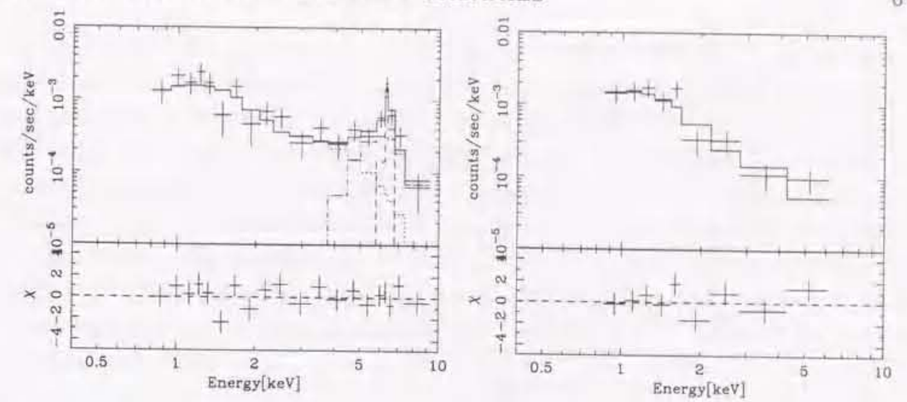

Figure 5.12: left: SIS spectrum of the NGC 2273 nucleus ($r < 1.5'$) (left). The best fit model (partially covered power-law) is shown as histogram. right: SIS spectrum of the radio source located at $\sim 2'$ from the nucleus ($r < 1'$) fitted with a power-law

Discussion

continuum shape

We detected heavily obscured hard X-ray emission from low luminosity Seyfert 2 galaxies NGC 2273 and NGC 4941. Both objects are obscured with column densities of $10^{23} - 10^{24}$ cm^{-2}. Such large obscuration is often observed in Seyfert 2 galaxies (e.g. Turner et al. 1997a, Smith & Done 1996, Awaki et al. 1991). The best fit photon index ~ 1.5 is also consistent with Seyfert 2 galaxies. The intrinsic luminosities are 1–3 orders of magnitude lower than previously observed Seyfert 2 galaxies; 6.1×10^{41} ergs s^{-1} for NGC 2273 and 4.8×10^{40} ergs s^{-1} for NGC 4941. Thus the continuum shape is very similar to higher luminosity Seyfert 2 galaxies even in very low luminosity Seyfert 2 galaxies. As shown in previous section, the photon indices of low luminosity Seyfert 1 galaxies are also quite similar to Seyfert 1 galaxies with higher luminosities. Therefore continuum shape is luminosity independent for both type 1 and type 2 Seyfert galaxies.

Narrow emission line galaxies (NELGs) with hard X-ray spectra detected in *ROSAT* surveys have optical emission line ratios classified as HII or Seyfert 2 on the excitation diagrams. Their X-ray fluxes are $F_{\rm X}(0.5\text{–}2\ {\rm keV}) < 10^{-14}$ ergs s^{-1}cm^{-2} and they are abundantly present around a redshift of ~ 0.5 (Almaini et al. 1996, 1998). Iwasawa et al. (1997) suggest that X-ray emission of NELGs is essentially come from hidden AGN based on hard X-ray spectra and large $L_{\rm X}/L_{\rm FIR}$ of AXJ 1749+684.

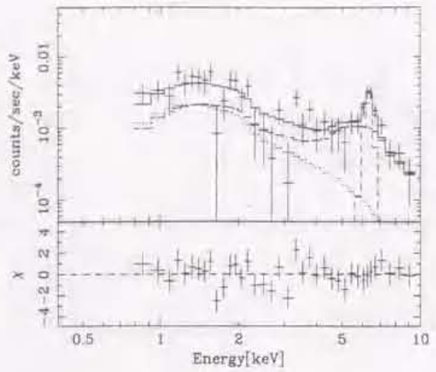

Figure 5.13: GIS spectrum of the NGC 2273 nucleus + the radio source located at $\sim 2'$ from the nucleus. The fitting is simultaneous with the SIS spectrum of each sources, but normalizations of each spectral component are left free independently.

We have shown that Seyfert 2 galaxies NGC 2273 and NGC 4941 indicate very hard X-ray spectra (see results of single power-law fit). If they are placed at a redshift of ~ 0.3, an X-ray flux of several times 10^{-16} ergs s^{-1} is expected. If relatively low luminosity Seyfert 2 galaxies are numerous even at redshifts greater than 0.1 as is local universe, this class of objects may contribute the X-ray background significantly. The optical classification of nuclear spectra could be diluted by circum nuclear starforming regions and/or starlight for distant objects and it is possible that more active galaxies are present than currently thought to be.

Obviously quantitative estimation based on larger sample of X-ray spectral measurements as well as results from surveys observation will be necessary.

iron K line

We detected strong iron K emission from NGC 2273 and NGC 4941. Such intense iron K emission is generally observed in Seyfert 2 galaxies (e.g. Turner et al. 1997a). The center energies of iron emission line from NGC 2273 and NGC 4941 are $6.33^{+0.07}_{-0.08}$ and $6.37^{+0.05}_{-0.06}$ keV (rest frame), respectively, which is consistent with fluorescence origin from cold or lower ionized iron as is observed in higher luminosity Seyfert 2 galaxies.

The iron line in Seyfert 2 galaxies are originated from obscuring matter and/or scattering matter located above the putative obscuring torus. The equivalent width of iron K emission from NGC 4941 760^{+410}_{-280} eV is consistent with that expected from transmission through the observed column density $N_{\rm H}=1.0^{+0.5}_{-0.3} \times 10^{24}$ cm^{-2}. On the other hand, the strong iron emission from NGC 2273 (equivalent width of $1.4^{+0.5}_{-0.4}$ keV) is rather large compared to calculation of iron equivalent width produced by transmission through $N_{\rm H}=4.6^{+1.1}_{-1.3} \times 10^{23}$ cm^{-2}. This suggest that there is significant contribution from reflection component possibly due to inner surface of a putative torus as several Seyfert 2 galaxies (Malaguti et al. 1997, Matt et al. 1996, Reynolds et al. 1994, Fukazawa et al. 1994; see also Turner et al. 1997b). Alternatively, luminosity decrease of central continuum source also explain the strong iron emission. Iron line emitting matter is located far from the nucleus, iron line intensity remains constant after luminosity decline of the nucleus (Iwasawa et al. 1994).

5.5.3 NGC 5194 (M51)

The SIS and GIS spectra were extracted from a region within 3' of the M51 nucleus in radius and fitted simultaneously. Only data from SIS0 chip1 and SIS1 chip3 were used for extracting SIS spectra since most of the source flux fell on these chips. The count rates of M51 for the SIS and GIS were 0.05 counts s^{-1} and 0.03 counts s^{-1}, respectively. Although the companion galaxy, NGC 5195, is located $\sim 4'$ to the north of M51, its X-ray flux is about 1/4 that of M51 in the 0.5–10 keV band according to the present *ASCA* observation, therefore the flux from NGC 5195 does not significantly affect the results on M51.

X-ray images

The *ASCA* SIS0+1 image of M51 in the 0.5–10 keV band is shown in Figure 1. The X-ray emission from M51 and the companion NGC 5195 is clearly detected. The discrete sources detected in the *ROSAT* (Marston et al. 1995; Ehle et al. 1995; Read et al. 1997) and *Einstein* (Palumbo et al. 1985) observations are not clearly seen in the *ASCA* image and only hints of the sources A and B in Palumbo et al. (1985) are seen.

In order to evaluate spatial extent of the X-ray emission, we examined a brightness profile of the SIS0 image (the SIS have superior spatial resolution to the GIS). We used a rectangular region parallel to the detector x-axis, as shown in Figure 1. The brightness profile projected onto the detector x-axis in this region is shown in Figure 2 for the 0.5–2 keV, 2–5 keV, and 5–10 keV energy bands. The histogram in Figure 2 represents the point spread function of the *ASCA* XRT + SIS in each energy range at the source position projected onto the detector x-axis in the same way as actual data. The brightness distribution is thus clearly extended in the 0.5–2 keV and 2–5 keV energy bands compared

to the point spread function. On the other hand, the image in the 5–10 keV band is consistent with the point spread function, although photon statistics are poor.

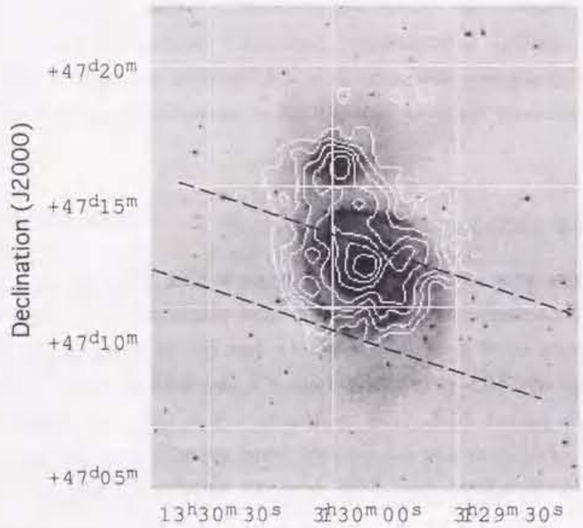

Figure 5.14: Contour map of M51 and NGC 5195 taken with SIS detectors (SIS0 + SIS1) superposed on optical image. Background is not subtracted. The contour levels are logarithmically spaced. The region between dashed lines is used to make a projected brightness profile.

X-ray Spectra

The SIS and GIS spectra are shown in Figure 3. These spectra clearly show emission lines around 1 keV, which indicate the presence of sub-keV, optically-thin plasmas, and neither the simple power-law nor thermal bremsstrahlung models provide acceptable fits. A single temperature Raymond-Smith thermal plasma model (Raymond & Smith 1977) also poorly fitted the data and significant hard tail residuals remained. Additionally, emission-line-like residuals were also seen around 6.4 keV. Accordingly, we fitted the

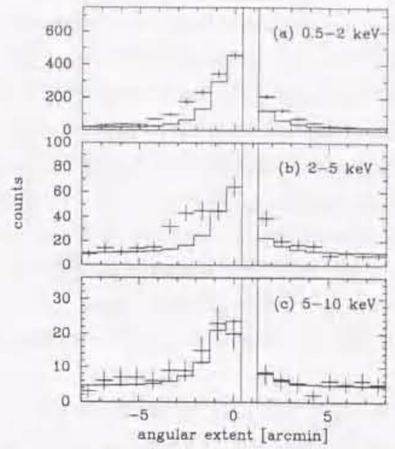

Figure 5.15: Brightness profile projected onto the detector x-axis in (a)0.5–2 keV, (b)2–5 keV, and (c)5–10 keV. The crosses are SIS0 data and the histogram represents the point spread functions of XRT + SIS added on background level. The region at an angle of ∼1 arcmin corresponds to the inter-chip gap of the SIS detector.

spectra with a combination of a Raymond-Smith plasma, a power-law and a Gaussian model, where we assumed Galactic absorption ($N_{\rm H}$= 1.3×10^{20} cm^{-2}; Stark et al. 1992). The fitting results are summarized in Table 1. The reduced chi-square was 1.242 for 142 d.o.f. in this model. However, emission-line-like residuals still remained at ∼0.65 keV, 0.9–1.0 keV and ∼1.9 keV which we identified as H-like O-K, He and H-like Ne-K and He-like Si-K emission lines, respectively. These residuals suggest a non-solar abundance ratio and/or a multi-temperature plasma. We further examined two models: (1) power-law + $2kT$-Raymond-Smith plasma + Gaussian model and (2) power-law + variable abundance Raymond-Smith plasma + Gaussian model. The best-fit parameters are also summarized in Table 1. We obtained significant improvement in the fit and the reduced chi-square was 1.01 and 0.997 for 142 and 140 d.o.f., using models (1) and (2) respectively. Then we allowed the absorption column density for the hard component to vary in the models (1) and (2), where the hydrogen column density for the Raymond-Smith component was fixed to the Galactic value. We obtained only an upper limit of $N_{\rm H}$=1.2×10^{22} cm^{-2} at 90% confidence for one interesting parameter ($\Delta\chi^2$= 2.7).

The SIS and GIS spectra and the best-fit model for the variable abundance case are shown in Figure 2. The X-ray luminosities of the hard power-law component and the Raymond-Smith component are 1.1×10^{40} ergs s^{-1} in the 2–10 keV bandpass and 1.2×10^{40}

ergs s^{-1} in the 0.5–2 keV bandpass, respectively. The X-ray luminosity of the power-law component is about six times lower than that obtained with *Ginga* (6.7×10^{40} ergs s^{-1}) in the 2–10 keV band , while the spectral slope of the hard component ($\Gamma = 1.43^{+0.17}_{-0.38}$) agrees well with the *Ginga* results of a power-law fit in the 2–20 keV band ($\Gamma = 1.43 \pm 0.08$). In this model, the addition of the narrow Gaussian line at 6.4 keV improved chi-square by $\Delta\chi^2$= 15.7 for the two additional parameters. Therefore the line feature is statistically significant at more than 99.9% confidence level for two additional degrees of freedom (line center energy and line intensity). The line center energy, $6.40^{+0.08}_{-0.12}$ keV implies the K-line of nearly neutral iron. The equivalent width was determined to be 910^{+410}_{-380} eV for the variable abundance case. The confidence contours for the line center energy and the line flux are shown in Figure 4.

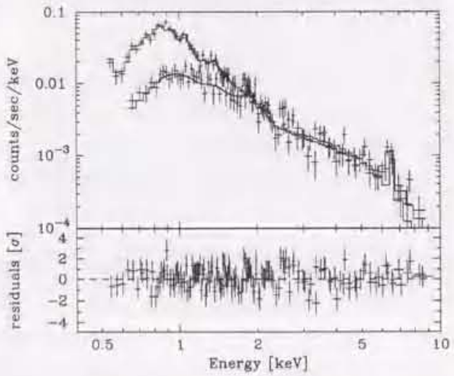

Figure 5.16: *ASCA* SIS and GIS spectra of M51. The solid lines represent the best-fit model of a combination of a variable abundance Raymond-Smith model, a power-law, and a Gaussian.

Discussion

Hard X-ray emission and an iron emission line

The X-ray spectrum from M51 is represented by a combination of a hard component with a photon index of ~ 1.4 and a thermal emission component with $kT \sim 0.4$ keV. The luminosity of the hard component is $L_{2-10\ \mathrm{keV}} = 1.1 \times 10^{40}$ ergs s^{-1}. This luminosity is about six times lower than that measured with *Ginga* (Makishima et al. 1991). Additionally a strong fluorescent iron emission line is found at 6.4 keV with an equivalent width

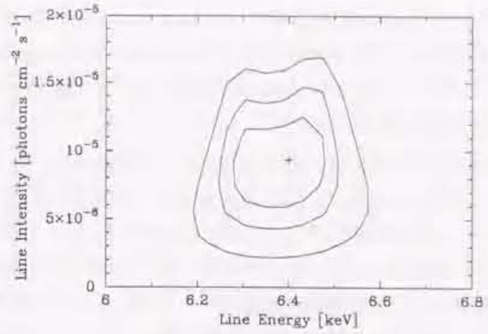

Figure 5.17: Confidence contours for the iron line energy and normalization. Contour levels correspond to 68, 90, and 99% confidence levels from inside to outside.

of ∼900 eV.

In normal spiral galaxies, X-ray emission is dominated by discrete sources such as low-mass X-ray binaries (LMXBs) (Fabbibano 1989; Makishima et al. 1989). The X-ray luminosity of M51 obtained with *ASCA* is only a factor of two larger than that of the normal spiral galaxy M31 which is dominated by LMXBs (Makishima et al. 1989). The X-ray to B-band luminosity ratio of M51, $L_{2-10\ \mathrm{keV}}/L_{\mathrm{B}} \sim 5.9 \times 10^{-5}$, is also close to those of normal spiral galaxies (e.g. $L_{\mathrm{X}}/L_{\mathrm{B}}$=3.5 × 10^{-5} for M31; Makishima et al. 1989). Therefore a significant portion of the observed hard X-ray luminosity from M51 is likely to come from the superposition of LMXBs. The extended image in the 2–5 keV band also supports this interpretation. However, the observed spectral slope of the hard component ($\Gamma \sim 1.4$) is harder than those of LMXBs , which are roughly equivalent to $\Gamma \sim 1.8$. Moreover, the observed strong iron emission line cannot be explained by the emission form LMXBs. Therefore the presence of an additional flat spectral component, accompanied by an iron line, is strongly inferred.

The iron emission line at 6.4 keV is of fluorescence origin from cold material irradiated by a strong X-ray source (an Fe line produced thermally from hot gas would have had an energy in excess of 6.7 keV). The large equivalent width of ∼900 eV is expected primarily when the X-ray source is obscured by hydrogen column density significantly greater than 10^{23} cm^{-2}(Makishima 1986). Thus the observed iron emission line strongly suggests the presence of an obscured X-ray source. A strong iron line of an equivalent width as large as $\sim$ 1 keV, ,which is not accompanied by high absorption of low energy X-rays, has been seen in heavily obscured Seyfert 2 galaxies, in which the hydrogen column density is

thought to exceed 10^{24} cm^{-2} (e.g. NGC 1068, Koyama et al. 1989; NGC 4945, Iwasawa et al. 1993; NGC 1365, Iyomoto et al. 1997). Their continua are interpreted as being dominated by X-rays scattered into the line of sight by partially ionized material in the opening part of the obscuring torus.

In M51, however, the X-ray image above 2 keV is extended by more than several arcminutes in diameter, which requires that scattering material is extended over galaxy scales. A possibility for reconciling the spectral results with the extended image in the 2–5 keV band is that the AGN emission contributes only to the hardest end of the *ASCA* spectra. We examined a spectral model consisting of a combination of a soft thermal component, a LMXBs component approximated by a 7 keV thermal bremsstrahlung (Makishima et al. 1989), and an absorbed power-law from an AGN. Since the photon statistics are limited, we fixed the photon index for the power-law component at 1.4, which is typical for Seyfert 2 galaxies observed with *Ginga* (Awaki et al. 1991b), and the temperature of the thermal bremsstrahlung component at 7 keV. We assumed the hydrogen column density at the Galactic value for the soft thermal component and the LMXBs component. For the power-law component, the hydrogen column density was fixed to values between 5×10^{23} cm^{-2} and 1×10^{24} cm^{-2}. A good fit was obtained for these assumed values of absorption column densities with a reduced chi-square of 0.985 (138 d.o.f.) for $N_{\rm H}$= 5×10^{23} cm^{-2} , for example. The intrinsic luminosity of the absorbed component, corrected for absorption, varied from 1.5×10^{40} to 3.7×10^{40} ergs s^{-1} when the absorption column was changed from 5×10^{23} cm^{-2} to 1×10^{24} cm^{-2}. The equivalent width of the iron line was then calculated as $\sim 1.1 \pm 0.6$ keV. An equivalent width that exceeds 1 keV is rather large to be a typical obscured Seyfert 2 galaxy (e.g. Awaki et al. 1991b), although the errors are large. This large equivalent width may also be a result of variability of the continuum emission from the nucleus. If the light crossing time over the distance from the nucleus to the emitting region of the iron line is larger than the variability time scale of the nucleus, a variation of iron line flux would be delayed relative to a continuum variation. Therefore in this case after the continuum emission decreases a large iron line equivalent width might be expected.

Alternatively it is also possible that reflected X-rays from an AGN dominates the hard band spectrum. In such a case, a large equivalent width of iron K line up to 1–2 keV with respect to the reflected continuum would be expected (George & Fabian 1991). Indeed, an extremely strong iron line is observed from the Seyfert 2 nucleus in NGC 6552 (Fukazawa et al. 1994; Reynolds et al. 1994) and the Circinus galaxy (Matt et al. 1996). The observed equivalent width of the iron line is $\sim$ 0.9 keV and $\sim$ 2 keV in NGC 6552 and the Circinus galaxy, respectively. These remarkable X-ray spectra are interpreted as

being dominated by X-rays reflected from cold matter. A spectral model for the hard component, consisting of a thermal bremsstrahlung (fixed to kT=7 keV) and a reflected continuum (the `plrefl` model in XSPEC), also reproduced the observed spectrum (with a reduced chi-square 0.997 for 138 d.o.f.) (Figure 5). For the reflection component, we assumed an incident photon index of 2.0 and a face-on disk which subtends a solid angle 2π as seen from the iraddiating source. An equivalent width of $1.5^{+0.6}_{-0.7}$ keV was obtained with respect to the reflected continuum. The 2–10keV luminosity of the reflected component was 3.9×10^{39} ergs s^{-1}, while that of the bremsstrahlung component was 7.7×10^{39} ergs s^{-1}. The best fit parameters for the soft Raymond-Smith component are similar to the results presented in Table 1. These results are consistent with the reflection dominated model, which can explain the extended image in the 2–5 keV band, the compact image in the 5–10 keV band, and the large equivalent width of the iron emission line, at the same time.

The 2–10 keV luminosity we measured is about six times lower than that derived with *Ginga* (Makishima et al. 1990). Although we cannot rule out the possibility that the *Ginga* LAC field of view was contaminated by other sources, the overall spectral slope ($\Gamma \sim 1.4$) obtained with *Ginga* in the 2–20 keV band is very similar to that derived with *ASCA*. Therefore, the apparent flux discrepancy between *Ginga* and *ASCA* may be due to time variations in the AGN of M51. In fact, when we increase the incident luminosity of the reflection component in Figure 5 by $\sim$ 5 times, and raise its escape fraction up to $\sim$ 10%, the spectrum and flux obtained with the *Ginga* LAC can be approximately reproduced. A gradual luminosity change of this order has actually been observed from the M81 nucleus (Ishisaki et al. 1996).

Thermal emission

The presence of diffuse hot gas across the galaxy has been pointed out on the extended X-ray images of M51 obtained with *ROSAT* (Ehle et al. 1995, Marston et al. 1995, Read et al. 1997). The *ASCA* spectra, exhibiting various low-energy emission lines (OVIII, NeIX, NeX, MgXI, Fe L line complex), give a strong support to the *ROSAT* results.

The results of a variable abundance Raymond-Smith plasma plus a hard component model fit indicates kT $\sim$0.4 keV and a low iron abundance compared to other elements such as O, Ne, Mg, and Si. The 2-kT Raymond-Smith plus a hard component model also gives an acceptable fit. Hot gas component with these characteristics have been observed from starburst galaxies such as M82 and NGC 253 (Ptak et al. 1997; Moran & Lehnert 1997; Tsuru et al. 1997). Furthermore, the X-ray luminosity to far-infrared luminosity

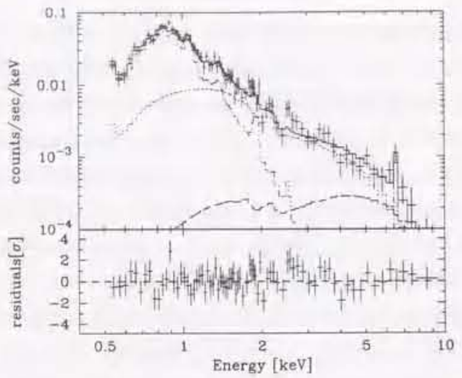

Figure 5.18: Reflection plus low mass X-ray binaries model fit for the hard component. Though fitting of SIS and GIS data were done simultaneously, only SIS data is shown for clarity.

ratio of M51, $\log(L_{\rm X}/L_{\rm FIR}) = -4.1$, is similar to those of starburst galaxies (Heckman, Armus, & Miley 1990; David, Jones, & Forman 1992), where $L_{\rm X}$ is the luminosity of the Raymond-Smith component and $L_{\rm FIR}$ is the far infrared luminosity of 60μm plus 100μm IRAS measurements calculated using equation (1) in David et al (1992). These facts suggest that the X-ray-emitting gas originates mainly from active star formation. Thus our results support the starburst driven winds interpretation of the diffuse emission in the *ROSAT* images (Read et al. 1997; Ehle et al. 1995), especially from a spectral point of view.

Table 5.18: Results of model fitting to the SIS and GIS spectra of M51

Parameter	Power-law + RS	Power-law + $2kT$ RS	Power-law + variable abundance RS
$N_{\rm H}$ (10^{20} cm^{-2})	1.3 (fixed)	1.3 (fixed)	1.3 (fixed)
hard component			
Power-law photon index Γ	1.13 (0.84–1.35)	1.01 (0.94–1.34)	1.43 (1.05–1.60)
Line energy (keV)	6.41 (6.26–6.49)	6.41 (6.26–6.49)	6.40 (6.28–6.48)
Equivalent width (eV)	720 (390–1120)	720 (410–1090)	910 (530–1320)
soft component			
kT (keV)	0.50 (0.46–0.55)	0.29 (0.26–0.32)	0.42 (0.38–0.52)
	—	0.82 (0.78–0.86)	—
Abundance (solar)	0.027 (0.020–0.035)	0.10 (0.086–0.12)	—
O	—	—	0.11 (0.054–0.20)
Ne	—	—	0.29 (0.27–0.49)
Mg	—	—	0.12 (0.012–0.30)
Si	—	—	0.42 (0.18–0.81)
Fe	—	—	0.055 (0.033–0.065)
χ^2/d.o.f.	176.4/142	141.0/140	137.6/138

5.5.4 NGC 4565

X-ray image

Fig 5.19 shows SIS0+1 raw image of NGC 4565 in the 0.5-10 keV . A bright X-ray source is detected at ~0.7' west of the nucleus. There is another X-ray source coincides with the optical nucleus. These sources can be identified with *ROSAT* PSPC sources RXJ 1236.2+2558 (source A32 in Vogler et al. 1996) and (RXJ 1236.3+2559 (source A34 in Vogler et al. 1996), respectively.

In order to evaluate X-ray fluxes of these sources, we made a projected image along them with a width of 30 pixel (= 3.2') and the obtained profile was fitted with the PSF of the XRT + SIS at the source positions plus constant background, where the PSF is made using the ray-tracing code and projected in the same way as the actual data. The projected profiles in the 0.5–2 keV and 2–10 keV band obtained with SIS0 are shown in Fig 5.20. The best fit PSF + background model is also shown in the same figure. Both

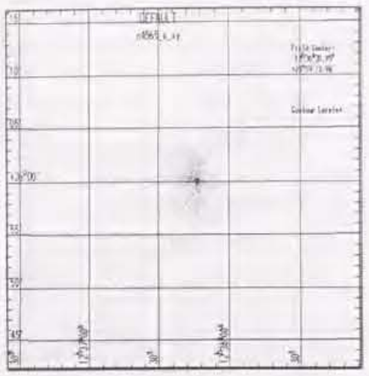

Figure 5.19: X-ray image of NGC 4565 obtained with SIS in the 0.5–10 keV

sources are point-like and well represented by the PSF in both soft and hard band. The 0.5–2 keV and 2–10 keV photon fluxes of the nucleus are $48 \pm 8\%$ and $48 \pm 10\%$ of those of the off center source, respectively, in contrast to the fluxes of the nucleus and east source are comparable in the *ROSAT* PSPC image. This fact suggests that X-ray flux at least one source varied between *ROSAT* and *ASCA* observations. There are systematic residuals about 3' east of the nucleus suggesting the presence of another faint X-ray source. This source can be identified with RXJ 1236.5+2559 (the source A43 in Vogler et al. 1996).

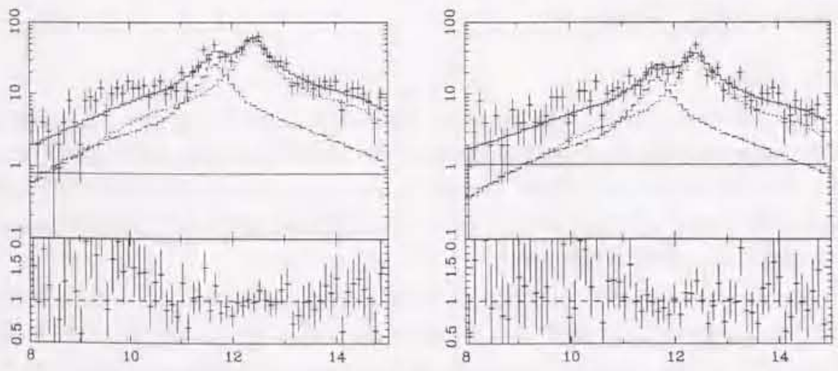

Figure 5.20: X-ray brightness projected along the nucleus and the off center source, left: 0.5–2 keV, right: 2–10 keV. Lower panels are data/model.

X-ray spectrum

Since the nuclear source and off center source is separated only 0.7', we cannot extract their X-ray spectra separately. Therefore we extracted X-ray spectra of both sources within a radius of 6' for GIS and 4' for SIS. Other X-ray sources are dim and do not make a significant contribution to the extracted spectra.

We fitted the spectra with a single power-law and deficit of data was seen around 2 keV, which suggest that hard X-ray emission is obscured by a column density $> 10^{22}$ cm^{-2}, and fits are not acceptable (χ^2/dof = 164/112) (Table 5.1). We tried to fit the spectra with two power-law model with different amount of absorption. The photon indices for these two power-law are agree with each other within statistical errors. Therefore photon indices are tied (equivalent to a partially covered power-law model) and good fits were obtained (Table 5.3).

There is a hint of emission lines around $\sim$1.4 keV, which is identified with He-like and H-like Mg lines, and infer the presence of thermal plasmas with $kT \sim 1$ keV. Then we added Raymond-Smith plasma model to above partial covering model. Since the abundance value is not strongly constrained ($Z > 0.03 Z_{\odot}$), we fixed it at the chi-square minimum 0.27. Addition of the RS component improves chi-square $\Delta\chi^2 = 4.6$. The results of a partial covered power-law + RS model is shown in Table 5.4. We also examined a RS with iron abundance left free and abundances of α elements fixed at 0.5. A better fit was obtained with chi-square improvement of $\Delta\chi^2 = 8.0$ compared to the partial covered power-law model. The results are summarized in Table 5.5. For a model accompanied with a variable abundance RS plasma, the best fit photon index, absorption column densities, and covering fraction are $2.70^{+0.34}_{-0.43}$, $3.1^{+0.7}_{-0.8} \times 10^{22}$ cm^{-2} and $0.53^{+0.18}_{-0.22} \times 10^{22}$ cm^{-2}, and $0.69^{+0.09}_{-0.07}$, respectively. The best fit spectra are shown in Fig 5.21 and the incident model spectrum is shown in Fig 5.22.

The observed and intrinsic (absorption corrected) luminosities are 1.8×10^{40} ergs s^{-1} and 2.5×10^{40} ergs s^{-1} in the 2–10 keV band, respectively. The X-ray luminosity of the soft thermal component is 3.7×10^{39} ergs s^{-1} in the 0.5–4.0 keV band. According to above image analysis, the flux of the nuclear source is $\sim 1/2$ of the off center source. Then the observed X-ray luminosity of these sources are obtained to be 6×10^{39} ergs s^{-1} and 1.2×10^{40} ergs s^{-1} in the 2–10 keV band, respectively. No significant iron line is detected in the hard band spectra.

X-ray emission obscured with a column density of 3×10^{22} cm^{-2} is detected and the apparent spectral slope ($\Gamma = 2.70^{+0.34}_{-0.43}$) is much steeper than those of Seyfert galaxies ($\Gamma = 1.7 - 2.0$). However the obtained X-ray spectrum is dominated by the off center source ($\sim 2/3$ of total flux), and does not reflect the X-ray spectrum of the nucleus. The

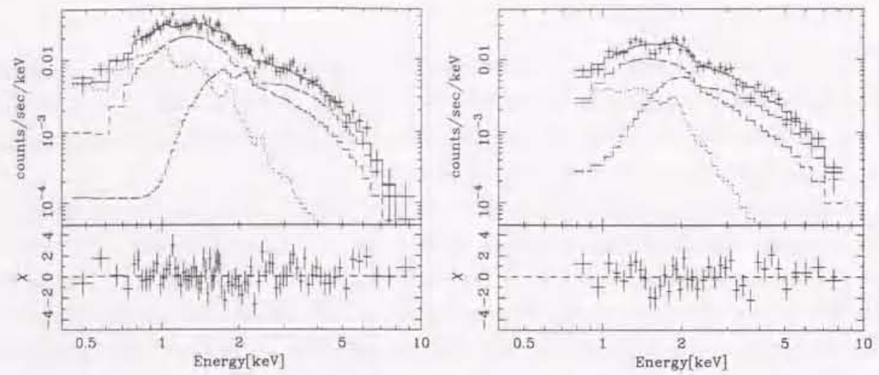

Figure 5.21: X-ray spectra of NGC 4565. left: SIS, right: GIS. Note both nuclear source and the off center source are included.

projected brightness profiles indicate the hardness of nuclear source is similar to the off center source and we cannot separate spectral components from each of sources. Therefore we use only the flux value for discussion. We assume that the 2–10 keV flux of the nucleus is 1/3 of the total flux, i.e. 6.0×10^{39} ergs s^{-1}. As discussed in §6.1, the ratio $L_X/L_{H\alpha}$ located well within the range of low luminosity AGNs, supporting the X-ray nucleus is the ionizing source of the optical emission lines.

The nuclear source is consistent with point-like. NGC 4565 is a relatively nearby galaxy, we can securely conclude that contribution from the discrete sources distributing over the host galaxy is negligible.

5.5.5 NGC 3079

The X-ray images of NGC 3079 in 0.5–2 keV band is extended compared to the point spread function of the XRT+SIS, while the 4–10 keV image is consistent with a point source. The X-ray spectra clearly show various emission lines such as K emission of He-like O, He-like and H-like Ne, He-like and H-like Mg, He-like Si, and iron L line complex. Therefore we tried a R-S + power-law model and acceptable fit is obtained (Table 5.4). We also examined a variable abundance R-S + power-law model. Since abundance value of each elements are not strictly constrained, we assume the abundace of the α elements (O, Ne, Mg, Si) is 0.5 solar, and only iron abundance is varied. The fit is significantly improved ($\Delta\chi^2 = 16.3$) for one additional degree of freedom (Table 5.5). The X-ray spectra and the best fit model are shown in Fig 5.23. The hard component is represented by a power-law

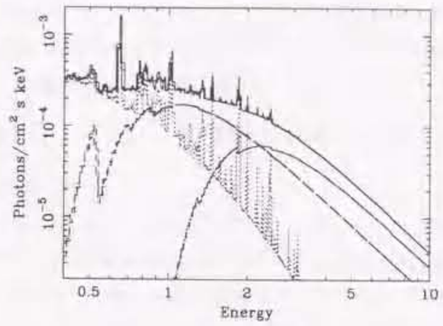

Figure 5.22: The best fit model of NGC 4565 including both the nuclear source and the off center source.

with a photon index of 2.0 ± 0.7 modified by some absorption $1.8^{+1.7}_{-1.3} \times 10^{22}$cm^{-2} and the intrinsic luminosity of this component is 2.5×10^{40} ergs s^{-1}.

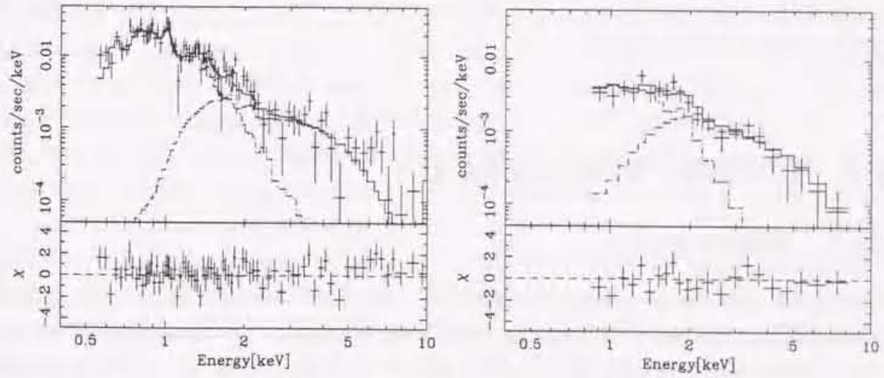

Figure 5.23: X-ray spectra of NGC 3079. left: SIS, right: GIS

5.5.6 NGC 1667

NGC 1667 is dim in X-rays and has a very soft spectrum. In the hard band image above 2 keV, NGC 1667 is almost invisible. Because of the soft spectrum, photon statistics of the GIS spectrum is very poor. Therefore we fit the SIS spectrum in the 0.5–5 keV range. The SIS spectrum is shown in Fig 5.24. The X-ray spectrum is well reproduced

by a power-law model with a photon index of $2.3^{+0.8}_{-0.4}$. The absorption column density $N_{\rm H} < 1.6^{21}$ cm^{-2} is consistent with the Galactic value (5.5×10^{20} cm^{-2}). The extrapolated 2–10 keV flux and luminosity are $9 \pm 4 \times 10^{-14}$ ergs s^{-1}cm^{-2} and $4 \pm 2 \times 10^{40}$ ergs s^{-1}, respectively.

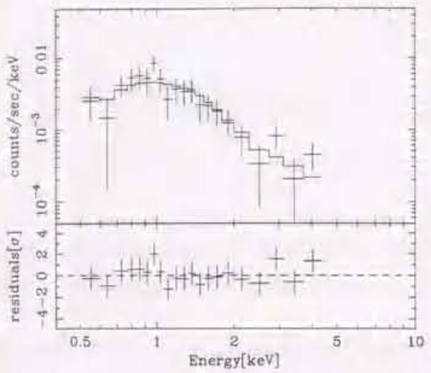

Figure 5.24: X-ray spectrum of NGC 1667 obtained with SIS. The best fit power-law model is shown as a histogram.

5.6 LINERs with broad Hα

5.6.1 Introduction

The optical spectroscopic surveys revealed that about one-third of nearby bright galaxies have LINER nuclei (see §2). Several possible origin of LINERs are proposed. The detection of broad Hα in optical spectra from 20% of LINERs (Ho et al. 1997b) and X-ray nuclei in some objects support the low luminosity AGN origin among several mechanisms.

The observation in the X-ray band can provide evidence of the presence of an AGN such as bright and hard X-ray nucleus, time variability, iron fluorescence lines, and so on. However few X-ray observations are available, because of limited sensitivity and/or energy band of previous observations. Here we report *ASCA* observations of LINERs with broad Hα. LINERs without broad Hα will be discussed in the following sections.

LINERs with broad Hα are the candidates of low luminosity AGNs among numerous LINERs, since broad line widths suggest that the line emitting gas is moving under strong gravity, and therefore suitable to study X-ray properties of low luminosity AGNs. We

present results of six LINERs with broad Hα NGC 1052, NGC 3998, NGC 4203, NGC 4438, NGC 4450, NGC 4594, and NGC 5005.

5.6.2 NGC 3998, 4203, 4450, 4594, and 5005

NGC 3998

NGC 3998 is bright X-ray source and detected with count rates of 0.29 counts s^{-1} per SIS and 0.18 counts s^{-1} per GIS. The X-ray image is point-like in both below and above 2 keV and the radial profiles of surface brightness are well represented by the PSF. No significant intensity variability is detected within a one day observation.

The X-ray spectra obtained with SIS and GIS detectors are shown in Fig 5.25. The X-ray spectra are fitted with a power-law model with a photon index of 1.89 ± 0.03 and small absorption $8.8 \pm 1.2 \times 10^{20}$ cm^{-2} No significant low energy emission lines are seen. There is a hint of iron K emission around 6.4 keV and we tried to add an Gaussian component to the power-law model. Since we cannot set a stringent constraints on the line width because of very weak line feature, we assumed the width of the Gaussian to be narrow. An addition of a narrow Gaussian improved $\Delta\chi^2 = 4.1$ and obtained line center energy and equivalent width are $6.40^{+0.11}_{-0.20}$ keV (observed) and 90 ± 70 eV (90% for one interesting parameter), respectively. The line center energy corresponds to $6.42^{+0.11}_{-0.20}$ keV in the rest frame. Obtained reduced χ^2 value for the power-law + Gaussian model is 1.19 for 280 dof. Fig 5.26 shows the confidence contours for the line center energy and line intensity, where the line width is again fixed at $\sigma = 0$, . The line center energy is consistent with fluorescence from cold iron, although He-like iron (6.7 keV) cannot be rejected at 90% confidence level for two interesting parameters. The iron line is statistically significant at 95.6% if we assume a narrow 6.4 keV line according to F-test for one additional parameter (line normalization) or at 82 % for two additional parameters (line center energy and line normalization).

The observed X-ray flux in the 2–10 keV is 8.1×10^{-12} ergs s^{-1}cm^{-2} which corresponds to 4.5×10^{41} ergs s^{-1} at 21.6 Mpc. This luminosity is about 60% of the luminosity obtained with *Ginga* on 1988 Apr 30 – May 1 (7.5×10^{41} ergs s^{-1} in 2–10 keV).

NGC 4203

X-ray image

Fig. 5.27 shows an X-ray image obtained with SIS0 + SIS1 in the 0.5–10 keV band. A bright X-ray source is detected at the position of the optical nucleus within position determination errors. Another bright source is detected about 2' South-East of the nucleus. The position of this off-nuclear source coincides with the position of TON 1480

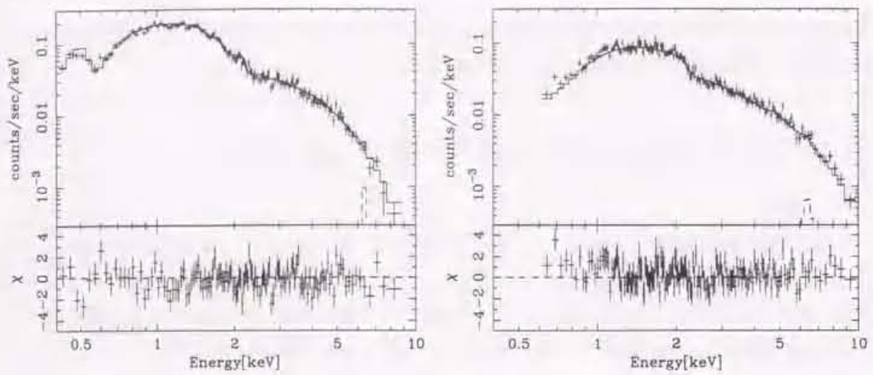

Figure 5.25: X-ray spectra of NGC 3998. left: SIS, right: GIS

(12h15m9.2s, 33d9m55.8s) (J2000).

In the GIS2 + GIS3 image (Fig 5.27), there are two more sources at (12h14m04s, 33d9m20s) and (12h14m26s, 33d11m20s). The former coincides with the position of QSO 1211+334 (12h14m04.2s, 33d09m46s) and the latter has no counter part in the NED.

The nucleus of NGC 4203, TON 1480, and QSO 1211 are also detected in a *ROSAT* PSPC image. The source without known counter part is clearly detected in the GIS image, not detected in the SIS and the *ROSAT* PSPC image. Although these facts suggest the source would have hard X-ray spectrum, it is too dim to measure a 2–10 keV flux using the GIS image.

X-ray spectrum

Since the separation between the nucleus of NGC 4203 and TON 1480 is only 2', we extracted the spectra using small radii; 1.2' for SIS and 1.5' for GIS. Firstly, we fit SIS spectra of NGC 4203 and TON 1480 with a power-law model to measure their spectral shape and an X-ray flux. The spatial resolution of SIS is superior to that of GIS and we can measure X-ray spectra and fluxed of these sources with small contamination from the other source. The spectrum of TON 1480 obtained with SIS is shown in Fig5.29. The NGC 4203 spectra are shown in Fig5.28. The fitting results for the SIS spectra are summarized in Table 5.19. Their X-ray spectra are well represented by a power-law model with little absorption. The photon indices are very similar to each other; 1.72 ± 0.1 for NGC 4203 and 1.81 ± 0.07 for TON 1480. Although the X-ray flux of TON 1480 is $\sim 73\%$ of that of NGC 4203, photons from TON 1480 in the GIS spectrum of NGC 4203 does not affect the spectral fitting results significantly. We fit the SIS and GIS spectra of NGC 4203 simultaneously with a power-law model, where the normalizations of model functions for

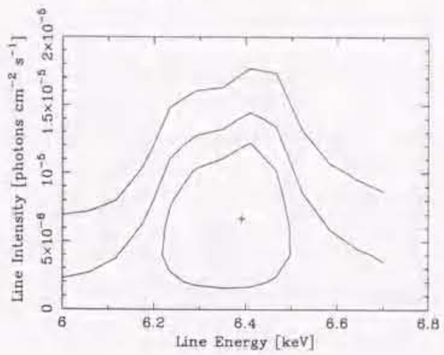

Figure 5.26: Confidence contours for the line energy and intensity for NGC 3998. The line width is assumed to be narrow. The contours correspond to 68%, 90%, and 99% confidence level for two interesting parameters ($\Delta\chi^2 = 2.3$, 4.6, and 9.2, respectively).

Table 5.19: Spectral fitting results of SIS spectra

	$N_{\rm H}$ [10^{20} cm^{-2}]	photon index	flux (2–10 keV) [10^{-12} ergs s^{-1}cm^{-2}]
NGC 4203	$1.8(<5.6)$	1.72 ± 0.1	2.2
TON 1480	<1.3	1.81 ± 0.07	1.6

SIS and GIS are left free separately. The best fit parameters are summarized in Table 5.1. The obtained photon index 1.77 ± 0.08 is quite similar to Seyfert 1 galaxies and the absorption column density is consistent with the Galactic value ($N_{\rm H}$=1.3 × 10^{20} cm^{-2}; Stark et al. 1992). The X-ray flux in the 2-10 keV band is 2.1×10^{-12} ergs s^{-1}cm^{-2}. We examined the presence of iron K emission by adding a narrow Gaussian at 6.4 or 6.7 keV to the fitting model. The chi-square value was not improved and upper limits for a 6.4 and 6.7 keV line is 300 eV and 260 eV, respectively.

fitting results of SIS spectrum

NGC 4450

The X-ray spectra of NGC 4450 can be fitted with a power-law model (reduced chi-square of 1.03 for 70 dof). However there is small excess around 0.7–1 keV. We tried a Raymond-Smith + power-law model and the chi-square improvement of $\Delta\chi^2 \sim 8$ is

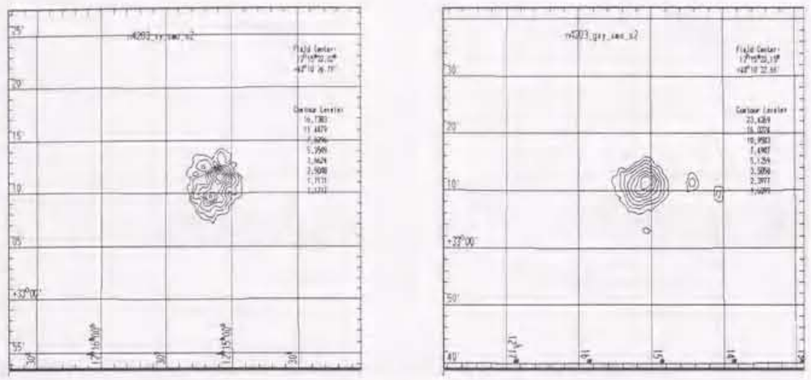

Figure 5.27: X-ray image of NGC 4203. left: SIS image in the 0.5–10 keV band, right: GIS image in the 0.7–10 keV band.

obtained, where we assumed the abundance of 0.1 solar or 0.5 solar since we cannot constrain the abundance value because of the weak line feature. The variable abundance Raymond-Smith + power-law model improves only $\Delta\chi^2 = 1.2$. The X-ray spectra and the best fit Raymond-Smith + power-law model are shown in Fig 5.30 and the best fit parameters are shown in Table 5.4. No significant iron K emission is detected.

NGC 4594

The X-ray image in the 0.5–2 keV range is extended compared to the point spread function, while the hard band image in 2–10 keV is point-like.

The X-ray spectra are not represented by a single power-law model and positive residuals are visible around 0.7–1 keV. In the spectral fittings, the normalization for SIS and GIS are varied separately, as SIS provides systematically lower normalization by $\sim 10\%$. Since the pointing position (2CCD nominal position) is close to the inter-chip gap of the CCDs, this systematic difference is probably due to photon loss into the gap. Secondary, we introduced a Raymond-Smith thermal plasma and a better fit is obtained. We tried to vary abundance of iron separately from that of alpha elements. Since abundance of iron and alpha elements cannot be well constraint independently, we assumed iron abundance of 0.5 solar and obtained relative abundance. The chi-square value improves $\Delta\chi^2$=5.0 from this model. The X-ray spectra are shown in Fig 5.31 along with the best fit variable abundance Raymond-Smith + power-law model. The best fit parameters are summarized

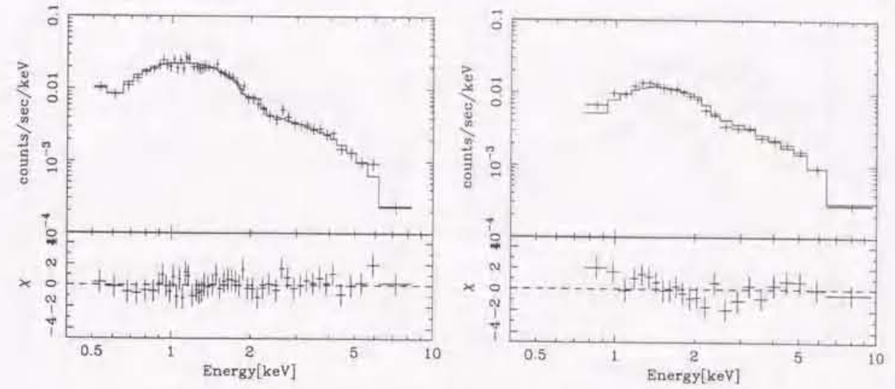

Figure 5.28: X-ray spectra of NGC 4203. left: SIS, right: GIS

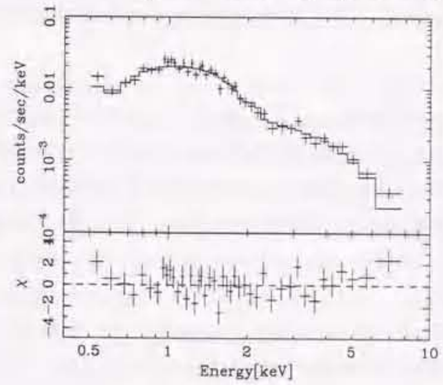

Figure 5.29: X-ray spectrum of TON 1480 obtained with SIS.

in Table 5.4 and Table 5.5.

NGC 5005

The X-ray image of NGC 5005 looks extended. The azimuthally averaged surface brightness profiles of SIS images are compared with the point spread function + constant background model. The radial profiles in the 0.5–2 keV and 2–10 keV band are shown in Fig 5.32. Systematic residuals suggest the X-ray source is not point-like and extended to $\sim 2'$ in radius. Actually fittings with a PSF + background model provide reduced chi-square of 1.42 (0.5–2 keV) and 1.61 (2–10 keV) for 11 dof. The X-ray spectra show relatively strong broad line like feature around 0.7–1 keV and hard emission. A Raymond-

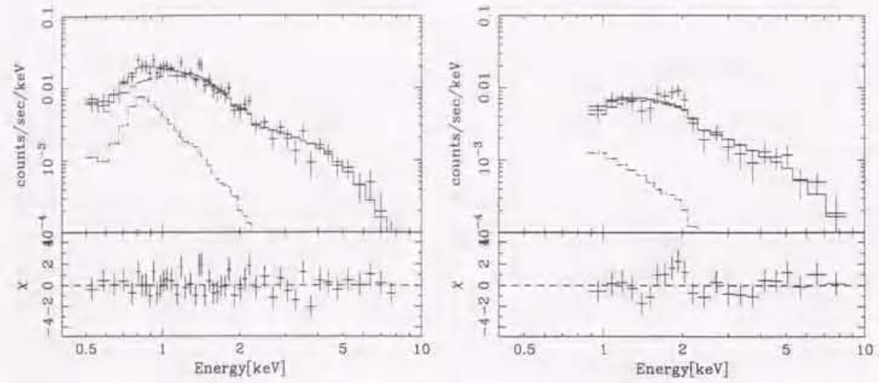

Figure 5.30: X-ray spectra of NGC 4450. left: SIS, right: GIS. The best fit Raymond-Smith + power-law model is shown as a histogram. The abundance of the soft thermal component is assumed to be 0.1 solar.

Smith + power-law model well fit the observed spectra. The best fit parameters and spectra are shown in Table 5.4 and Fig 5.33, respectively. The obtained temperature and abundance are similar to other object analyzed here. However the photon index of the power-law component $\Gamma = 0.97 \pm 0.37$ is significantly harder than other LINERs which show photon indices around ~ 1.8.

Discussion

We detected hard X-ray emission from all of NGC 3998, NGC 4203, NGC 4450, NGC 4594, and NGC 5005. The 2–10 keV images obtained with SIS is point like except for NGC 5005. As is discussed in §6.1, these objects show correlation between Hα and X-ray luminosity observed in Seyfert galaxies. and strongly suggest that optical emission lines are ionized by photoionization by high energy photons emitted from low luminosity AGNs.

The hard X-ray spectrum is well represented by a power-law with a photon index ~ 1.8 but for NGC 5005. This spectral slope is quite similar to Seyfert 1 galaxies (e.g. Nandra et al. 1997b). On the other hand, iron emission lines, which is generally observed from Seyfert 1 galaxies, are not observed except for marginal detection in NGC 3998. Detailed comparison to higher luminosity AGNs will be presented in §6.2.

The photon index of $1.22^{+0.43}_{-0.34}$ from NGC 5005 is harder than other objects. The signature of extended hard X-ray image infer the significant contribution from discrete sources such as low mass X-ray binaries (LMXBs) in the host galaxies as in normal spiral

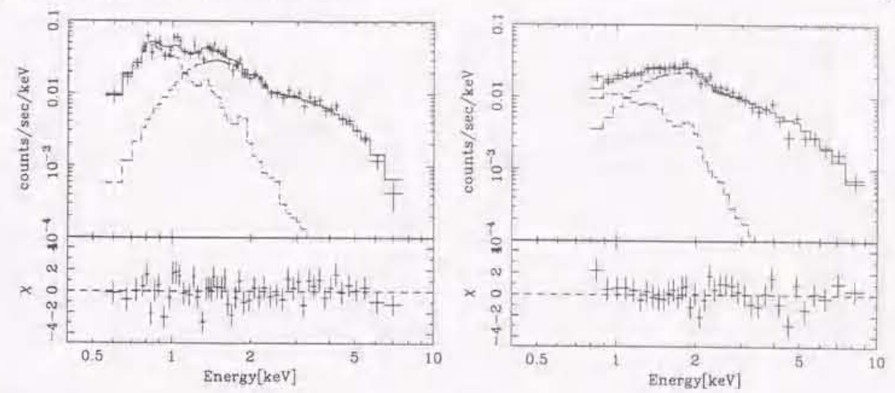

Figure 5.31: X-ray spectra of NGC 4594. left: SIS, right: GIS. The best fit variable abundance Raymond-Smith + power-law model is shown as a histogram.

galaxies. However X-ray spectrum of NGC 5005 is harder than the spectrum of LMXBs whose spectrum is approximated by thermal bremsstrahlung of several keV. Similar hard X-ray spectrum is observed from the starburst galaxy NGC 1808 (Awaki et al. 1996). A power-law fit to the hard component of NGC 1808 provides photon index of $1.3^{+0.3}_{-0.4}$. Awaki et al. (1996) attributed the hard X-ray spectrum to high mass X-ray binaries produced by the starburst activity. Since NGC 5005 also shows starburst activity, similar interpretation would be possible. We cannot exclude the possibility of the presence of an obscured AGN. However, the extended hard band image suggest that the obscured AGN does not contribute to X-ray flux significantly.

5.6.3 NGC 1052

Results

image

NGC 1052 is detected at the position of the optical nucleus and some serendipitous sources are also detected. The brightest one is NGC 1042 at (2h40m23.7s, -8d25m59.9s) (J2000), which is an Scd galaxy with a nucleus classified as an HII nucleus based on detection of an $H\alpha$ emission line and an upper limit of [NII] line (Keel 1983). X-ray images in the 0.5–2 keV and 2–10 keV band are consistent with the point spread function. The azimuthally averaged profiles of surface brightness is well fitted with the point spread function with reduced chi-square of 1.30 in 0.5–2 keV and 0.88 in 2–10 keV for 11 dof.

spectrum

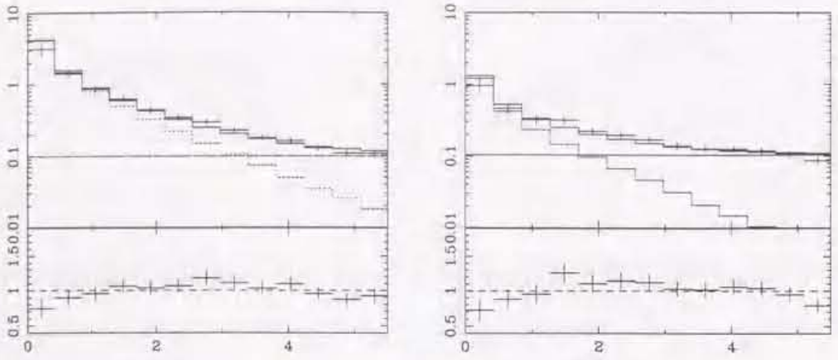

Figure 5.32: Radial profiles of surface brightness in the 0.5–2 keV (left) and 2–10 keV range for NGC 5005. Solid lines are the best fit model of point spread function of SIS + XRT superposed on constant background. Lower panels show data/model.

The X-ray spectra of NGC 1052 show turnover above ~3 keV and a power-law fit to the spectra provides an extremely flat photon index ($\Gamma \sim 0.2$) and unacceptable reduced chi-square (χ^2_ν=2.2 for 111 dof). These spectral shape suggest that the hard component suffers from heavy absorption of order of 10^{23} cm^{-2} and that medium hardness component with small absorption is also present. Additionally, an emission like feature is seen around 6.4 keV. Therefore we fit the spectra with partial covered power-law + Gaussian model. Although the fit is significantly improved ($\Delta\chi^2$=112), positive residuals are seen around 0.7–1 keV. Then we add a Raymond-Smith thermal plasma model to above model. This model fits the data well (χ^2_ν=1.00 for 104 dof) and the best fit spectra are shown in Fig 5.34.

The best fit parameters are summarized in Table 5.4. Observed flux and luminosity in the 2–10 keV band are 4.8×10^{-12} ergs s^{-1}cm^{-2} and 1.8×10^{41} ergs s^{-1}, respectively, and the intrinsic luminosity corrected for absorption is 3.8×10^{41} ergs s^{-1} in 2–10 keV (Table 5.9). Fig 5.35 shows the best fit model spectrum and Fig 5.36 shows the confidence contours for the absorption column density — the covering fraction, and the line center energy — line intensity. In this model, an addition of a narrow Gaussian improved chi-square $\Delta\chi^2$=12.1 for two additional parameters (line center energy and normalization).

Discussion

Emission from obscured AGN

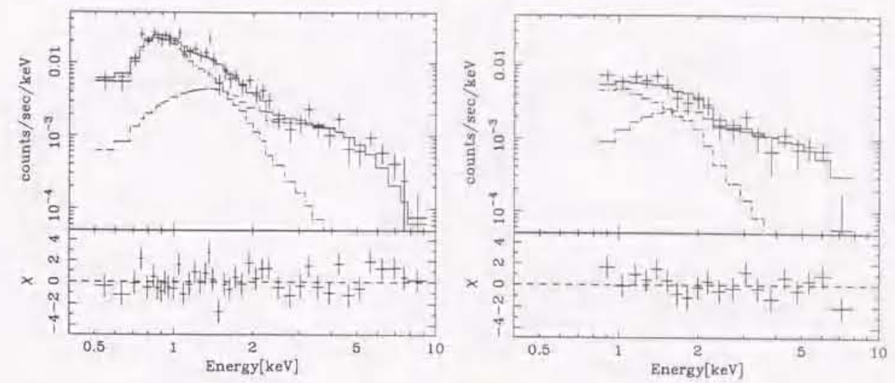

Figure 5.33: X-ray spectra of NGC 5005. left: SIS, right: GIS. The best fit Raymond-Smith + power-law model is shown as a histogram.

We detected a hard X-ray emission absorbed by a column density of $\sim 10^{23}$ cm^{-2} which is most likely from an obscured AGN. NGC 1052 is the first example of a LINER with a significant absorption ($N_{\rm H} >\sim 10^{23}$ cm^{-2}).

The continuum slope $1.67^{+0.57}_{-0.40}$ and absorption column density $N_{\rm H} = 2.0^{+0.7}_{-0.8} \times 10^{23}$ cm^{-2} are typical for Seyfert 2 galaxies with higher luminosities (e.g. Turner et al. 1997a). Iron K emission is also detected at 6.32 ± 0.08 keV with an equivalent width of 180^{+80}_{-90} eV. This equivalent width is consistent with expected from transmission through the equivalent hydrogen column density of $\sim 2 \times 10^{23}$ cm^{-2} (Turner et al. 1997a, b; Leahy & Creighton 1993).

NGC 1052 is known as an H_2O megamaser source (Braatz, Wilson, & Henkel 1994, 1996). Our X-ray measurement of the X-ray spectrum shows the nucleus is obscured by $\sim 2 \times 10^{23}$ cm^{-2}. H_2O megamasers are expected when we are seeing the AGN from almost edge on view. We confirmed all of the H_2O megamaser source is obscured by column density of more than 10^{23} cm^{-2} but for NGC 3079 (Table 5.20).

origin of the soft component

As NGC 1052 is an early type galaxy (E4), extended halo of thermal plasma would by present. *ROSAT* PSPC spectrum are fitted with a RS model with $kT = 2.9^{+5.9}_{-1.3}$ keV, which is significantly higher than typical temperature of elliptical galaxies and inconsistent with $kT - \sigma$ correlation (Davis & White 1996). This is likely to be due to emission from the AGN significantly contributes to the *ROSAT* band. If we assume iron L complex is due

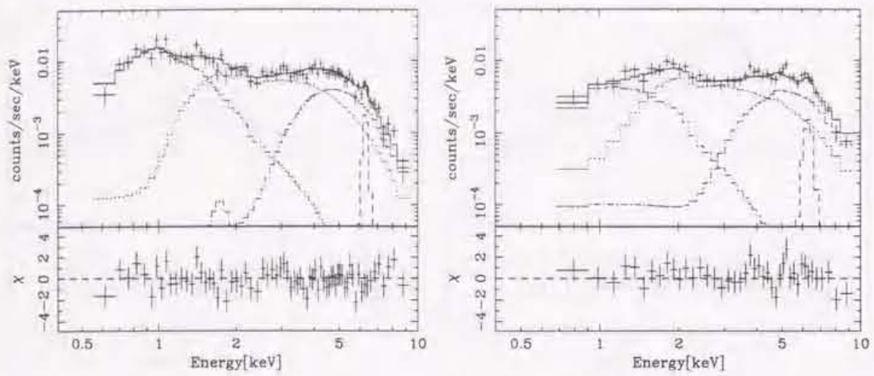

Figure 5.34: X-ray spectra of NGC 1052. left: SIS, right: GIS

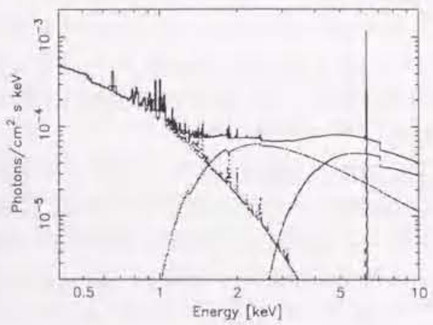

Figure 5.35: The best fit model spectrum of NGC 1052.

to a thermal plasma and AGN emission is represented by partially covered power-law, temperature of $kT = 1.0^{+2.2}_{-0.3}$ keV and abundance of $0.04^{+0.06}_{-0.04}$ solar are obtained. These values are well within the $kT - \sigma$ and $kT-$abundance correlations by Davis & White (1996).

5.6.4 NGC 4438

X-ray image

ASCA observations of NGC 4438 were performed on 1995 Dec. 24 and 1996 Jan. 5 for 20 ksec each. NGC 4438 is detected at the position coincides with the optical nucleus (12h27m45.6s, +13d00m32s) (J2000) and one serendipitous source is detected at

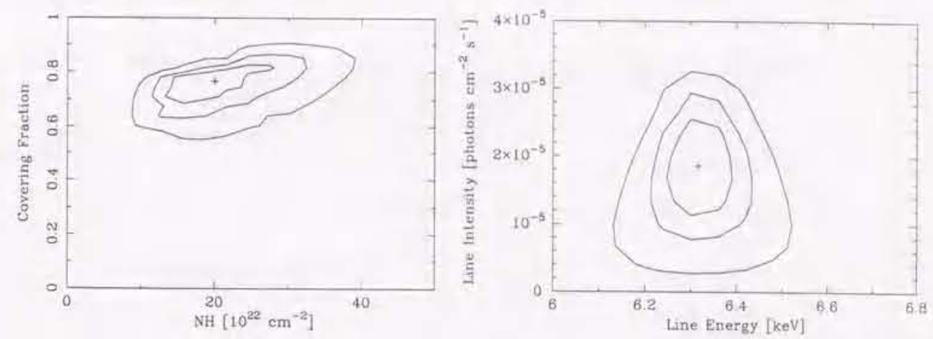

Figure 5.36: Confidence contours for the absorption column density and the covering fraction (left), and the line center energy and line intensity. The contours correspond to 68%, 90%, and 99% confidence level for two interesting parameters ($\Delta\chi^2 = 2.3$, 4.6, and 9.2, respectively).

(12h27m57s, +13d02m22s). Additionally diffuse emission due to an intracluster gas of the Virgo cluster of galaxies is seen and becomes brighter towards South-East which is the direction to the M87.

The X-ray flux of NGC 4438 is very low (0.01 counts s^{-1} per 1SIS and 0.004 counts s^{-1} per 1GIS) and there is no significant flux change between two observations. Therefore we present the results of analyses based on combined data of two observation.

X-ray spectrum

We extracted the X-ray spectra using a 2' radius region centered at NGC 4438 to minimize the photons from the serendipitous source and the Virgo cluster emission. Background spectra are accumulated from the source free region in the same field to subtract the diffuse cluster emission.

The X-ray spectra cannot be fitted with a simple power-law or thermal bremsstrahlung model. Excess emission is seen around 0.8–1 keV which indicate the presence of thermal plasmas of $kT < 1$ keV. We fit the spectra with a power-law + Raymond-Smith (RS) model and a good fit is obtained. Since the abundance of the RS plasmas is not constrained, we assumed the abundance of 0.1 solar or 0.5 solar. The fitting results are summarized in Table 5.4. The power-law slope and absorption column density for the power-law component are not well constrained because of poor statistics and couples with the soft RS component. For example the photon index of $\Gamma = 2.0^{+1.5}_{-1.0}$ and absorption column density $N_{\rm H} = 1.4^{+3.9}_{-1.4} \times 10^{22}$ cm^{-2} are obtained for an assumed abundance of 0.1

Table 5.20: X-ray absorption in H_2O mega maser detected objects.

Galaxy	class	$N_{\rm H}$ [10^{23} cm^{-2}]	reference
NGC 1052	L1.9	$2.4^{+1.0}_{-0.8}$	this work
NGC 1068	S2	> 10	1
NGC 1386	S2	$5.4^{+4.2}_{-2.9}$	2
Mrk 1210	S2	$2.0^{+0.8}_{-0.6}$	3
NGC 3079	S2	—	this work
NGC 4258	S1.9	1.5 ± 0.2	4
NGC 4945	S2	40^{+20}_{-12}	5, 6
Circinus	S2	> 10	7
ESO 103-G35 (1988)	S2	$1.8^{+0.4}_{-0.3}$	8
ESO 103-G35 (1991)	S2	2.2 ± 0.3	9

references: (1)Koyama et al. 1989, (2)Iyomoto et al. 1997, (3)Ueno 1995, (4)Makishima et al. 1994, (5)Iwasawa et al. 1993, (6)Done et al. 1996, (7)Matt et al. 1996, (8)Warwick et al. 1993, (9)Smith & Done 1996

solar. No significant iron line is detected and upper limit of the equivalent width of a narrow line at 6.4 keV is 1.3 keV. The X-ray flux of the hard component in the 2–10 keV band is $2.7 \pm 0.5 \times 10^{-13}$ ergs s^{-1}cm^{-2} for assumed abundances 0.5 or 0.1 solar. These fluxes correspond to the X-ray luminosities of $9.1 - 9.5 \times 10^{39}$ ergs s^{-1} at a distance of 16.8 Mpc. The soft component is represented by a RS plasma model of $kT \sim 0.76$ keV and the X-ray flux in the 0.5–4 keV band is $\sim 2 - 4 \times 10^{-13}$ ergs s^{-1} for an assumed abundance between 0.5 and 0.1 solar, which corresponds to 6.8×10^{39} ergs s^{-1}–1.5×10^{40} ergs s^{-1}.

We detected very weak X-ray emission from NGC 4438. The Hα flux of this object is large ($F_{\rm H\alpha}$=7.1×10^{-14} ergs s^{-1}; Ho et al. 1997a) and nearly the same as the Seyfert 1.5 galaxy NGC 5033 ($F_{\rm H\alpha}$=5.0×10^{-14} ergs s^{-1}) and the LINER/Seyfert 1.9 galaxy NGC 4579 ($F_{\rm H\alpha}$=8.1×10^{-14} ergs s^{-1}) from which bright X-ray emission is detected. However observed X-ray flux is only $\sim 3 \times 10^{-13}$ ergs s^{-1}cm^{-2} which is more than an order of magnitude smaller than NGC 5033, NGC 4579 and a flux expected from the $L_{\rm X}/L_{\rm H\alpha}$ correlation for low luminosity Seyfert galaxies and LINERs with broad Hα discussed above. This X-ray weakness suggest following possibilities; (1) the AGN is heavily obscured and/or (2) dominant excitation mechanism of LINER emission lines are not photoionization by low luminosity AGN.

If AGN is present and powering the all Hα luminosity, AGN should be obscured to

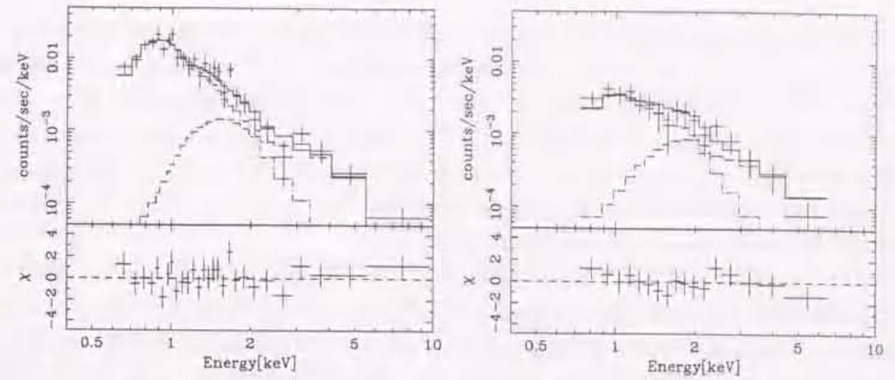

Figure 5.37: X-ray spectra of NGC 4438. left: SIS, right: GIS

explain observed small 2–10 keV $L_{\rm X}/L_{\rm H\alpha}$ ratio. Although the obtained X-ray spectrum show no indication of absorption, this would be explained if other component such as X-ray binaries in the galaxy dominates the 2–10 keV flux as in M51 (NGC 5194; §5.5.3, Terashima et al. 1998a). Heavily obscured AGNs generally exhibit-e strong fluorescent iron K emission with an equivalent width of more than several hundreds of eV (e.g. Turner et al. 1997a). The upper limit of an iron emission line at 6.4 keV is $\sim$ 1.3 keV, which cannot exclude the presence of iron emission like Seyfert 2s.

Alternatively, other ionizing source may be present in stead of an AGN. Since the LINER optical emission lines are emitted from extended region (ref), significant fraction of them may be driven by processes such as circumnuclear starformation or cooling flows.

In summary, we found no X-ray evidence for the presence of an AGN. If AGN is present, it is required to be heavily obscured to explain small $L_{\rm X}/L_{\rm H\alpha}$ ratio compared to low luminosity Seyfert galaxies and other 'AGN-like' LINERs with broad Hα emission. Then weak broad Hα (Ho et al. 1997b) is likely to be scattered component.

5.7 LINERs without broad Hα

5.7.1 Introduction

Excitation mechanism of a LINER is still under debate and most likely to be heterogeneous, including photoionization by a low luminosity AGN, photoionization by very hot stars, shock, and so on. Broad Hα emission is detected from about 10% of LINERs. Broad Balmer lines are indicator of genuine AGN candidate, since broad line width

(>1000 km s^{-1}) infer that the line emitting gas is moving under strong gravity by super massive blackholes. As shown in the previous sections, hard X-ray emission is actually detected from LINERs with broad Hα and strongly supports they are genuine AGNs with very low luminosities ($L_X < 10^{41}$ ergs s^{-1}). If the origin of a LINER is heterogeneous, LINERs without broad Hα component (hereafter referred as LINER 2) are good candidates to investigate ionizing source of LINERs other than low luminosity AGNs. No detailed study of LINER 2 is done in the X-ray regime, so far.

In the case that LINER 2s are genuine AGNs, emission from the nucleus may be obscured in analogy to Seyfert 2s. Since LINER 2s are quite numerous ($\sim 30\%$ of bright galaxies), significant fraction of bright galaxies may harbor obscured AGNs. Recent X-ray surveys and optical follow up observations show narrow emission line galaxies (NELGs) (including HII nuclei, Seyfert 2s, and LINER 2s) become dominant population at a low X-ray flux ($< 1 \times 10^{-13}$ ergs $s^{-1}cm^{-2}$) in the 0.5–2 keV band (Almaini et al. 1996) and their X-ray spectra are harder than broad lined AGNs such as QSOs. At present, most of the X-ray sources are classified as HII nuclei, Seyfert 2s by optical follow up observations (Boyle et al. 1995). At a faint flux, LINER 2s may be a important class, since LINERs tend to be less luminous than Seyferts, and they may contribute to the X-ray background (XRB) significantly. Alternatively, they may be very dim X-ray sources and not important as the origin of the XRB, specifically in the case of most of LINER 2s are not genuine AGNs.

X-ray observations at energies above 2 keV is essential to clarify ionization mechanisms in LINERs and to search for faint obscured AGNs, which may be contribute to the XRB significantly. We selected objects with large Hα fluxes and observed them with *ASCA*. If LINER 2s are genuine AGNs, large X-ray fluxes are expected, since X-ray fluxes are proportional to Hα fluxes even for low luminosity AGNs (see §6). If observed X-ray fluxes are very small, it means that AGN is not present or that AGN is negligibly contribute to X-ray emission. We present here the X-ray results of LINER 2s NGC 404, NGC 4569, and NGC 7217. These galaxies are bright in Hα and indicate no broad Hα emission.

5.7.2 NGC 404, 4569 and 7217

NGC 404

NGC 404 is not detected with the exposure time of ~ 14 ksec. We fit the one dimensional projection with a width of 3' of SIS images in the 2–10 keV and fit this profile with the point spread function + constant background model. Obtained a 3σ upper limit of the

X-ray flux is $\sim 2 \times 10^{-13}$ ergs s^{-1} in the 2–10 keV band assuming an X-ray spectrum of a power-law with a photon index of 1.8.

NGC 4569

X-ray emission from NGC 4569 is detected at the position coincides with the optical nucleus (Fig. 5.38) with count rates of 0.02 counts s^{-1} and 0.007 counts s^{-1} for SIS and GIS, respectively. Some serendipitous sources are detected in the GIS field of view (Table 5.21). The source #5 is identified with the QSO Q1235+1335 at a redshift of 0.15. Additionally diffuse emission is seen over the GIS field. This emission is due to emission from the hot gas in the Virgo cluster of galaxies, since NGC 4569 is located from 2.1 deg from M87 (Böhringer et al. 1994).

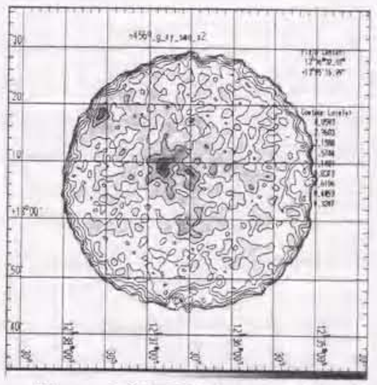

Figure 5.38: GIS image of the NGC 4569 field

The GIS image shows some X-ray sources and diffuse emission around NGC 4569. In order to minimize photons from these sources, we extracted spectra from 3' radius region for both SIS and GIS. Background spectra for SIS are extracted using outside of 4' radius circle centered at NGC 4569 on the same chip. Backgrounds for GIS are accumulated from an annular region centered on NGC 4569.

The X-ray spectrum cannot be explained by simple power-law or thermal bremsstrahlung model, and positive residuals are clearly seem around 0.7–1 keV, which is identified with iron L emission from sub-keV thermal plasma. Therefore we introduced a Raymond-Smith thermal plasma model in addition to an absorbed power-law, where absorption column

Table 5.21: Source positions detected in the NGC 4569 field

source No.	position (J2000)	ID
0	(12h36m50s, +13d09m10s)	NGC 4569 (12h36m49.8s, +13d09m46s)
1	(12h36m30s, +13d08m20s)	
2	(12h36m14s, +13d08m40s)	
3	(12h36m38s, +13d12m00s)	[faint]
4	(12h36m34s, +12d08m40s)	[extended?]
5	(12h37m33s, +13d18m25s)	QSO Q1235+1335 (12h37m33.6s, +13d19m6.6s)

density for the RS component is fixed at the Galactic value (2×10^{20} cm^{-2}; Stark et al. 1992).

The best fit photon index and absorption column density are $\Gamma = 2.1 \pm 0.6$ and $N_{\rm H}$=$1.5^{+1.0}_{-1.3} \times 10^{22}$ cm^{-2}, respectively. The soft component is represented by a RS model with $kT = 0.69^{+0.08}_{-0.12}$ keV and abundance = $0.1^{+0.6}_{-0.06}$ solar. We also examined a model RS + thermal bremsstrahlung and equal quality of fit was obtained with the best fit temperature of $kT = 8.1(> 3.3)$ keV and $N_{\rm H}$=$0.74(< 1.9) \times 10^{22}$ cm^{-2}. The spectral parameters for the soft component is same as the RS + power-law fit.

Although spectral shape is well represented by this model, the best fit normalization values are different between SIS and GIS. From the fitting of the spectra extracted from r=4'region, the 2–10 keV fluxes are obtained to be $3.7^{+0.6}_{-0.5} \times 10^{-13}$ ergs s^{-1}cm^{-2} for SIS and $2.4^{+0.7}_{-0.4} \times 10^{-13}$ ergs s^{-1}cm^{-2} for GIS. The 0.5–4 keV fluxes of the RS component are $4.2^{+0.5}_{-0.4} \times 10^{-13}$ ergs s^{-1}cm^{-2} for SIS and $2.4 \pm 0.4 \times 10^{-13}$ ergs s^{-1}cm^{-2} for GIS. These results are almost same for the spectra of r=3' region. These discrepancy between fluxes from different instruments are probably due to different contribution of serendipitous sources and the diffuse emission. We regard these values as possible uncertainties of background subtraction and use the average of flux value between SIS and GIS $3.1^{+1.2}_{-1.1} \times 10^{-13}$ in 2–10 keV in the following discussions. This flux corresponds to $1.05^{+0.41}_{-0.37} \times 10^{40}$ ergs s^{-1} at a distance of 16.8 Mpc. The 0.5–4 keV flux and luminosity of the RS component are $3.3^{+1.4}_{-1.3} \times 10^{-13}$ ergs s^{-1}cm^{-2} and $1.1^{+0.5}_{-0.4} \times 10^{40}$ ergs s^{-1}, respectively.

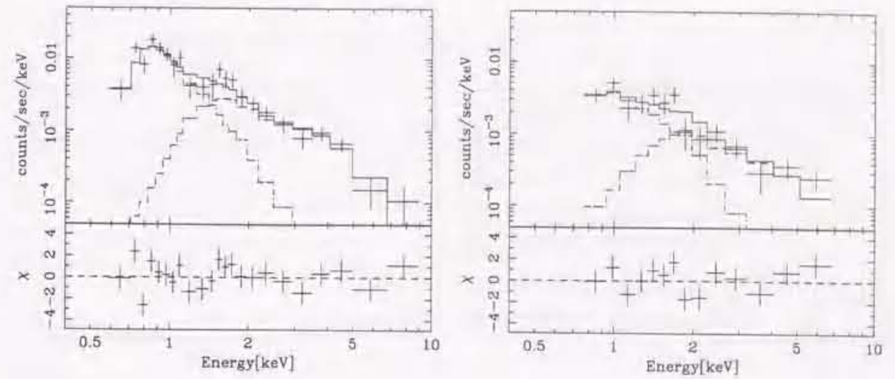

Figure 5.39: SIS (left) and GIS (left) spectra of NGC 4569. Histogram represents the best fit R-S plus power-law model

NGC 7217

NGC 7217 and some serendipitous sources are detected in the field of view (Fig 5.40). The position of these sources are summarized in Table 5.22. These serendipitous sources have no counter part in the NASA Extragalactic Database. The X-ray images of NGC 7217 in the 0.5–2 keV and 2–10 keV band obtained with SIS are consistent with the point spread function.

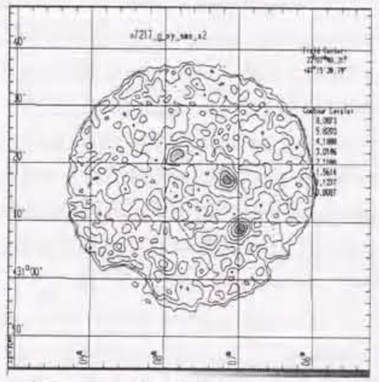

Figure 5.40: GIS image of the NGC 7217 field

Since the serendipitous sources #5 and #1 are located at 9'–10' from NGC 7217, we extracted GIS spectra using 4' radius region centered at the NGC 7217 nucleus to avoid

Table 5.22: Source positions detected in the NGC 7217 field

source No.	position (J2000)	ID
0	(22h07m54s, +31d21m15s)	NGC 7217 (22h07m52.3s +31d21m32s)
1	(22h07m12s, +31d16m54s)	
2	(22h07m00s, +31d08m48s)	
3	(22h07m27s, +31d06m40s)	
4	(22h08m02s, +31d02m54s)	
5	(22h08m09s, +31d13m08s)	

the photons from these sources. Background spectra are extracted from the blank sky observations released from the NASA Guest Observer Facility using the same region on the detector as extracted region of the source spectra. SIS spectra are extracted from a region of 4' radius. NGC 7217 and source #1 are located on SIS0 chip1 / SIS1 chip3 and SIS0 chip0 / SIS1 chip2, respectively, and contribution of photons from source #1 to the SIS0 chip1 / SIS1 chip3 is small. Therefore the spectrum of outer region ($r > 4$' from NGC 7217) is used as a background.

X-ray spectra cannot be represented by simple model (single power-law or thermal bremsstrahlung) and residuals suggest the presence of a soft component accompanied by excess emission in 0.7–1 keV. We tried the canonical model (absorbed power-law + Raymond-Smith thermal plasma), where abundance is fixed at 0.5 solar as poor statistics prevent us making a stringent constraint on the abundance value. The best fit parameters are summarized in Table 5.4 and the SIS and GIS spectra with the best fit model are shown in Fig 5.41. The best fit photon index of the hard component $2.2^{+0.6}_{-0.4}$ is somewhat steeper than the typical value from Seyfert galaxies ($\sim 1.7 - 2.0$). The excess absorption column density $\sim 10^{22}$ cm^{-2} is required in addition to the galactic value 9×10^{20} cm^{-2} (Stark et al. 1992). The observed spectra are also fitted with an absorbed thermal bremsstrahlung + Raymond-Smith thermal plasma model. The flux in the 2–10 keV band is 2.0×10^{-13} ergs s^{-1}cm^{-2} for these models (Table 5.8).

Discussion

We observed three Hα bright LINERs without broad Hα and detected very weak X-ray emission from NGC 4569 and NGC 7217. No significant X-ray emission is detected from NGC 404.

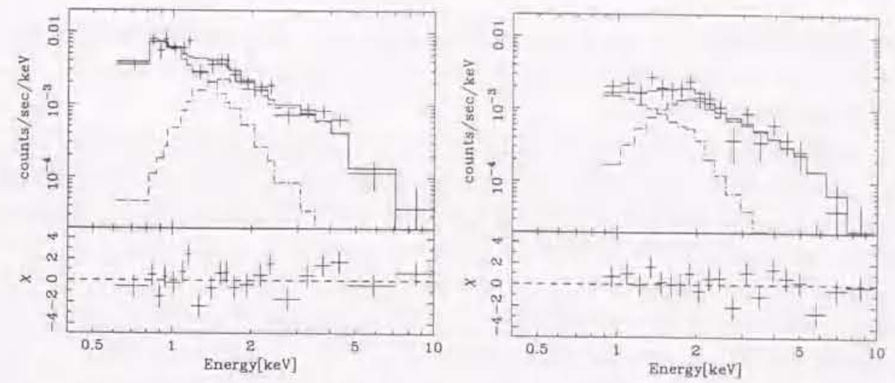

Figure 5.41: SIS (left) and GIS (left) spectra of NGC7217. Histogram represents the best fit R-S plus power-law model

X-ray spectra of NGC 4569 and NGC 7217 are represented by a two component model. The soft component is described by a thermal plasma model of $kT \sim 0.7$ keV. The X-ray to far infrared luminosity ratios L_X/L_{FIR} are 2.4×10^{-4} for both NGC 4569 and NGC 7217, and very similar to the typical value of starburst galaxies. Starburst galaxies generally show apparently weak iron L emission line features (Moran & Lehnert 1997, Ptak et al. 1997, Tsuru et al. 1997). Although we cannot make a stringent constraints on the iron abundance because of poor statistics, X-ray spectral shape is consistent with starburst galaxies.

The X-ray fluxes of the hard component are $\sim 3 \times 10^{-13}$ ergs s^{-1}cm^{-2} and $\sim 2 \times 10^{-13}$ ergs s^{-1}cm^{-2} for NGC 4569 and NGC 7217, respectively. Only upper limit of the X-ray flux $\sim 2 \times 10^{-13}$ ergs s^{-1}cm^{-2} is obtained for NGC 404. If X-rays above 2 keV are originated from an AGN, the X-ray to Hα luminosity ratio $L_X/L_{H\alpha}$ is expected to be similar to low luminosity AGNs discussed in §6.1. However observed $L_X/L_{H\alpha}$ values for these three galaxies are about an order of magnitude smaller than low luminosity AGNs and Seyfert 2 galaxies, where L_X is the luminosity in the 2–10 keV band and $L_{H\alpha}$ is the luminosity of the narrow component of the Hα emission line. Furthermore, X-ray binaries seem to make a significant contribution to the hard X-ray emission, since the X-ray to B-band luminosity ratios L_X/L_B are similar to normal galaxies. Actually the observed X-ray spectra of the hard component is consistent with superposition of low mass X-ray binaries, whose spectra can be approximated by thermal bremsstrahlung with temperature of several keV. If contribution from binaries is subtracted, $L_X/L_{H\alpha}$ for the nuclear component is much lower than the observed $L_X/L_{H\alpha}$. The small $L_X/L_{H\alpha}$ values

suggest two possibilities; one is that optical emission lines are generated by the energy source which emit less X-rays than AGNs, and another is that the AGN is obscured even at energies above 2 keV.

The X-ray spectra of the hard component in NGC 4569 and NGC 7217 are represented by a power-law with photon index of ~2.5 or thermal bremsstrahlung of several keV, and suffers from excess absorption of order of 10^{22} cm^{-2}. The X-ray spectral slope is consistent with super position of low mass X-ray binaries or starburst galaxies (Ptak et al. 1997, Tsuru et al. 1997, Moran & Lehnert 1997, Ohashi et al. 1990), but somewhat steeper than AGNs. Thus there is no clear indication of the presence of AGN in three galaxies analyzed here. We discuss the possible ionization sources in these LINER 2s.

1. Ionization by hot stars

X-ray detected LINER 2s NGC 4569 and NGC 7217 show soft thermal emission, probably due to starburst activity, and weak hard X-ray emission. Although NGC 404 is not detected in X-rays, the upper limits for L_X/L_{FIR} and L_X/L_B values are consistent with NGC 4569 and NGC 7217.

Starburst could produce LINER-like optical emission lines through shock heating in starburst driven winds (e.g. Heckman et al. 1990) or photoionization by very hot stars (Filippenko & Terlevich 1992, Shields 1992).

Recent UV observations with *HST* FOS of NGC 404 and NGC 4569 show UV spectra are dominated by hot stars (Maoz et al. 1998). Maoz et al. (1998) extrapolate the UV luminosity at 1300 A towards higher energies and estimate the expected Hα flux under Case B recombination with 100% covering factor, where they assume instantaneous burst of age 1 Myr with Salpeter initial-mass function with upper mass cut off of $120M_\odot$ or $30M_\odot$. They conclude that stellar populations probably provide enough ionizing photons to drive the observed optical emission line flux. If shock excitation plays an important role in ionizing LINER spectra, strong UV emission lines are expected. NGC 4569 shows no strong UV emission line and shock is not a dominant ionizing process at least in this object.

NGC 7217 is a UV dark object and UV emission is probably hidden by dust obscuration, as the observed large flux ratio Hα/Hβ = 6.83 indicates significant reddening (Barth et al. 1998). Therefore no spectral information in the UV is available and we cannot exclude the presence of enough number of hot stars to explain optical emission line luminosities.

2. Hidden AGN

Although the optical emission line flux can be probably explained by hot stars, it has not yet answered whether AGN is present or not. The X-rays from AGN does not contribute significantly to the observed X-ray flux even at energies above 2 keV as discussed above. Hence, if AGN is present, AGN should be obscured. In order to obscure X-ray emission of several keV, an equivalent hydrogen column density of the absorbing matter is necessary to exceed $\sim 10^{23}$ cm^{-2}. Then UV emission from the hidden AGN is completely blocked and only scattered UV emission would be expected. Actually, recent *HST* WFPC2 observations of Seyfert 2 galaxies show that UV emission from Seyfert 2 galaxies are fully explained by circum nuclear starforming regions and UV emission from the nuclei is barely detected (Colina et al. 1997). Therefore bright UV emission dominated by hot stars (NGC 404 and NGC 4569) and no detection in the UV (NGC 7217) do not exclude the possibility of the presence of hidden AGN at the LINER 2 nuclei.

There are two possibilities to reconcile observational data and the presence of a hidden AGN. In the case that X-ray flux above 2 keV is dominated by emission from X-ray binaries, it may possible that X-rays from obscured AGN emission contribute only above several keV. The low luminosity Seyfert 2 galaxy M51 (NGC 5194) is actually the case (§5.5.3; Terashima et al. 1998a). Alternatively, X-rays from the nucleus may completely blocked by the obscuring matter. Then we expect only scattered X-rays and the scattered fraction is typically less than several percent (Ueno 1995). In this case, the observed small $L_X/L_{H\alpha}$ can be explained, since narrow Hα is emitted from out side of the obscuring matter, and the observed X-ray luminosity L_X is only a small fraction of the intrinsic luminosity. In both cases, strong iron K emission with an equivalent width greater than several hundreds of eV is expected. Although the observed spectra show no indication of iron lines, we cannot set a physically meaningful upper limit because of limited photon statistics. The obtained upper limits for the equivalent width are $\sim 1.5 - -2$ keV for NGC 4569 and NGC 7217.

In summary, observed X-ray properties are consistent with starburst origin and UV data indicate that optical emission lines are probably explained by hot stars. X-ray emission from AGN does not dominates even at energies above 2 keV and we exclude the presence of 'type 1' AGN, while we cannot exclude the possibility of the presence of heavily obscured AGN.

5.8 Poststarburst LINERs NGC 4736 and NGC 5195

5.8.1 Introduction

Optical spectroscopic surveys have revealed low-level activity in the form of low ionization nuclear emission-line regions(LINERs) and they are usually considered to be due to AGN with low ionization parameters. Some LINERs show strong Balmer absorption lines as well as low ionization emission lines and make it difficult to measure Hα precisely. Such absorption features could lead us to misclassification to LINERs based on emissin line ratio such as [NII]/Hα. X-ray measurements are crucial to determine 'true' ionizing source including low luminosity AGNs, starburst driven winds, very hot stars and so on.

The deep Balmer absorption lines indicate presence of a number of A-type stars. The nuclei with these features would suggest they are in poststarburst phase. If this is the case, X-ray observation of this class is of quite importance for studying link between starburst and AGN. Furthermore X-ray measuremets of abundances of hot gas produced by galactic winds caused by starburst activity provide us information on chemical evolution of starburst galaxies.

Here we present X-ray results of NGC5195 and NGC4736 which are LINERs with deep Balmer absorption lines (Filippenko & Sargent 1985, Ho, Filippenko & Sargent 1995, Ho, Filippenko & Sargent (1997a), Yamada 1995 private communication, Taniguchi et al. 1996).

5.8.2 NGC 4736

The SIS images of NGC 4736 in the 0.5–2 keV and 2–10 keV band is consistent with the point spread function. A *ROSAT* PSPC image indicates the presence of weak extended component extended to 1' scale in raduis (Cui et al. 1997). we find no clear evidence of extended emission probably due to different band pass between two instuments (*ROSAT* PSPC has more sesitivity in the soft energy band). This would also suggest that extended emission has soft X-ray soectrum. Actually hot gas of kT $\sim$0.3 keV is suggested from *ROSAT* PSPC spectrum (Cui et al. 1997).

The SIS and GIS spectra of NGC 4736 are shown in Fig 5.42. The X-ray spectra are well fitted with a two-component model Raymond-Smith + power-law and the best fit spectral parameters are summarized in Table 5.4. The best fit photon index ($1.44^{+0.14}_{-0.16}$) is slightly flatter than typical AGNs. We also examined a model with different abundance between iron and alpha elements, where we fixed abundance of iron at 0.5 solar. Similar chi-square is obtained for this model. In this model, the best fit photon index is slightly

steepar than previous model: $1.57^{+0.45}_{-0.12}$.

A hint of iron K emission is seen. We add a narrow Gaussian at 6.4 keV or 6.7 keV to above models. An addition of a 6.7 keV Gaussain slightly improves chi-square ($\Delta\chi^2$=2.9) and an equivalent width of 340^{+380}_{-320} eV is obtained. This line emission is significant at only 90% confidence. A 6.4 keV line does not improves chi-square ($\Delta\chi^2$=0.5). If iron emission at 6.7 keV is real, the center energy is higher than 6.4 keV which is generally observed from Seyfet 1 galaxies.

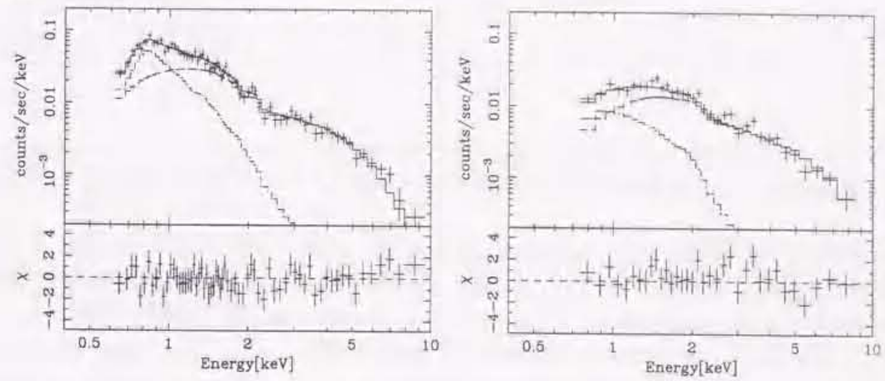

Figure 5.42: SIS (left) and GIS (left) spectra of NGC4736. The best fit Raymond-Smith + power-law model is shown.

5.8.3 NGC 5195

NGC 5195 is the companion galaxy of M51 (NGC 5194) and located at $\sim$4' from M51. Therfore we extracted X-ray spectra within 1.5' and 2' radii from the NGC 5195 nucleus. Although count rates are small (0.012 cts s^{-1} $1SIS^{-1}$ and 0.006 cts s^{-1} $1GIS^{-1}$), the X-ray spectra cannot be explained by a single power-law model. An acceptable fit is obtained with a Raymond-Smith + power-law model. The SIS and GIS spectra and the best fit model are shown in Fig 5.43.

Discussion

We detected bright X-ray source at the nucleus of NGC 4736. The X-ray specrum is slightly flatter than typical spectrum of Seyfert 1 galaxies and LINERs with broad Hα. As discussed in §6.1, the ratio $L_X/L_{H\alpha}$ is similar to other low luminosity AGNs and X-ray

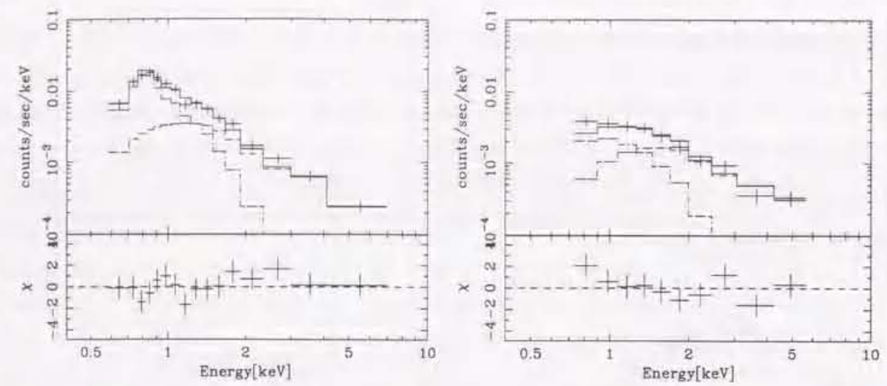

Figure 5.43: SIS (left) and GIS (left) spectra of NGC5195. The best fit Raymond-Smith + power-law model is shown.

emission is most likely to be dominated by emission from AGN. Only weak hint of iron emission is seen around ~ 6.7 keV and equivalent width is constrained to be 340^{+380}_{-320} eV. Iron emission line centered at 6.7 keV of equivalent width around ~300 eV are observed in the low luminosity Seyfert / LINER NGC 3031 (M81) (Ishisaki et al. 1996) and NGC 4579 (§5.4.2, Terashima et al. 1998b). If this iron emission is really present, it provides additional evidence for the AGN.

On the other hand, the X-ray spectrum of NGC 5195 is consistent with photon index of ~ 1.8 although the error are large. However smaller $L_X/L_{H\alpha}$ suggests small contribution of AGN to X-ray flux as is the case for LINER 2s discussed in §5.7. The small X-ray luminosity and X-ray spectrum is consistent with LMXBs origin distributed in the host galaxy.

Chapter 6

Discussion

6.1 Summary of Observational results

We observed twenty low luminosity Seyfert galaxies and LINERs with *ASCA* and detected X-ray emission from all of the galaxies but for one LINER (NGC 404). In this section, we briefly summarize the results.

6.1.1 Spectrum

The X-ray spectra of our sample galaxies are represented by a combination of a soft thermal emission and a hard component. Several objects (NGC 2273, NGC 3998, NGC 4203, NGC 4941, NGC 5033) show no signature of a soft thermal emission and require only a hard component.

A summary of the best fit parameters of the hard components is tabulated in Table 6.1. In many cases, the hard component can be modeled by a power-law modified by photo-electric absorption. The hard component of NGC 1052, NGC 2273, NGC 4565 and NGC 4941 show both heavily absorbed and less absorbed components and well represented by a partial covering model. The best fit parameters for iron K emission are also shown in Table 6.1 for objects from which iron emission is detected (NGC 1052, NGC 2273, NGC 3998, NGC 4579, NGC 4941, NGC 5033, NGC 5194).

The spectral fitting parameters for the soft components are shown in Table 6.2. The soft components are represented by a Raymond-Smith thermal plasma model of $kT \sim 0.5 - 1.0$ keV. The abundance is determined for objects with good statistics and typically less than sub solar. The thermal emission from NGC 3079, NGC 4450, NGC 4594, and NGC 5194 show weak iron L line complex compared and apparently small iron abundance compared to α elements is obtained.

Table 6.1: Summary of the spectral parameters for the hard component.

name	class	$N_{\rm H}$ [cm^{-2}]	photon index	Energy [keV]	width [eV]	EW [eV]	model
NGC 4579	S1.9/L1.9	0.04 ± 0.03	1.72 ± 0.05	$6.73^{+0.13}_{-0.12}$	$0.17^{+0.11}_{-0.12}$	490^{+180}_{-190}	PL+RS+GA
NGC 5033	S1.5	0.087 ± 0.017	1.72 ± 0.04	$6.40^{+0.08}_{-0.06}$	0(f)	290 ± 100	PL+GA
NGC 1667	S2	$0(< 0.16)$	$2.3^{+0.8}_{-0.4}$	—	—	—	PL
NGC 2273	S2	9.5 ± 1.6	$1.11^{+0.14}_{-0.41}$	$6.37^{+0.05}_{-0.06}$	0(f)	1400^{+500}_{-400}	PC+GA
		$0(< 0.034)$					
		(CF $0.77^{+0.05}_{-0.07}$)					
NGC 3079	S2	$1.8^{+1.7}_{-1.3}$	2.0 ± 0.7	—	—	—	PL+vRS
NGC 4565	S2	$0.65^{+0.11}_{-0.14}$	2.60 ± 0.32	—	—	—	PC+RS
		0.30 ± 0.07					
		(CF $0.65^{+0.11}_{-0.14}$)					
NGC 4941	S2	100^{+50}_{-30}	$1.50^{+0.58}_{-0.48}$	$6.33^{+0.07}_{-0.08}$	0(f)	760^{+410}_{-280}	PC+GA
		$0.18(< 0.56)$					
		(CF $0.962^{+0.023}_{-0.050}$)					
NGC 5194	S2	$2.6^{+1.3}_{-0.7}$	$1.69^{+0.35}_{-0.48}$	$6.41^{+0.08}_{-0.12}$	0(f)	910^{+410}_{-380}	PL+vRS+GA
NGC 1052	L1.9	$20.0^{+7.0}_{-8.3}$	$1.67^{+0.57}_{-0.40}$	6.35 ± 0.08	0(f)	180^{+80}_{-90}	PC+GA
		$2.5^{+2.7}_{-1.4}$					
		(CF $0.77^{+0.08}_{-0.10}$)					
NGC 3998	L1.9	0.088 ± 0.012	1.89 ± 0.03	$6.42^{+0.11}_{-0.20}$	0(f)	90 ± 70	PL+GA
NGC 4203	L1.9	$0.024(< 0.056)$	1.77 ± 0.08	—	—	—	PL
NGC 4438	L1.9	$1.4(< 5.3)$	$2.0^{+1.5}_{-1.0}$	—	—	—	PL+RS
NGC 4450	L1.9	$0(< 0.38)$	$1.64^{+0.30}_{-0.39}$	—	—	—	PL+vRS
NGC 4594	L2(1.9)	0.73 ± 0.29	1.89 ± 0.16	—	—	—	PL+vRS
NGC 5005	L1.9	$0.10(< 0.86)$	0.97 ± 0.37	—	—	—	PL+RS
NGC 404	L2						no detection
NGC 4569	T2	$2.4^{+1.5}_{-1.2}$	$2.7^{+0.9}_{-0.6}$	—	—	—	PL+RS
NGC 4736	L2	$0(< 0.88)$	$1.44^{+0.14}_{-0.16}$	—	—	—	PL+RS
NGC 5195	L2:	$1.9^{+2.0}_{-1.3}$	$2.0^{+0.9}_{-0.7}$	—	—	—	PL+RS
NGC 7217	L2	$1.5^{+1.6}_{-0.9}$	$2.4^{+0.8}_{-0.6}$	—	—	—	PL+RS

model : PL : power-law, PC : partially covered power-law, RS : Raymond-Smith, vRS : variable abundance Raymond-Smith, GA : Gaussaian

The center energies of iron emission lines are at the rest frame.

Table 6.2: Summary of the spectral parameters for the soft component.

name	class	kT [keV]	abundance [solar]	abundance (Fe) [solar]	model
NGC 4579	S1.9/L1.9	$0.90^{+0.11}_{-0.05}$	0.5(f)	—	PL+RS
NGC 5033	S1.5	—	—	—	PL+GA
NGC 1667	S2	—	—	—	PL
NGC 2273	S2	—	—	—	PL
NGC 3079	S2	$0.62^{+0.08}_{-0.15}$	0.5(f)	$0.048^{+0.026}_{-0.019}$	PL+vRS
NGC 4565	S2	$1.35^{+1.65}_{-0.42}$	$0.27(> 0.03)$	—	PC+RS
NGC 4941	S2	—	—	—	PC+GA
NGC 5194	S2	$0.61^{+0.04}_{-0.05}$	$0.14^{+0.05}_{-0.06}$	$0.041^{+0.013}_{-0.011}$	PL+vRS+GA
NGC 1052	L1.9	$1.0^{+2.2}_{-0.3}$	$0.04(< 0.10)$	—	PC+RS+GA
NGC 3998	L1.9	—	—	—	PL+GA
NGC 4203	L1.9	—	—	—	PL
NGC 4438	L1.9	$0.79^{+0.07}_{-0.15}$	0.1(f)	—	PL+RS
NGC 4450	L1.9	$0.66^{+0.19}_{-0.30}$	0.5(f)	$0.09(> 0.03)$	PL+vRS
NGC 4594	L2(1.9)	$0.62^{+0.08}_{-0.11}$	0.5(f)	$0.11^{+0.08}_{-0.03}$	PL+vRS
NGC 5005	L1.9	$0.76^{+0.07}_{-0.08}$	$0.06^{+0.09}_{-0.02}$		PL+RS
NGC 404	L2				no detection
NGC 4569	T2	$0.69^{+0.07}_{-0.09}$	$0.12^{+0.42}_{-0.064}$	—	PL+RS
NGC 4736	L2	$0.62^{+0.06}_{-0.07}$	$0.05^{+0.11}_{-0.02}$	—	PL+RS
NGC 5195	L2:	$0.61^{+0.07}_{-0.14}$	0.03 ± 0.02	—	PL+RS
NGC 7217	L2	$0.76^{+0.10}_{-0.12}$	0.1(f)	—	PL+RS

model : PL : power-law, PC : partially covered power-law, RS : Raymond-Smith, vRS : variable abundance Raymond-Smith, GA : Gaussaian

The center energies of iron emission lines are at the rest frame.

6.1.2 Image

We compared the SIS images in the 0.5–2 keV and 2–10 keV band with the point spread function (PSF). The X-ray images of NGC 3079, NGC 5005 and NGC 5194 (M51) is extended in the 2-10 keV band. For these objects, we also examined the X-ray images in the higher energy band. NGC 3079 in the 4–10 keV band and NGC 5194 in the 5–10 keV band are consistent with the PSF, while NGC 5005 in the 4–10 keV is still extended. All the other objects are consistent with point-like above 2 keV. In the soft energy band 0.5–2 keV, several sources are extended compared to the PSF. These are NGC 3079, NGC 4450, NGC 4569, NGC 4594, NGC 5005, NGC 5194.

6.1.3 Variability

We searched for variability of X-ray intensities using light curves binned to 5760 sec. We found significant variability within one day observation only from NGC 5033. Other objects indicate no signature of variability. We compare the fluxes obtained to previous X-ray observations in the next section.

6.2 Origin of X-ray emission

We detected hard X-ray emission with luminosities of $\sim 10^{39} - 10^{41}$ ergs s^{-1} from all the observed low luminosity Seyfert galaxies and LINERs but for NGC 404. Since normal galaxies also emit X-rays with luminosities of the order of $10^{39} - 10^{40}$ ergs s^{-1}, only the detection of hard X-rays does not provide evidence for the presence of AGN. We discuss the origin of X-ray emission above 2 keV based on X-ray properties (variability, images, iron emission lines) and correlation between X-ray and other wavelengths data.

6.2.1 X-ray evidence for AGN

Iron K emission line

Iron K fluorescence lines are generally detected from Seyfert galaxies. The fluorescent lines indicate the presence of cold matter and X-rays irradiating it. Thus detection of fluorescent iron emission is strong evidence for the active nucleus and the cold matter subtended to large solid angle viewed from the nucleus (type 1) and/or large column density along the line of sight (type 2). A fluorescent iron line is detected from NGC 5033 and its X-ray emission is obviously dominated by emission from an AGN as variability is also detected.

Strong fluorescent iron lines are present in the spectra of NGC 1052, NGC 2273, NGC 4941, and NGC 5194. Heavily absorbed continuum ($N_{\rm H} \sim 10^{23} - 10^{24}$ cm^{-2}) is also detected from NGC 1052, NGC 2273 and NGC 4941. These spectral features are reminiscent of Seyfert 2 galaxies with higher luminosities and these objects are considered to be low luminosity version of Seyfert 2s. Although NGC 5194 shows extended hard X-ray image in the 2–5 keV band, detection of a strong fluorescent iron line strongly suggest that presence of a hidden AGN (see subsection for M51).

In summary, fluorescent iron lines, which is strong evidence of the presence of an AGN, are detected from NGC 5033, NGC 1052, NGC 2273, NGC 4941, and NGC 5194 and they are most likely to be AGNs.

Variability

Detection of X-ray variability indicates that the X-ray flux is dominated by single or at most a few compact objects. Significant X-ray variability within one day observation is detected only from NGC 5033. Then we compared our *ASCA* fluxes with previous observations. Table 6.3 summarizes the X-ray fluxes of the current sample galaxies in the 2–10 keV range obtained by previous observations. Three galaxies NGC 1667, NGC 3998, and NGC 5194 (M51) are observed by the *Ginga* satellite. Their *ASCA* fluxes are smaller than the fluxes measured with *Ginga*. Such X-ray variability indicates the presence of a compact nucleus in these galaxies, although we cannot rule out the possibility that *Ginga* flux is contaminated by other X-ray sources because of large field of view ($1^\circ \times 2^\circ$) of the *Ginga* LAC. NGC 5033 is observed by EXOSAT/ME and the *ASCA* flux is about 15% smaller than that obtained with EXOSAT/ME. Since spectral shape of NGC 5033 is not constrained by EXOSAT/ME (Turner & Pounds 1989), flux estimation from EXOSAT data depends on assumed spectral shape. Furthermore, the uncertainty of the *ASCA* flux is about 10%. Therefore long term variability of NGC 5033 is not significant in currently available data in the 2–10 keV range.

In Table 6.4, we compared also the 0.5–2 keV fluxes with previous *ROSAT* observations. The fluxes, measured instruments (PSPC/HRI) and the energy range reported in the literatures are shown as well as *ASCA* measurements. We assumed the best fitting spectra of *ROSAT* PSPC to convert the energy range to 0.5–2 keV. For the HRI data, we assumed a photon index of 2.0 and the Galactic absorption. According to Table 6.4, some objects show flux difference of a factor of 2 between *ROSAT* and *ASCA* observations. However we should be cautious when we compare fluxes obtained with different instruments because of different energy responses, bandpass, and the best fit/assumed model spectra. Furthermore, the response matrix of the *ROSAT* PSPC detector is known to give

steeper spectral slope ($\Delta\Gamma \sim 0.5$) than other instruments such as *ASCA* and *BeppoSAX* (Iwasawa, Fabian, & Nandra 1998). This fact also introduce the uncertainty in estimating the soft X-ray flux using *ROSAT* data. In case of NGC 5194, the AGN is heavily obscured and the X-ray emission is dominated by extended hot gas and several point sources. Then drastic flux change cannot be expected. Nevertheless, a factor of 2 different soft X-ray fluxes is reported for NGC 5194 (M51). Therefore we estimate the uncertainty in the soft X-ray flux estimation is a factor of 2. Then the flux change of listed objects in Table 6.4 is not significant, but for NGC 5033. Note two *ROSAT* PSPC observations of NGC 5033 are analyzed in the same manner, and a factor of 6 flux increase seems to be real.

In summary, X-ray variability is detected from NGC 1667, NGC 3998, NGC 4579, NGC 5033, and NGC 5194, and they are most likely to contain a nuclear compact source.

Table 6.3: X-ray fluxes obtained with previous missions in the hard energy band

Name	F_X(2-10 keV) [10^{-12} ergs s^{-1}cm^{-2}]		Ref.	F_X(2-10 keV; ASCA) [10^{-12} ergs s^{-1}cm^{-2}]	ratio
NGC1667		Ginga		0.09	
NGC3998	15	Ginga	A90	8.1	0.537
NGC5033	4.7	Exosat/ME	T89	5.5	0.855
NGC5194	6.1	Ginga	M90	1.1	0.164

references : A90 : Awaki et al. 1990, T89 : Turner & Pounds 1989, M90 : Makishima et al. 1990

X-ray images and Contribution from X-ray binaries

The X-ray emission from normal spiral galaxies are primarily from superposition of discrete sources specifically low mass X-ray binaries (Makishima et al. 1989) and their spectra are approximated by thermal bremsstrahlung of several keV. The X-ray continua of the brightest objects NGC 3998 and NGC 5033 are power-law shape and cannot be fitted with a thermal bremsstrahlung model. The X-ray spectra of NGC 1052, NGC 2273, and NGC 4941 are heavily absorbed and indicate the presence of a compact X-ray sources surrounded by thick matter. Therefore, in these galaxies, discrete sources in the host galaxies negligible contribute to the overall X-ray emission. On the other hand, the hard component of the X-ray spectra from other objects are also fitted with a thermal bremsstrahlung model of several keV except for the objects with very hard spectra (NGC 4736 and NGC 5005). Therefore we cannot exclude the possibility of discrete source origin of the hard X-ray emission only from the spectral shape.

Table 6.4: X-ray fluxes obtained with previous missions in the soft energy band

Name	F_X		Ref.	F_X(0.5-2 keV)	F_X(0.5-2 keV; ASCA)	ratio
NGC3079	0.727	ROSAT PSPC 0.1-2.0 keV	R97	0.53	0.47	1.13
NGC4203	2.16	ROSAT PSPC 0.1-2.5 keV	B95	1.40	1.19	1.18
NGC4594	2.30	ROSAT HRI 0.1-2.4 keV	F97	1.61	1.22	1.32
NGC4736	1.78	ROSAT PSPC 0.1-2 keV	C97	1.54	1.32	1.17
NGC5005	0.840	ROSAT PSPC 0.1-2.0 keV	R97	0.60	0.43	1.42
NGC5033	2.13	ROSAT PSPC 0.1-3.0 keV	P96	0.91	2.44	0.37
	7.04	ROSAT HRI 0.2-2.2 keV	K95	4.90	2.44	2.01
	13.1	ROSAT PSPC 0.1-3.0 keV	P96	5.61	2.44	2.30
NGC5194	4.05	ROSAT PSPC 0.1-2.0 keV	R97	2.79	1.36	2.05
	4.45	ROSAT HRI 0.1-2.4 keV	E95	2.84	1.36	2.09
	1.72	ROSAT PSPC 0.2-2.2 keV	M95	1.36	1.36	1.00
NGC5195	0.65	ROSAT HRI 0.1-2.4 keV	E95	0.42	0.47	0.90

references : R97 : Read, Ponman, & Strickland 1997, B95 : Bregman, Hogg, & Roberts 1995, P96 : Polletta et al. 1996, K95 : Koratkar et al. 1995, F97 : Fabbiano & Juda 1997, C97 : Cui et al. 1997, M95 : Marston et al. 1995, E95 : Ehle et al. 1995

If discrete sources distributing over the host galaxy dominate the X-ray emission, the X-ray image is expected to be extended. The X-ray images above 2 keV of NGC 5005 and M51 (NGC 5194) are extended and discrete sources contribute to the hard X-ray emission significantly. The relatively nearby galaxies NGC 4203 (9.7 Mpc), NGC 4565 (9.7 Mpc), and NGC 4736 (4.3 Mpc) in our sample show a point like X-ray source at the nucleus. Therefore these objects are considered to be dominated by the central point source. NGC 4594 (20.0 Mpc) is observed with *ROSAT* HRI and several point sources and diffuse emission is are detected (Fabbiano & Juda 1997). They estimate that the nuclear source emits $\sim 50\%$ of total X-ray flux within the PSF of the *ROSAT* PSPC even in the soft X-ray band. Since *ASCA* image is extended below 2 keV and point-like above 2 keV, and and probably contribution from diffuse component is small in the hard X-ray band.

In summary, NGC 1052, NGC 2273, NGC 3998, NGC 4203, NGC 4565, NGC 4594, NGC 4736, NGC 4941 and NGC 5033 are dominated by a nuclear source, while discrete sources significantly contribute to X-ray emission from NGC 5005 and NGC 5194.

6.2.2 X-ray emission from hot gas

Most of the sample galaxies exhibit the soft component represented by a thin thermal plasma model of kT ~0.5–1 keV. In this section, we discuss the origin of the thermal component based on X-ray morphology, temperature, abundance, and luminosities.

The presence of hot gas with temperature of kT ~0.5–1 keV is known in elliptical galaxies, starburst galaxies, and some normal spiral galaxies. Several objects (NGC 3079, NGC 4565, NGC 4594, NGC5194) indicate that their iron abundance is lower than alpha elements. Such hot gas component with lower iron abundance is observed in starburst galaxies (Tsuru et al. 1998, Moran & Lehnert 1996, Ptak et al. 1996) and giant HII regions (Ptak 1997), while the metal abundance of hot gaseous component of elliptical galaxies is consistent with the solar ratio (Awaki et al. 1994, Matsushita et al. 1997). Therefore contribution from starformation activity to the hot gas is strongly suggested for at least these objects. Although the metal abundance in hot gas of other objects is consistent with the solar ratio, the possibility that iron is less abundant cannot be ruled out because of limited photon statistics. If the hot gas is originated from starburst activity, the luminosity of the hot gas is expected to be proportional to the far infrared luminosity, which reflects the power of starburst activity, as in starburst galaxies. Fig 6.1 shows the correlation between the X-ray luminosity in 0.5–4 keV of the Raymond-Smith component in the spectral fitting and the fir infrared luminosity. We calculated the far infrared flux from IRAS measurements of fluxes at 60 μm and 100 μm as $F_{\rm FIR} = 1.26 \times 10^{-11}(2.58F_{60\mu m} + F_{100\mu m})$[ergs s^{-1}], where $F_{60\mu m}$ and $F_{100\mu m}$ are measured in unit of Jy. In the same figure, data points for starburst galaxies taken from literatures are also shown.

The X-ray luminosities of hot gas in starburst galaxies are roughly proportional to far infrared luminosities and the X-ray to far infrared luminosity ratio $L_{\rm X}/L_{\rm FIR}$ is around 10^{-4} (Fig 6.1, see also Heckman et al. 1990). The ratio $L_{\rm X}/L_{\rm FIR}$ for most of the present sample galaxies are similar to starburst galaxies and their hot gas are most likely to be produced through starburst activity.

The $L_{\rm X}/L_{\rm FIR}$ values for NGC 4594 and NGC 1052 are higher than other objects and starburst galaxies. The X-ray image of NGC 4594 in the 0.5–2 keV band is clearly extended to the galaxy scale or more and the X-ray distribution seems to be spherical. NGC 4594 is a Sa galaxy with a large buldge and an X-ray gas halo similar to elliptical galaxies may be present. Since NGC 1052 is an E3/S0 galaxy, such a gaseous halo is a possible origin of the hot gas. Actually, for both NGC 4594 and NGC 1052, observed kT is consistent with the relation between kT and the stellar velocity dispersion (σ) for

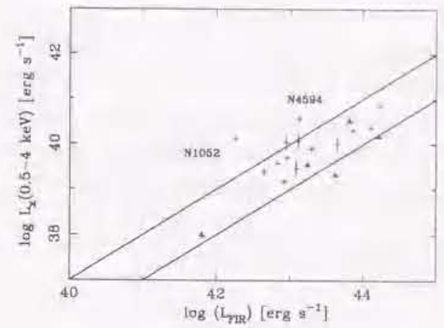

Figure 6.1: Far infrared luminosity vs X-ray (0.5–4 keV) luminosity for the soft thermal component. Upper and lower solid lines correspond to $L_{\rm X}/L_{\rm FIR}$=10^{-3} and $L_{\rm X}/L_{\rm FIR}$=10^{-4}, respectively. Crosses represent the galaxies in the present sample and triangles are starburst galaxies compiled from literatures.

elliptical galaxies (Davis & White 1996).

6.3 Ionization mechanism of LINERs

6.3.1 X-ray to Hα luminosity ratio

If X-ray emission is dominated by an AGN and optical emission lines are due to photoionization by radiation from an AGN, the X-ray luminosity is expected to be proportional to the optical emission line luminosity. Actually X-ray luminosities in 2–10 keV and luminosities of broad Hα positively correlate well for Seyfert 1 galaxies and quasars (e.g. Ward et al. 1988). *ROSAT* observations of low luminosity Seyfert galaxies show this correlation extends to lower luminosity though number of sample galaxies are rather limited (Koratkar et al. 1995).

If the origin of LINERs is photoionization, intensity of optical emission lines are expected to be proportional to number of ionizing photons. Among optical emission lines, strength of forbidden lines such as [NII]$\lambda\lambda$6548, 6583 and [SII]$\lambda\lambda$6716, 6731 depends on other parameters e.g. electron density. Therefore Hydrogen recombination lines are more straight forward to compare with X-ray luminosities and to study ionization mechanisms. Assuming case B recombination (Osterbrock 1989), expected number of Balmer photons can be calculated from number of ionizing photon number. Therefore we compare the

observed X-ray luminosity and luminosity of Hydrogen recombination line. Since both narrow and broad Hα fluxes are available in literatures (Ho et al. 1997a, b), and Hα is less affected by extinction than Hβ, we use Hα flux for the following analysis.

We also included the *ASCA* results taken from literature to obtain more galaxy samples and compare with our galaxy samples; NGC 1097 (Iyomoto et al. 1996), NGC 1365 and NGC 1386 (Iyomoto et al. 1997), NGC 3031 (M81; Ishisaki et al. 1997), NGC 3147 (Ptak et al. 1996), NGC 4258 (Makishima et al. 1994). All of these objects are low luminosity Seyfert galaxies and X-ray emission is considered to be dominated by AGN.

Table 6.5: X-ray spectral fitting results of LLAGNs taken from literature

name	distance	class	intrinsic luminosity	photon index	$N_{\rm H}$	Fe center energy	EW
	[Mpc]		[10^{40} ergs s^{-1}]		[10^{22} cm^{-2}]	[keV]	[eV]
NGC1365	16.9	S1.5	3.2	$0.8^{+0.7}_{-0.2}$	$0(<3.0)$	$6.57^{+0.10}_{-0.06}$	2100^{+2100}_{-300}
NGC1386	16.9	S2	2.2	$1.6^{+1.9}_{-1.2}$	28^{+27}_{-26}	$6.53^{+0.05}_{-0.06}$	1600^{+7900}_{-1200}
NGC3031	1.4	S1.5	0.3	1.85 ± 0.04	1	6.6–6.7	200–300
NGC3147	40.9	S2	50	1.80 ± 0.09	$0.015(<0.043)$	$6.44^{+0.36}_{-0.14}$	490^{+310}_{-290}
NGC4258	6.8	S1.9	3.6	1.78 ± 0.29	15 ± 2	6.5 ± 0.2	250 ± 100

We show the $L_{\rm X} - L_{\rm H\alpha}$ plot for the low luminosity Seyfert 1s and LINER 1s along with Seyfert 1 / quasars sample by Ward et al. (1988) in Fig 6.2. Seyfert galaxies and LINER 1s (LINERs with broad Hα) are probable candidates of low luminosity AGNs. LINER 2s are discussed later. As the low luminosity Seyfert 1s and LINER 1s in our sample are intermediate types, i.e. type 1.5 / 1.8 / 1.9, luminosities of both broad and narrow Hα are available. Hence we plot the broad, narrow, and total Hα luminosities. The data points locate at the extension of the correlation for Seyfert / quasars, but somewhat scattered. This may be caused by obscuration of the broad line regions.

Then we plot the X-ray and narrow Hα luminosities of the low luminosity Seyfert 1s and LINER 1s. For luminous Seyferts / quasars, broad Hα dominates and narrow Hα measurements are often difficult. Therefore we use narrow Hα luminosities of Seyfert 2 galaxies (Mulchaey et al. 1994 and references therein). Fig 6.3 presents the $L_{\rm X} - L_{\rm H\alpha}$ plot using narrow Hα lines. The $L_{\rm X} - L_{\rm H\alpha}$ correlation is well extends to lower luminosities. Few objects (NGC 4438) would be X-ray faint compared to the correlation. Scatter of one order of magnitude is seen for both luminous and low luminosity sample. One reason is variability; ionizing continuum (UV–X-ray) shows rapid variability of a time scale of

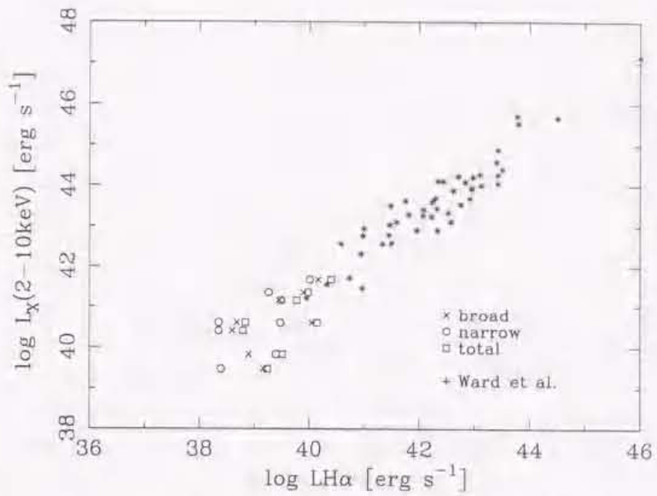

Figure 6.2: $L_{\rm H\alpha}$–$L_{\rm X}$ plot for low luminosity Seyfert 1 galaxies, LINER 1s, and Seyfert / quasar sample by Ward et al. (1988). Broad, narrow, and total Hα luminosities are plotted for low luminosity Seyfert 1 galaxies and LINER 1s. The Hα luminosities taken from Ward et al. (1988) are for broad Hα

a day or less, while the narrow emission line intensity is not vary in such a time scale since narrow line regions are located far from the nucleus (>10 pc). In Fig 6.3 Seyfert 2 galaxies with NGC number are heavily obscured AGN and only scattered radiation is observed even in X-rays. Then they are more than one order of magnitude X-ray faint compared to the correlation. We further discuss the $L_{\rm X}$ / $L_{\rm H\alpha}$ value quantitatively in the next section.

Secondary, we present the same plot for LINER 2s in Fig 6.4. Among LINER 2s, NGC 4736 is on the correlation. Note that both X-ray and Hα luminosity of NGC 4736 are almost same as the Seyfert 1.5 / LINER 1.5 galaxy M81. On the other hand, other LINER 2s NGC 404, NGC 4569, NGC 7217 are X-ray faint compared to the $L_{\rm H\alpha}$–$L_{\rm X}$ relation. These X-ray weakness suggest that optical emission lines are ionized by other mechanism rather than photoionization by the central AGN and/or that the AGN is heavily obscured. Actually, as discussed in the LINER 2s subsection, optical emission lines are most likely to be ionized by primarily hot stars for NGC 404 and NGC 4569.

For comparison, we also compiled starburst galaxies for which measurements of Hα and

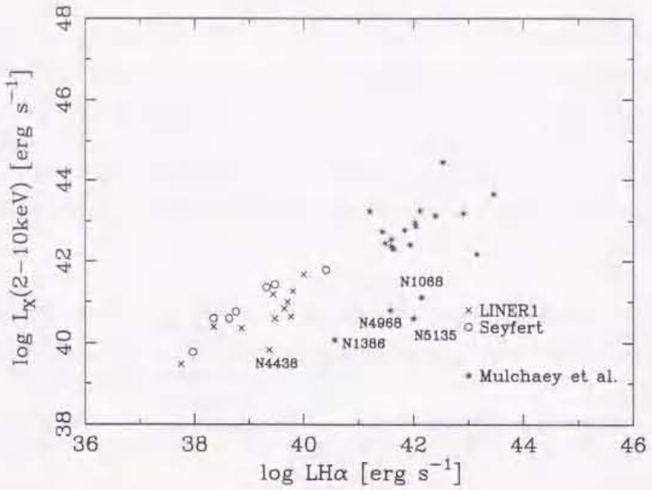

Figure 6.3: $L_{H\alpha}$–L_X plot for low luminosity Seyfert 1 galaxies, LINER 1s, and Seyfert 2 sample by Mulchaey et al. (1994). Narrow Hα luminosities are plotted.

2–10 keV luminosity are available. Except for NGC 1569 and NGC 4449, Hα luminosities are estimated from observed Brγ luminosities assuming Case B recombination ($T = 10^4$ K). These starburst galaxies are also plotted in Fig 6.4 and it is obvious that starburst galaxies are 1/10 – 1/100 X-ray faint at a given Hα luminosity. Small $L_X/L_{H\alpha}$ for starburst galaxies compared to Seyfert galaxies are also reported in Pérez-olea & Colina (1996) using soft X-ray luminosity in the 0.1–2.4 keV band.

In starburst galaxies, correlation between X-ray and Hα luminosities are loose and scatter is large. This is probably due to the heterogeneous origin of the hard X-ray emission in starburst galaxies ; X-ray binaries, inverse Compton scattering of far-infrared photons by energetic electrons, hot gas produced by collective supernova explosions. Then X-ray luminosity reflects the power of the starburst indirectly.

$L_X/L_{H\alpha}$ of LINER 2s and NGC 4438 are $\sim 1/10$ of those of low luminosity Seyferts and LINER1 s, and they are within large scatter of starburst galaxies or slightly higher than starburst galaxy. Thus 2–10 keV X-ray luminosities of LINER 2s and NGC 4438 are consistent with starburst origin, although small contribution from other origin may also present.

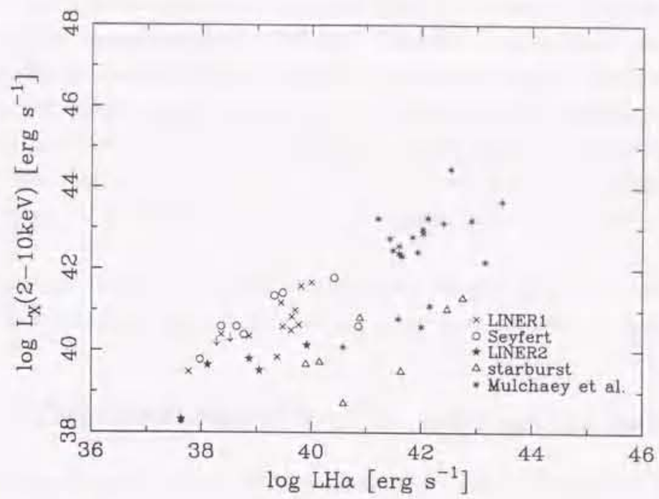

Figure 6.4: $L_{H\alpha}$–L_X plot for low luminosity Seyfert 1 galaxies, LINER 1s, LINER 2s and Seyfert 2 sample by Mulchaey et al. (1994). Narrow Hα luminosities are plotted. Starburst galaxies are also plotted for comparison.

6.3.2 Ionizing photons

Most of the LINER 1s show L_X – $L_{H\alpha}$ correlation as in luminous Seyfert galaxies. This correlation strongly suggests that optical emission lines in LINER 1s are photoionized by low luminosity AGNs with X-ray luminosities of $10^{39} - 10^{41}$ ergs s^{-1}.

We examine whether L_X luminosities are large enough or not to explain observed Hα luminosities. We estimate the ionizing photon number

$$Q = \int_{\nu_0}^{\infty} \frac{L_\nu}{h\nu} d\nu,$$

where ν_0 is the frequency of the Lyman edge, by extrapolating observed X-ray luminosity at 2 keV under assumption of the spectral shape of the ionizing continuum of $L_\nu \propto \nu^{-1}$. This spectral slope seems to be adequate to LINER 1s, as is shown in the next section. Then we compare the number of ionizing photon Q and Hα photon $N_{H\alpha}$. If we assume Case B recombination and 100% covering fraction, Q / $N_{H\alpha} = 2.2$ is expected (Osterbrock 1989). For low luminosity Seyfert galaxies and LINER 1s, Q / $N_{H\alpha}$ values are greater than 2.2. This means X-ray luminosity is enough to drive Hα luminosity. On the other hand, for the lowest $L_X/L_{H\alpha}$ object NGC 4569, Q / $N_{H\alpha}$ is calculated to be 1.3, which

means that X-ray photon number is in deficit to explain Hα even if we assume all of the X-ray flux goes into ionization. NGC 5195 has also low $L_X/L_{H\alpha}$ and Q / $N_{H\alpha}$ of 2.8. Since our estimation is under extreme condition (i.e. 100% covering fraction and all of ionizing photons are used to photoionize the narrow line regions), presumably this Q / $N_{H\alpha}$ is not enough to explain all Hα luminosity. Therefore, for these objects (NGC 4569 and NGC 5195), it is most probable that there is other ionization source rather than AGNs or that AGN is heavily obscured even at energies above 2 keV. Actually the presence of hot stars as an ionizing source is suggested for NGC 4569 from the UV spectrum (Maoz et al. 1998).

Such variety in $L_X/L_{H\alpha}$ suggest heterogeneous origin of LINERs: photoionization by low luminosity AGNs, photoionization by hot stars, and possibly starburst driven winds.

6.4 X-ray properties of low luminosity AGNs

In this section, we summarize the low luminosity AGN (LLAGN) sample and discuss their X-ray properties.

We use low luminosity Seyfert galaxies and also LINERs which satisfy following criteria as low luminosity AGN; X-ray image is point-like in X-rays above 2 keV and $L_X/L_{H\alpha}$ is similar to low luminosity Seyfert galaxies. However, the low luminosity Seyfert 2 galaxy NGC 4565 and NGC 5194 (M51) are excluded because of following reasons. Since NGC 4565 is dominated by the off nuclear source and we cannot measure the AGN spectrum, we utilized only the X-ray flux data of NGC 4565. NGC 5194 is dominated by discrete sources distributing over the host galaxy, and again we cannot measure the AGN spectrum.

The LLAGN sample consists of NGC 1052, NGC 2273, NGC 3998, NGC 4203, NGC 4450, NGC 4736, NGC 4579, NGC 4594, NGC 4941, NGC 5033. We also compiled *ASCA* results of low luminosity Seyferts and LINERs taken from literature; NGC 1097, NGC 1365, NGC 1386, NGC 3031 (M81), NGC 3147, and NGC 4258.

6.4.1 Spectral shape

Absorption column density

The X-ray spectra of observed galaxies are generally explained by the 'canonical model' Raymond-Smith thermal plasma of kT =0.5–1 keV + hard component. The hard component, which is dominated by LLAGN, is well represented by a power-law with some absorption.

The intrinsic absorption column densities are widely distributed from $N_H \sim 10^{20}$ cm^{-2} to $\sim 10^{24}$ cm^{-2}. Fig 6.5 shows the distribution of the hydrogen column densities N_H. Small and large intrinsic absorption are reminiscent of Seyfert 1s and Seyfert 2s, respectively. Then we classify our sample galaxies into two classes: type 1 (small absorption) and type 2 (large absorption). Here we define objects with $N_H < 10^{22}$ cm^{-2} as type 1 LLAGN, and objects with $N_H > 10^{22.5}$ cm^{-2} as type 2 LLAGN. Note that distribution in Fig 6.5 does not reflects the true number ratio of type 1 and type 2 since our sample are not complete.

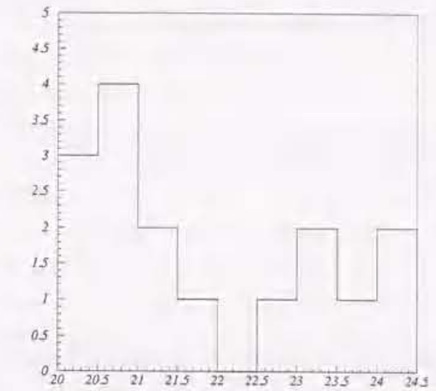

Figure 6.5: Histogram of log N_H for low luminosity AGNs

Continuum slope

We compare the continuum slope of LLAGNs with luminous Seyfert galaxies. Fig 6.6 shows luminosity dependence of photon indices for type 1 LLAGNs and Seyfert 1 galaxies taken from Nandra et al. (1997b). The photon indices of type 1 LLAGNs are quite similar to higher luminosity Seyfert 1s. The spectral slope of Seyfert 2s are known to be slightly flatter than Seyfert 1 galaxies (e.g. Awaki et al. 1991). For type 2 LLAGNs, the errors of photon indices are large and differences of photon indices between type 2 LLAGNs and luminous Seyfert 1/2 cannot be clearly recognized.

Thus spectral slope in LLAGNs are quite similar to luminous Seyfert galaxies. As shown in following subsections, LLAGNs are suggested to emit at very low Eddington ratio $L/L_{Eddington}$. Even under such extreme conditions, the spectral slope remains the same.

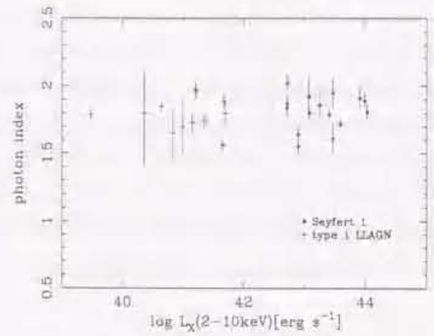

Figure 6.6: Luminosity dependence of photon indices of type 1 AGNs

Iron emission line

Type 2 object

In luminous Seyfert 2 galaxies, strong iron K emission is generally detected and the line center energy is consistent with 6.4 keV (e.g. Turner et al. 1997a). Iron emission with the line center energy higher than 6.4 keV is also often observed (e.g. Turner et al. 1997b). These strong emission lines are due to transmission through cold matter in the line of sight, reflection from cold matter out of line of sight, and ionized scatterer located above the opening part of the putative torus (Turner et al. 1997b).

We detected iron emission lines from all the LLAGNs with large intrinsic absorption. The line center energy is consistent with 6.4 keV but for two galaxies NGC 1365 and NGC 1386 (Iyomoto et al. 1997).

The equivalent width of iron K emission at 6.4 keV in NGC 1052, NGC 4258, and NGC 4941 are consistent with expected from transmission through observed column density. On the other hand, the equivalent width of the 6.4 keV line in NGC 2273 (EW=$1.4^{+0.5}_{-0.4}$ keV) is rather large compared to the expected equivalent width in the transmission case. Possible reasons for such large equivalent width are (1)significant contribution from reflection and/or (2)time variability (see subsection NGC 2273).

The strong line emission dominated by highly ionized iron in NGC 1365 and NGC 1386 would be explained by geometrical configuration. If we are seeing the obscuring matter in an almost edge on geometry, contribution of a reflection component from the inner surface of the obscuring matter becomes small, and scattered component dominates

the iron emission. The equivalent widths in NGC 1365 and NGC 1386 are consistent with the scattering model calculations by Band et al. (1990).

Type 1 object

We detected iron K emission from only a few type 1 LLAGNs; NGC 4579, NGC 5033. A detection of iron K emission from NGC 3031 (M81) is reported by Ishisaki et al. (1996) and Serlemitsos et al. (1996). From NGC 3998, only marginal iron K emission is detected. For LLAGNs except for these objects, photon statistics are limited to study iron emission lines. From some bright objects, upper limits of a equivalent width of narrow Gaussian line at 6.4 keV and 6.7 keV are typically 200–300 eV.

Since almost all the type 1 LLAGNs have very similar X-ray characteristics (spectral slope, intrinsic absorption, no short time scale variability), we summed up X-ray spectra of relatively bright objects which have no significant iron lines to obtain the composite spectrum with better photon statistics. We added the spectrum from four objects NGC1097, NGC3998, NGC4450, and NGC4594 (Fig 6.7).

We fitted the composite spectra in 2–10keV band with power-law model, since most of the *ASCA* spectra of LINERs indicate thermal emission from a hot gas of $kT \sim 0.5$ keV which is negligible in the energies above 2keV. An iron emission line is *not* detected from this composite spectrum. An upper limit of an equivalent width is $\sim$ 100 eV for narrow line at 6.4 keV or 6.7 keV. Our data cannot set a limit to the Compton reflection component. Obtained upper limit of the equivalent width 100 eV is smaller than the typical value of Seyfert 1s (100–200 eV; Nandra et al. 1997b).

Optically thick disk

The iron emission line in NGC 5033 is consistent with fluorescence from cold iron, which are usually observed from Seyfert 1 galaxies. On the other hand, NGC 4579 shows iron K emission at 6.7 keV with an equivalent width of $\sim$ 500 eV. The broad iron line is detected from M81 and the center energy, width, and equivalent width of the iron line from M81 are $\sim$ 6.6 keV, $\sim$ 200 eV, and $\sim$300 eV, respectively (Ishisaki et al. 1996, Serlemitsos et al. 1996).

If the optically thick accretion disk is present in LLAGNs as in Seyfert galaxies, difference of ionization states of iron line emitter would explain iron lines from LLAGNs. The line energy is consistent with He-like iron for M81 and NGC4579. A large equivalent width can be also explained by highly ionized species which have larger effective fluorescent yield. For FeXVII–FeXXIII, resonant trapping by the next ionized species destroy

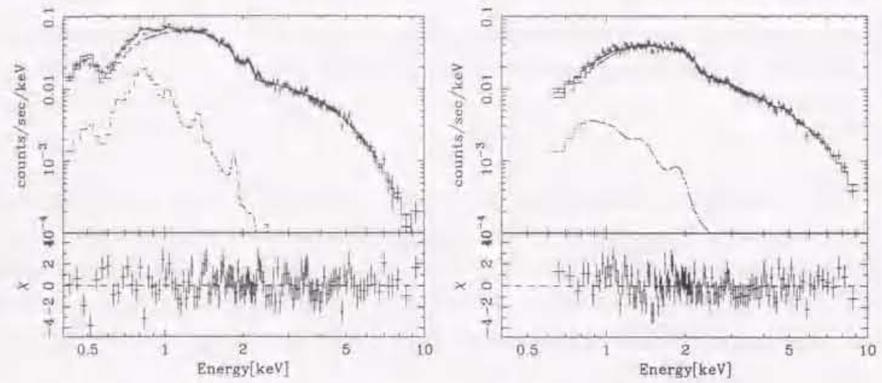

Figure 6.7: Composite X-ray spectra of LINERs. NGC 1097, 3998, 4450, and 4594 are added. left: SIS, right: GIS

the fluorescent photons (e.g. Zycki & Czerny 1994, Ross & Fabian 1993). When the ionization state of an iron lines are in this range, an iron emission is suppressed. Therefore a 6.4 keV line from NGC5033, weak iron line from the averaged spectrum, and 6.7 keV line from NGC4579 can be explained by ionization state of an iron emitter. Weak or no iron line is also explained if matter around the nucleus is fully ionized. A possible problem with this interpretation is to maintain high ionization parameter under low luminosity (see subsection of NGC 4579).

Advection dominated accretion flow

Alternatively, it is also possible that LLAGNs have no standard accretion disk. An advection dominated accretion flow (ADAF) is proposed for an LLAGNs emitting at very low Eddington ratio (e.g. NGC4258, Lasota et al. 1996). In an ADAF, accreting matter is heated up to very high temperature ($T_i \sim 10^{12}$K, $T_e \sim 10^9$K). Therefore iron atoms are fully ionized and no iron emission is expected. This accretion model naturally explain the upper limit for an iron line equivalent width for the averaged spectrum of LLAGNs. Actually, super massive black hole is suggested to be present in NGC4594 ($M \sim 1 \times 10^9 M_\odot$; Kormendy et al. 1996) and the Eddington ratio is estimated to be $\sim 10^{-6}$. Such an extremely low Eddington ratio is compatible with an ADAF.

Detection of an iron line indicates the presence of matter, which is not fully ionized, surrounding a large solid angle viewed from the light source. Therefore iron lines from NGC5033 and NGC4579 cannot be explained by ADAF. An optically thick disk probably

present in LLAGNs, from which an iron line is detected.

6.4.2 UV – X-ray spectral slope and blue bump

We calculated continuum slope between optical to X-ray. In usual AGNs, there exists so-called 'blue bump' in the UV band. Therefore the spectral slope between UV and X-ray reflects the strength of the UV bump relative to the power-law continuum. We compiled UV luminosity at 2300 A from *HST* FOC and WFPC2 observations (Maoz et al. 1995, Maoz 1996, Barth et al. 1996b, Barth et al. 1998) for type 1 LLAGNs. We use monochromatic X-ray flux at 2 keV and define UV – X-ray spectral slope as

$$\alpha_{oX} = -\log \frac{f_X/f_o}{\lambda_X/\lambda_o}$$

.

The α_{oX} values of LLAGNs distribute around ~ 1.0. This value is lower than typical values (1.2–1.4) for luminous Seyfert galaxies and quasars (Elvis et al. 1995, Bechtold et al. 1994, Mushotzky 1993, Mushotzky and Wandel 1992,). Recent UV observations around 1300 A of NGC 3031, NGC 4579, and NGC 4594 with *HST* FOS suggest the possibility that hot stars contribute to the UV emission to significant amount. Hence α_{oX} values obtained here could be only an upper limit. Therefore we conclude that LLAGNs have small α_{oX} than higher luminosity AGNs. This means that big UV bump generally observed in luminous AGNs is absent in this class of objects.

One possible reason for the absence of big UV bump is low temperature of the accretion disk. If energy extraction efficiency η in LLAGNs are same as higher luminosity objects, very low luminosity means that mass accretion rate $\dot{m}$ is very small, where output luminosity is denoted as $L = \eta \dot{m} c^2$. According to the standard accretion disk (Shakura & Sunyaev 1973), the effective temperature $T_e(r)$ is proportional to $\dot{m}^{1/4}$ at radius large enough compared to the radius of the inner boundary of the accretion disk. If the mass accretion rate in LLAGNs is 1/1000 of those of luminous AGNs, $T_e(r)$ becomes 1/5.6. Then the peak wavelength of the UV bump shift to the near UV – optical band. In these wavelengths, star light dominates the emission from weak AGN and we cannot observe the UV bump. Alternatively, if optically thick accretion disk is absent, strong UV emission from the accretion disk will disappear. For example, an advection dominated accretion flow (ADAF) model predicts no UV bump (e.g. Lasota et al. 1995). Again the ADAF model is not appropriate for the objects from which iron emission is detected; NGC 3031 (M81) and NGC 4579.

name	X-ray flux[a] [10^{-13} ergs s^{-1}cm^{-2}keV^{-1}]	UV flux[b] [10^{-15}ergs s^{-1}cm^{-2}A^{-1}]	α_{ox}	UV reference
NGC 3031 (M81)			0.86	H96
NGC 4203	5.3	0.21	1.14	B98
NGC 4579 (M58)	10		0.92	B96
NGC 4736	4.3	0.43	0.98	M96
NGC 4594 (M104)	6.7	0.12	1.28	M98

Table 6.6: UV–X-ray continuum slope α_{ox}

(a)monochromatic flux at 2 keV, (b)monochromatic flux at 2300 A, references : H96: Ho, Filippenko & Sargent 1996; B96 Barth et al. 1996; M96 Maoz 1996; M98 Maoz et al. 1998

6.4.3 X-ray to Hα luminosity ratio

The correlation between X-ray and Hα luminosity extends to low luminosity. However X-ray to Hα luminosity ratio $L_X/L_{H\alpha}$ is larger for low luminosity objects as clearly seen in Fig 6.8 which shows histograms of $\log L_X/L_{H\alpha}$ for our LLAGNs sample and Seyfert 2 sample of Mulchaey et al. (1994). The Kolmogorov-Smirnov test indicates that distributions are different at the 98.5% confidence level (P_{KS}=0.015).

LLAGNs indicate weak UV emission relative to X-rays in at least objects discussed above. Then number of ionizing photons are smaller at given X-ray luminosity. Therefore in order to explain a given Hα, LLAGNs should be more X-ray luminous than luminous Seyfert galaxies. Assuming ionizing continuum shape of $L_\nu \propto \nu^{-\alpha}$, we calculated the ionizing photon number. α=0.9 provides about 5.4 times more ionizing photons than α=1.3. This agrees with the difference between two histograms ($\sim 10^{0.75} = 5.6$) in Fig 6.8.

6.4.4 Variability

Seyfert 1 galaxies with lower luminosity show larger amplitude and more rapid variability than higher luminosity objects. However type 1 LLAGNs indicate no time variability within one day except for NGC 3031 and NGC 5033, and longer time scale seems to be common. A variability time scale provides upper limit of the size of the X-ray emitting region and longer time scale would suggest the presence of the large central engine, i.e. large central black hole mass.

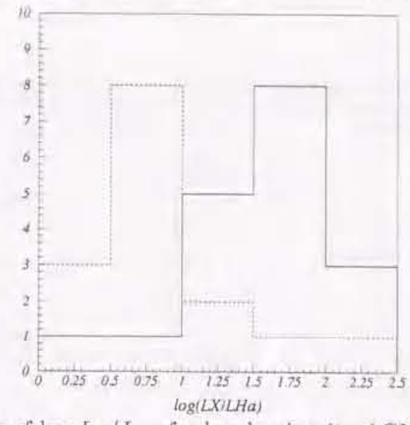

Figure 6.8: Histogram of log $L_X/L_{H\alpha}$ for low luminosity AGNs (solid line) and Seyfert 2 sample of Mulchaey et al. 1994. (dotted line)

6.4.5 Eddington ratio

If a blackhole mass is large (comparable or greater than that of luminous AGNs) as is inferred by slower time variability , the Eddington ratio $L/L_{\rm Eddigton}$ becomes extremely low for LLAGNs because of their low luminosities, where Eddington luminosity is

$$L_E = \frac{4\pi c G m_H M}{\sigma_T} = 1.3 \times 10^{38} \frac{M}{M_\odot} [\mathrm{ergs/s}].$$

The large mass is also suggested for blackholes at the center of nearby relatively quiescent galaxies (e.g. Kormendy & Richstone 1995). Here we compare observed X-ray luminosities and inferred blackhole mass, and calculate the Eddington ratio. The blackhole mass taken from literature and the calculated Eddington ratio are summarized in Table 6.7. The blackhole mass is estimated from kinematics around the nucleus measured by water vapor maser for NGC 4258 (Miyoshi et al. 1995) and measured by optical emission lines for NGC 4594 (Kormendy et al. 1996), and the ionization parameters and line width of UV broad emission lines for NGC 3031 (Ho et al. 1995) and NGC 4579 (Barth et al. 1996a).

Obtained Eddington ratios are very small and at most $\sim 10^{-4}$. Particularly, the Eddington ratio of NGC 4594 is extremely low; $\sim 10^{-6}$. If we apply bolometric correction of one order, this value becomes $\sim 10^{-3}$. Thus LLAGNs are suggested to emit at very low Eddington ratio.

Table 6.7: Summary of the central blackhole mass, Eddington ratio L_X/L_{Edd}

name	BH mass	X-ray luminosity [ergs s^{-1}]	L_X/L_{Edd}	reference
NGC 3031 (M81)	$(0.7-3)\times10^6 M_\odot$	2×10^{40}	$\sim1\times10^{-4}$	1
NGC 4258 (M106)	$3.6\times10^7 M_\odot$	4×10^{40}	$\sim1\times10^{-5}$	2
NGC 4579 (M58)	$\sim4\times10^6 M_\odot$	1.4×10^{41}	$\sim3\times10^{-4}$	3
NGC 4594 (M104)	$\sim1\times10^9 M_\odot$	1.0×10^{41}	$\sim8\times10^{-7}$	4

1. Ho, Filippenko & Sargent 1995; 2. Miyoshi et al. 1995; 3. Barth et al. 1996; 4. Kormendy et al. 1996

6.4.6 Limits on accretion mechanisms

We usually assume the presence of the standard Shakura & Sunyaev disk (1973) in AGNs. An advection dominated accretion flow (ADAF) model is extensively studied (e.g. Kato et al. 1996). Lasota et al. (1996) applies an ADAF to the LLAGN NGC 4258 which emits at extremely low Eddington ratio. In an ADAF, accreting matter is optically thin and geometrically thick, and heated up to very high temperature ($T_i \sim 10^{12}$K, $T_e \sim 10^9$K). Then UV bump and iron K emission expected from an optically thick and geometrically thin disk are not present.

The absence of the UV bump in LLAGNs is consistent with an ADAF. No significant iron K emission in most of the objects is also consistent with an ADAF. However iron emission lines are detected from NGC 3031, NGC 4579, and NGC 5033 among type 1 LLAGNs. Their observed equivalent widths indicate that matter in cold – He-like ionization state subtends large solid angle viewed from the X-ray nucleus. This is inconsistent with an ADAF.

On the other hand, the iron emission line at 6.7 keV detected from NGC 4579 cannot be explained by the expected ionization state from the X-ray irradiated standard disk calculated by Matt et al. (1993) (see subsection NGC 4579).

These results suggest that the accretion process in LLAGNs would be different from higher luminosity AGNs. Thus simple ADAF model or standard accretion disk model alone cannot explain all of the observed properties.

Chapter 7

Conclusion

We observed low luminosity Seyfert galaxies and LINERs with the *ASCA* satellite and detected X-rays from all of the object but for one object. Almost all sources are detected for the first time in the 2–10 keV band.

We obtained hard X-ray sample of LINERs of unprecedented number and quality. Almost all LINERs with broad Hα in the optical spectrum indicate point like hard X-ray source. Their X-ray luminosity is well correlated with Hα luminosity. This fact strongly support the the origin of these LINERs are photoionization by a low luminosity AGN. On the other hand, majority of LINERs without broad Hα in our sample are X-ray dim compared to L_X–$L_{H\alpha}$ correlation for low luminosity Seyfert galaxies and LINERs with broad Hα. X-ray weakness of these objects means that their optical emission lines are ionized by other mechanism rather than low luminosity AGNs and/or that AGN is heavily obscured even at energies above 2 keV. X-rays from these objects are consistent with due to starburst activity and/or discrete sources in the host galaxy.

Using low luminosity AGN (LLAGN) sample consists of low luminosity Seyfert galaxies and LINERs whose X-ray emission is considered to be dominated by low luminosity AGNs, we compared their X-ray properties with luminous AGNs. There are two classes of LLAGNs, i.e. type 1 and type 2 which indicates small and large intrinsic absorption in their X-ray spectra, respectively; as Seyfert 1 and 2. Their continuum shape are very similar to luminous Seyfert galaxies. Iron emission in type 2 LLAGNs are fully consistent with luminous Seyfert 2 galaxies. On the other hand, iron emission lines from type 1 LLAGNs show variety in the strength and center energy on the contrary to usual Seyfert 1s. These results are inconsistent with both prediction of iron emission from the X-ray irradiated disk (Matt et al. 1993) and advection dominated accretion flow model by Lasota et al. (1995), and infer that physical states of the accretion disk around the LLAGNs are

different from those of Seyfert 1s.

We also detected thermal emission of $kT = 0.5 - 1$ keV from most of the galaxies. The origins of thermal component are inter stellar medium / galactic super winds heated by on going starburst activity and extended X-ray halo similar to elliptical galaxies.

Acknowledgments

I am gratefull to Profs. K. Yamashita, H. Kunieda, and Y. Tawara for their continuous support and guidance throughout my doctral course. I would like to thank Dr. Luis C. Ho for fruitful collaboration and providing us information of their new results from optical surveys and *HST* observations in prior to publications. Thanks are due to Profs. Kazuo Makishima, Richard F. Mushotzky and Dr. Andrew F. Ptak for useful comments and discussions. I wish to thank all members in the X-ray laboratory, paticulaly to Dr. A. Furuzawa for technical help. I am grateful to the ASCA_ANL / SimASCA software development teams for their efferts. I would like to express my thank all the member of the *ASCA* team.

This research was made under the support of the JSPS.

references

Almaini, O., Shanks, T., Boyle, B.J., Griffiths, R.E., Roche, N., Stewart, G.C., & Georgantopoulos, I. 1996, MNRAS, 282, 295

Almaini, O. et al. 1998, Astron. Nachr. 319

Anders, E. & Grevesse, N. 1989, Geochimica et Cosmochimica, Acta 53, 197

Antonucci, R.R.J. 1993, ARA&A, 31, 473

Armus, M., Heckman, T.M., Weaver, K.A., Lehnert, M.D. 1995, ApJ, 445, 666

Awaki, H., Koyama, K., Kunieda, H., & Tawara, Y. 1990, Nature, 346, 544

Awaki, H., Koyama, K., Kunieda, H., Takano, S., Tawara, Y., & Ohashi, T. 1991a, ApJ, 366, 88

Awaki, H., Koyama, K., Inoue, H. & Halpern, J.P. 1991b, PASJ, 43, 195

Awaki, H. et al. 1994, PASJ, 46, L65

Awaki, H., Ueno, S., Koyama, K., Tsuru, T., & Iwasawa, K. 1996, PASJ, 48, 409

Bajaja, E., Dettmar, R.-J., Hummel, E., & Wielebinski, R. 1988, A&A, 202, 35

Baldwin, J.A., Philips, M.M. & Terlevich, R. 1981, PASP, 93, 5

Band, D.L., Klein, R.I., Cator, J.I., & Nash, J.K. 1990, ApJ, 362, 90

Barth, A., Reichert, G.A., Filippenko, A.V., Ho, L.C., Shields, J.C.,, Mushotzky, R.F., & Puchnarewicz, E.M. 1996a, AJ, 112, 1829

Barth, A. et al. 1996b in The Physics of LINERs in View of Recent Observations, eds. Eracleous, M. et al., San Francisco: ASP

Barth, A.J., Ho, L.C., Filippenko, A.V., & Sargent, W.L.W. et al. 1998 ApJ, in press

Bechtold et al. 1994, AJ, 108, 759

Böringer, H., Briel, U.G., Schwarz, R.A., Voges, W., Hartner, G., & Trümper, T. 1994, Nature, 368, 828

Boyle, B.J., McMahon, R.G., Wilkes, B.J., & Elvis, M. 1995, MNRAS, 276, 315

Braatz, J.A., Wilson, A.S. & Henkel, C. 1994, ApJ, 437, L99

Braatz, J.A., Wilson, A.S., & Henkel, C. 1996, ApJS, 106, 51

Bregman, J.N., Hogg, D.E., & Roberts, M.S. 1995, ApJ, 441, 561

Colina, L., Vargas, M.L.G., Delgado, R.M.G., Mas-Hesse, J.M., Pŕez, E., Alberdi, A., & Krabbe, A. 1997, ApJ, 488, L71

Collura, A., Reale, F., Schulman, E., and Bregman, J.N. 1994, ApJ, 420, L63

Comastri, A., Setti, G., Zamorani, G., Elvis, M., Wilkes, B.J., McDowell, J.C., & Giommi, P. 1992, 384, 62

Comastri, A., Setti, G., Zmorani, G., & Hasinger, G. 1995, A&A, 296, 1

Crane, P. et al. 1993, AJ, 106, 1371

Cui, W., Feldkhun, D., & Braun, R. 1997, ApJ, 477, 693

Dahari, O. & De Robertis, M.M. 1988, ApJ, 331, 727

David, L.P., Jones, C. & Forman, W. 1992, ApJ, 388, 82

Davis, D.S. & White III, R.E. 1996, ApJ, 470, L35

Done, C., Madejski, G.M., & Smith, D.A. 1996, ApJ, 463, L63

Dopita, M.A. et al. 1996, in The Physics of LINERs in View of Recent Observations, eds. Eracleous, M. et al., San Francisco: ASP

Dopita, M.A, Koratkar, A.P., Allen, M.G., Tsvetanov, Z.I., Ford, H.C., Bicknell, G.V., & Sutherland, R.S. 1997, ApJ, 490, 202

Dotani, T. et al. 1995, ASCA News Letter, 3

Dotani, T. et al. 1997, ASCA News Letter, 5, 14

Ehle, M., Pietsch, W., & Beck, R. 1995, A&A, 295, 289

Elvis, M. et al. 1995, ApJS, 95, 1

Fabbiano, G. 1988, ApJ, 330, 672

Fabbiano, G. 1989, ARA&A, 27, 87

Fabbiano, G., Heckman, T.M., & Keel, W.C. 1990, ApJ, 355, 442

Fabbiano, G., Gioia, I.M., & Trinchieri, G. 1989, ApJ, 347, 127

Fabbiano, G., Kim, D.-W., Trinchieri, G. 1992, ApJS, 80, 531

Fabbiano, G., Fassnacht, C., & Trinchieri, G. 1994, ApJ, 434, 67

Fabbiano, G. 1996, in The Physics of LINERs in View of Recent Observations, eds. Eracleous, M. et al., San Francisco: ASP

Fabbiano, G. & Juda, J.Z. 1997, ApJ, 476, 666

Fabian, A.C. 1986

Fabian, A.C., Rees, M.J., Stella, L., White, N.E. 1989, MNRAS, 238, 729

Fabian, A.C. et al. 1995, MNRAS, 277, L11

Ferland, G.J. & Netzer, H. 1983, ApJ, 264, 105

Filippenko, A.V. 1989, in Active Galactic Nuclei (IAU Symp. 134), p495

Filippenko, A.V. & Terlevich, R. 1992, ApJ, 397, L79

Filippenko, A.V. & Sargent, W.L.W. 1985, ApJS, 57, 503

Filippenko, A.V. 1996, in The Physics of LINERs in View of Recent Observations, eds. Eracleous, M. et al., San Francisco: ASP

Forman, W. Jones, C., & Tucker, W. 1985, ApJ, 293, 102

Fosbury, R.A.E., Mebold, U., Goss, W.M., & Dopita, M.A. 1978, MNRAS, 183, 549

Fukazawa, Y. et al. 1994, PASJ, 46, L141

Gendreau, K.C. 1994, ASCA News letter, 1

George, I.M., & Fabian, A.C. 1991, MNRAS, 249, 352

Guibert, P.W. & Rees, M.J. 1988, MNRAS, 233, 475

Halpern, J.P, & Steiner, J.E. 1983, ApJ, 269, L37

Heckman, T.M. 1980, A&A, 87, 152

Heckman, T.M., Blitz, L., Wilson, A.S., Armus, L., & Milley, G.K. 1989

Heckman, T.M., Baum, S.A., Van Breugel, W.J.M., & McCarthy, P. 1989

Heckman, T.M., Armus, L., & Miley, G. 1990, ApJS, 74, 833

Heckman, T.M., Lehnert, M.D., & Armus, L. 1993, in The Environment and Evolutin of Galaxies, p455, Kluwer Academic Publishers

Heckman, T.M. et al. 1997, ApJ, 482, 114

Hirano, T., Hayakawa, S., Nagase, F., Masai, K., & Mitsuda, K. 1987, PASJ, 39, 619

Ho, L.C., Filippenko, A.V., & Sargent, W.L.W. 1993, ApJ, 417, 63

Ho, L.C., Filippenko, A.V., & Sargent, W.L.W. 1995, ApJS, 98, 477

Ho, L.C. 1996, in The Physics of LINERs in View of Recent Observations, eds. Eracleous, M. et al., San Francisco: ASP

Ho, L.C., Filippenko, A.V., & Sargent, W.L.W. 1996, ApJ, 462, 183

Ho, L.C., Filippenko, A.V., & Sargent, W.L.W. 1997a, ApJS, 112, 315

Ho, L.C., Filippenko, A.V., Sargent, W.L.W., & Peng, C.Y. 1997b, ApJS, 112, 391

Ho, L.C., Filippenko, A.V., & Sargent, W.L.W. 1997c, ApJ, 487, 568

Huchra, J.P., Wyatt, W.F., & Davis, M. 1982, AJ, 87, 1628

Hummel, E., van der Hulst, J.M., & Dickey, J.M. 1984, A&A, 134, 207

Hummel, E., Van Der Hulst, J.M., Keel, W.C., & Kennicutt, R.C., Jr. 1987, A&AS, 70, 517

Idesawa, E. et al. 1997, ASCA News Letter

Ishisaki, Y. et al. 1997, PASJ, 48, 237

Iyomoto, N., Makishima, K., Fukazawa, Y., Tashiro, M., Ishisaki, Y. Nakai, N., & Taniguchi, Y. 1996, PASJ, 48, 231

Iyomoto, N., Makishima, K., Fukazawa, Y., Tashiro, M., & Ishisaki, Y. 1997, PASJ, 49, 425

Iwasawa, K. et al. 1993, ApJ, 409, 155

Iwasawa, K., & Taniguchi, Y. 1993, ApJ, 413, L15

Iwasawa, K., Yaqoob, T., Awaki, H., & Ogasaka, Y. 1994, PASJ, 46, L167

Iwasawa, K. 1994, Ph.D. thesis, Nagoya University

Iwasawa, K., Fabian, A.C., Mushotzky, R.F., Brandt, W.N., Awaki, H., & Kunieda, H. 1996, MNRAS, 279, 873

Iwasawa, K., Fabian, A.C., & Matt, G. 1997, MNRAS, 289, 443

Iwasawa, K., Fabian, A.C., Brandt, W.N., Crawford, C.S., & Almaini, O. 1997, MNRAS, 291, L17

Iwasawa, K., Fabian, A.C., & Nandra, K. 1998, submitted to MNRAS

Kallman, T.R, & MacCray, R. 1982, ApJS, 50, 263

Kato, S., Inagaki, S., Mineshige, S., & Fukue, J. 1996, Physics of Accretion Disks advection, radiation and magnetic fields, Gordon and Breach Science Publishers

Keel, W.C. 1983a, ApJ, 269, 466

Keel, W.C. 1983b, ApJS, 52, 229

Keel, W.C. et al. 1985, AJ, 90, 708

Kii, T., et al. 1991, ApJ, 367, 455

Kim, D.-W., Fabbiano, G., & Trinchieri, G. 1992, ApJ, 393, 134

Kohno, K. Kawabe, R., Tosaki, T., & Okumura, S.K. 1996, ApJ, 461, L29

Koratkar, A., Deustua, S.E., Heckman, T., Filippenko, A.V., Ho, L.C., & Rao, M. 1995, ApJ, 440, 132

Kormendy, J., & Richstone, D. 1995, ARA&A, 33, 581

Kormendy, J. et al. 1996, ApJ, 473, L91

Koski, A.T. & Osterbrock, D.E. 1976, ApJ, 203, L49

Koyama, K., Inoue, H., Tanaka, Y., Awaki, H., Takano, S., Ohashi, T., Matsuoka, M. 1989, PASJ, 41, 731

Lampton, M., Margon, B., & Bowyer, S. 1976, ApJ, 208, 177

Lasota, J.-P., Abramowicz, M.A., Chen, X., Krolik, J., Narayan, R., & Yi, I. 1996, ApJ, 462, 142

Lawrence, A. 1987, PASP, 99, 309

Lawson, A.J., Turner, M.J.L., Williams, O.R., Stewart, G.C., & Saxton, R.D. 1992, MNRAS, 259, 743

Lawson, A.J. & Turner, M.J.L. 1997, MNRAS, 288, 920

Leahy, D.A. & Creighton, J. 1993, MNRAS, 263, 314

Lightman, A.P. & White, T.R. 1988, ApJ, 335, 57

Makishima, K. 1986, in The Physics of Accretion onto Compact objects; eds Mason, K.O. et al.

Makishima, K. et al. 1989, PASJ, 41, 697

Makishima, K., Ohashi, T., Kondo, H., Palumbo, G.G.C., & Trinchieri, G. 1990 ApJ, 365, 159

Makishima, K. et al. 1994, PASJ, 46, L77

Makishima, K. 1994, in proc. of New Horizon of X-ray Astronomy, eds. Makino, F., & Ohashi, T.

Makishima, K. et al. 1996, PASJ, 48, 171

Malaguti, G. et al. 1997, A&A, 331, 519

Maoz, D., Filippenko, A.V., Ho, L.C., Rix, H.-W., Bahcall, J.N., Schneider, D.P., & Macchetto, F.D. 1995, ApJ, 440, 91

Maoz, D. Filippenko, A.V., Ho, L.C., Macchetto, F.D., Rix, H-W., & Schneider, D.P 1996, ApJS, 107, 215

Maoz, D. 1996 in The Physics of LINERs in View of Recent Observations, eds. Eracleous, M. et al., San Francisco: ASP

Maoz, D., Koratkar, A., Shields, J.C., Ho, L.C., & Filippenko, A.V. 1998, submitted to AJ

Maran, S.P., & Kinney, A.L. 1993, PASP, 105, 447

Marston, A.P., Elmegreen, D., Elmegreen, B., Forman, W., Jones, C., & Flanagan, K. 1995, ApJ, 438, 663

Matsushita, K. et al. 1994, ApJ, 436, L41

Matsushita, K., Makishima, K., Rokutanda, E., Yamasaki, N.Y., & Ohashi, T. 1997, ApJ, 488, L125

Matt, G., Perola, G.C., & Piro, L. 1991, A&A, 247, 27

Matt, G., Fabian, A.C., & Ross, R.R. 1993, MNRAS, 262, 179

Matt, G. et al. 1996, MNRAS, 281, L69

Miller, J.S. & Goodrich, R.W. 1990, ApJ, 355, 456

Moran, E.C., & Lehnert, M.D. 1997, ApJ, 478, 172

Morrison, R. & MacCammon, D. 1983, ApJ, 270, 199

Mulchaey, J.S. et al. 1994, ApJ, 436, 586

Murphy, E.M., Lockman, F.J., Laor, A., & Elvis, M. 1996, ApJS, 105, 369

Mushotzky, R.F., Marshall, F.E., Boldt, E.A., Holt, S.S., & Serlemitsos, P.J. 1980, ApJ, 235, 377

Mushotzky, R.F. 1982, ApJ, 256, 92

Mushotzky, R.F. 1984

Mushotzky, R.F. and Wandel, A. 1989, ApJ, 339, 674

Mushotzky, R.F. 1992, The Nearest Active Galaxies, eds. Netzer, H. and Beckman, J., (Madrid:CSIC)

Mushotzky, R.F., Done, C. & Pounds, K.A. 1993, ARA&A, 31, 717

Mushotzky, R.F., Loewenstein, M., Awaki, H., Makishima, K., Matsushita, K., & Matsumoto, H. 1994, ApJ, 436, L79

Mushotzky, R.F., Fabian, A.C., Iwasawa, K., Kunieda, H., Matsuoka, M., Nandra, K., & Tanaka, Y. 1995, MNRAS, 272, L9

Nandra, K. & Pounds, K.A. 1994, MNRAS, 268, 405

Nandra, K., George, I., Turner, T.J., & Fukazawa, Y. 1996, ApJ, 464, 165

Nandra, K., George, I.M., Mushotzky, R.F., Turner, T.J., & Yaqoob, T 1997, ApJ, 476, 70

Nandra, K., George, I.M., Mushotzky, R.F., Turner, T.J., & Yaqoob, T 1997, ApJ, 477, 602

Nandra, K., George, I.M., Mushotzky, R.F., Turner, T.J., & Yaqoob, T 1997c, ApJ, 488, L91

Nicholson, K.L., Reichert, G.A., Mason, K.O., Puchnarewicz, E.M., Ho, L.C., Shields, J.C., & Filippenko, A.V. 1997, MNRAS, submitted

Ohashi, T., Makishima, K., Tsuru, T., Takano, S., Koyama, K., & Stewart, G.C. 1990, ApJ, 365, 180

Ohashi, T. et al. 1996, PASJ, 48, 157

Okada, K., Dotani, T., & Mitsuda, K. 1997, PASJ, in press

Osterbrock, D.E. 1989, Astrophysics of Gaseous Nebulae and Active Galactic Nuclei, California: University Science Books

Otani, C. & Dotani, T 1994, ASCA News letter, 1

Ohyama, Y. & Taniguchi, Y. 1996, in The Physics of LINERs in View of Recent Observations, eds. Eracleous, M. et al., San Francisco: ASP

Palumbo, G.G.C., Fabbiano, G., Fransson, C & Trinchieri, G. 1985, ApJ, 298, 259

Pérez-olea, D.E. & Colina, L. 1996, ApJ, 468, 191

Petre, R., Mushotzky, R.F., Serlemitsos, P.J., Jahoda, K., & Marshall, F.E. 1993, ApJ, 418, 644

Phillips et al. 1986

Pounds, K.A., Nandra, K., Stewart, G.C., George, I.M., Fabian, A.C. 1990, Nature, 344, 132

Ptak, A., Yaqoob, T., Serlemitsos, P., Kunieda, H., & Terashima, Y. 1996, ApJ, 459, 542

Ptak, A., Serlemitsos, P., Yaqoob, T., Mushotzky, F., & Tsuru, T. 1997, AJ, 113, 1286

Ptak, A. 1997, Ph.D. thesis, University of Maryland

Reynolds, C.S., Fabian, A.C., Makishima, K., Fukazawa, Y., & Tamura, T. 1994, MNRAS, 268, L55

Raymond, J.C., & Smith, B.W. 1977, ApJS, 35, 419

Read, A.M., Ponman, T.J., & Strickland, D.K. 1997, MNRAS, 286, 626

Rees 1984, ARA&A, 22, 47

Rees 1990, Science

Rothschild, R.E. et al. 1993

Reichert, G.A., Branduardi-Raymont, G., Filippenko, A.V., Mason, K.O., Puchnarewicz, E.M., & Wu, C.-C. 1992, ApJ, 387, 536

Salvati, M., Bassani, L., Della Ceca, R., Maiolino, R., Matt, G., & Zamorani, G. 1997, A&A, 323, L1

Sandage, A. & Tammann, G.A. 1975, ApJ, 196, 313

Serlemitsos, P.J. et al. 1995, PASJ, 47, 105

Serlemitsos, P.J., Ptak, A., & Yaqoob, T. 1996 in The Physics of LINERs in View of Recent Observations, eds. Eracleous, M. et al., San Francisco: ASP

Shakura, N.I. & Sunyaev, R.A. 1973, A&A, 24, 337

Shields, J.C. 1992, ApJ, 399, L27

Smith, D.A., & Done, C. 1996, MNRAS, 280, 255

Stark, A.A., Gammie, C.F., Wilson, R.W., Bally, J., Linke, R.A., Heiles, C., & Hurwitz, M. 1992, ApJS, 79, 77

Stauffer, J.R. 1982, ApJ, 262, 66

Tanaka, Y. et al. 1995, Nature, 375, 659

Tanaka, Y., Inoue, H., & Holt, S.S. 1994, PASJ, 46, L37

Taniguchi, Y. et al. 1996, ApJ, 467, 215

Terashima, Y., Serlemitsos, P.J., Kunieda, H., & Iwasawa, K. 1994, in proc. of New Horizon of X-ray Astronomy, eds. Makino, F. & Ohashi, T., Universal Academy Press

Terashima, Y., Ptak, A., Fujimoto, R., Itoh, M., Kunieda, H., Makishima, K., & Serlemitsos, P.J. 1998a, ApJ, in press

Terashima, Y., Kunieda, H., Misaki, K., Mushotzky, R.F., Ptak, A., & Reichert, G. 1998b, submitted to ApJ

Tomisaka, K. & Ikeuchi, S. 1988, ApJ, 330, 695

Tsuru, T. 1992, Ph.D. thesis, University of Tokyo

Tsuru, T. et al. 1998, PASJ, in press

Tsusaka, Y. et al. 1995, Appl. Opt., 34, 4848

Tuahunter, C. & Tsvetanov, Z. 1989, Nature, 341, 422

Turner, T.J. & Pounds, K.A. 1989, MNRAS, 240, 833

Turner, T.J., George, I.M., Nandra, K., & Mushotzky, R.F. 1997a, ApJS, 113, 23

Turner, T.J., George, I.M., Nandra, K., & Mushotzky, R.F. 1997b, ApJ, 488, 164

Tully, R.B. 1988, Nearby Galaxies Catalog, Cambridge University Press

Ueda, Y. et al. 1996, ASCA News letter, 4, 28

Ueno, S., Mushotzky, R.F., Koyama, K., Iwasawa, K., Awaki, H., & Hayashi, I. 1994, PASJ, 46, L71

Ueno, S. 1995, Ph.D. thesis, Kyoto University

Veilleux, S & Osterbrock, D.E. 1987, ApJS, 63, 295

Véron-Cetty, M.-P. & Véron, P. 1986, A&AS, 66, 335

Vogler, A., Pietsch, W., & Kahabka, P. 1996, A&A, 305, 74

Ward, M.J., Done, C., Fabian, A.C., Tennant, A.F., & Shafer, R.A. 1988, ApJ, 324, 767

Warner, J.W. 1977, ApJ, 213, L29

Warwick, R.S., Sembay, S., Yaqoob, T., Makishima, K., Ohashi, T., Tashiro, M., & Kohmura, Y. 1993, MNRAS, 265, 412

Watson, M.G., Stanger, V., & Griffiths, R.E. 1984, ApJ, 286, 144

Weedman, D.W. 1977, ARA&A, 15, 69

Williams et al. 1992

Yamashita, A. 1995, Master thesis, University of Tokyo (in Japanese)

Yamashita, A. et al. 1997, IEEE Transactions on Nuclear Science, 44

Yamashita, A. et al. 1997, ApJ, 486, 763

Życki, P.T. & Czerny, B. 1994, MNRAS, 266, 653

副論文